



University College London

**Department of Chemistry
Faculty of Mathematical and Physical Sciences (MAPS)**

Bioinspired ordered polymer-composites

Yi Shi

Submitted in fulfilment of the requirement for the degree of

Doctor of Philosophy

March 2017

I, Yi Shi, confirm that the work presented in this thesis is my own. Where information has been derived from other sources, I confirm that this has been indicated in the thesis.

Signed _____

Date _____

Abstract

As the number of cars has expanded to 1 billion, technologies to slow the consumption of oil are sought. A 10 wt. % reduction of a car body mass can lead to a 7 % decrease in fuel consumption. Thus, there is a quest for high strength to weight ratio, high elastic modulus, toughness and low cost materials for the vehicle industry. Biological composites such as nacre, have outstanding mechanical properties because of its microstructure and aim of this project is to mimic the hierarchical structure of nacre.

In this project, clays including montmorillonite, laponite, Black Hills bentonite as well as kaolinite were used to fabricate the layered structure of nacre. A solution casting method was used to build the hierarchical nacre-like composite and in-situ photo polymerisation, vacuum impregnation and vacuum assisted filtration methods were employed for preformed clay sheets and polymers (methyl methacrylate, tri(ethyleneglycol) dimethacrylate, poly(propylene glycol) dimethacrylate as well as epoxy resin) to mimic the structure of nacre.

XRD was used to indicate the intercalation of polymer and orientation function of clay sheets and SEM for microstructure detection. Tensile testing was used to investigate the properties of different volume fraction (40-70 vol. %) composites and the highest value 98 MPa came from 50 vol. % MMT/PVA composite. The mechanism of polymerisation of acrylic groups with clays present was analysed and redox polymerisation was introduced for the kaolinite/PMMA system. Kaolinite/PMMA samples were tested via three points loading and a composite with flexural strength of (40 ± 20) MPa and flexural modulus of (30 ± 20) GPa was obtained.

Acknowledgement

I would like to thank my supervisor Prof. Julian R.G. Evans for his guidance, support and suggestions during my four years' study. I appreciate his background knowledge in the experimental design; patience and critical thinking in the results discussions. I have learned a lot from him.

I also wish to thank my colleagues in Julian's group, Miss Yuan Qi, Mr. Matteo Conti, Mr. Hao Su, and Miss Katherine Sanders, for their assistance, cooperation and discussions. I would like to express my thanks to Dr. Jeremy Cockcroft and Mr. Martin Vickers, for their training and support to use the XRD equipment. Also, my appreciation goes to Dr. Steve Firth for his time and guidance on the use of TGA, SEM, and EDS.

I would like to thank my friends, both in China and UK, for their support and understanding. A special gratitude to Dr. Liying Wang and Dr. Shuqun Chen for their advice and help.

I want to acknowledge the financial support of the M3S Industrial Doctorate Centre at UCL, which allowed me the opportunity to accomplish my study in UK.

I wish to thank my parents and all my family members for their patience and encouragement whenever needed. Words are not enough to express all my gratitude to them. I owe everything to them.

Abbreviations

AFM	Atomic force microscopy
AIBN	2-2'-azobisisobutyronitrile
BH	Black hill bentonite
BPO	Benzoyl peroxide
CCNs	Calcium carbonate nanotablets
CFRC	Carbon fibre reinforced composites
CTAB	Hexadecyl-trimethylammonium bromide
CTL	Coal to liquid
DMPT	N,N-dimethyl-p-toluidine
DSC	Differential scanning calorimetry
EDL	Electrical double layer
EDS	Energy dispersive X-ray spectroscopy
EG	Ethylene glycol
EPD	Electrophoretic deposition
FTIR	Fourier transform infrared spectroscopy
GO	Graphene oxide
HASC	Hot-press assisted slip casting
HMPP	Sodium hexametaphosphate
ITO	Indium–tin–oxide
LBL	Layer-by-layer assembly

MEHQ	4-methoxyphenol
MMA	Methyl methacrylate
MMT	Montmorillonite
PCN	Polymer-clay nanocomposites
PDDA	Poly (diallyldimethylammonium chloride)
PDM	Poly (dodecylmethacrylate)
PEI	Poly (ethylenimine)
PMMA	Poly (methyl methacrylate)
PPD	P-phenylenediamine
PPGDMA	Poly (propylene glycol) dimethacrylate
PTFE	Polytetrafluoroethylene
PTPGDA	Poly (tripropylene glycol diacrylate)
PVA	Poly (vinyl alcohol)
SEM	Scanning electron microscopy
SPA	Sodium polyacrylate
TEGDMA	Tri (ethyleneglycol) dimethacrylate
TGA	Thermogravimetric analysis
Tween-20	Polyoxyethylene sorbitan monolaurate
XRD	X-ray diffraction

Table of Content

List of Figures	12
List of Tables.....	18
1 Introduction	20
1.1 General introduction.....	21
1.2 Motivation for this research.....	25
References	28
2 Literature Review	30
2.1 Composite materials	31
2.2 Structure of polymer-clay nanocomposites	32
2.3 Principles of biomimetics	32
2.3.1 The properties of nacre	33
2.3.2 Attempts to replicate the nacre structure	40
2.3.3 Factors influencing self-assembled montmorillonite during drying.....	48
2.3.4 Introduction of electric double layers and zeta potential	50
2.3.5 Clay and electric double layers	51
2.4 Structure of clays and graphene oxide	54
2.4.1 Structure of montmorillonite	54
2.4.2 Structure of laponite.....	55
2.4.3 Structure of kaolinite	55
2.4.4 Structure of graphene oxide.....	56
References	58
3 Experimental Details.....	64
3.1 Details of materials and their sources.....	65
3.2 Solution-casting process of clay and GO/PVA composite.....	65
3.2.1 Self-assembled process of clay discs	65

3.2.2 Original process of solution casting from Walley [2]	66
3.2.3 Modified process of solution casting of MMT/PVA nanocomposite.....	67
3.3 MMT/epoxy resin composite	68
3.3.1 Mixture of clays and epoxy resins	68
3.3.2 Self-assembled clay discs	69
3.3.3 Ion-exchanged MMT	69
3.3.4 Vacuum impregnation.....	69
3.4 Polymerisation of methyl methacrylate (MMA) and MMA/clay composites..	71
3.5 Photo polymerisation of laponite/polymer composite.....	72
3.5.1 Infiltration of monomer in self-assembled structure.....	73
3.5.2 Polymerisation of clay discs	73
3.6 Study of kaolinite and kaolinite composite	75
3.6.1 Kaolinite sedimentation process	75
3.6.2 Kaolinite epoxy resin system	76
3.6.3 Kaolinite/MMA composite	76
3.6.3.1 Redox polymerisation of MMA	77
3.6.3.2 Redox polymerisation of kaolinite and MMA	77
3.7 Characterisation of instruments and their operation.....	77
3.7.1 Fourier transform infrared spectroscopy (FTIR)	77
3.7.2 X-Ray diffraction (XRD).....	78
3.7.3 Measurement of mechanical properties	78
3.7.4 Differential scanning calorimetry (DSC).....	79
3.7.5 Scanning electron microscopy (SEM)	79
3.7.6 Energy dispersive X-ray spectroscopy (EDS)	79
3.7.7 Thermogravimetric analysis (TGA).....	80
3.7.8 Atomic force microscopy (AFM)	80
3.7.9 UV-VIS spectrometer	80

3.7.10 Laser cutter	80
3.7.11 Ultrasonic probe.....	80
References	82
4 Development of Clay/Polymer Composites.....	83
4.1 Montmorillonite and polyvinyl alcohol nanocomposites by solution casting..	84
4.1.1 X-ray diffraction of MMT and its composite	84
4.1.2 SEM figures of MMT and PVA composites	85
4.1.3 EDS of 50 vol. % MMT/PVA nanocomposite	88
4.1.4 Mechanical testing	88
4.2 Factors affecting mechanical properties of MMT/PVA composite	90
4.3 Characterisation of modified composites	93
4.3.1 Study of MMT size after centrifugation	93
4.3.2 EDS analysis of elemental composition before and after centrifugation...	96
4.3.3 Orientation function of Nanofil 116 MMT	98
4.3.4 Thermal analysis of MMT/PVA composites	101
4.3.5 Mechanical properties of MMT/PVA composites.....	104
4.4 Clays and epoxy resin system	109
4.4.1 XRD of clays and clays resin mixture	109
4.4.2 SEM of self-assembled structure	112
4.4.3 Theoretical study of epoxy resin.....	114
4.4.4 Analysis of MMT/resin composite	116
4.5 MMA polymerisation mechanism.....	121
References	128
5 Laponite Based Clay/Polymer Nanocomposites	132
5.1 Analysis of laponite/PVA nanocomposite from solution casting.....	133
5.1.1 X-ray diffraction of laponite and its composite	133
5.1.2 Fracture surface of laponite/PVA composites.	134

5.1.3 UV-visible transmittance of laponite/PVA nanocomposite.....	136
5.2 Study the photo polymerisation in the presence of clay.....	140
5.2.1 FTIR quantification of degree of conversion and rate of reaction.....	142
5.2.2 Fabrication of ordered structures by preformed laponite film.....	145
References	147
6 Kaolinite Based Polymer Composite	148
6.1 Kaolinite and resin system.....	149
6.1.1 Sedimentation experiment to adjust the optimal pH for kaolinite suspensions	149
6.1.2 SEM of kaolinite sheets obtained by the self-assembly processes	150
6.1.3 Kaolinite film fabrication by vacuum filtration.....	151
6.1.4 Packing efficiency of kaolinite filter cake	153
6.1.4 Orientation function of kaolinite filter cake	155
6.1.5 The possibility of infiltration of epoxy resin	155
6.1.6 Evidence of resin infiltration.	156
6.1.7 Mechanical testing of kaolinite/resin composite.	158
6.2 Kaolinite/PMMA polymer composites by thermal polymerisation	160
6.2.1 Redox polymerisation of MMA.....	162
6.2.2 Mechanical testing of samples prepared by redox polymerisation in the presence of kaolinite	163
6.2.3 Mechanical testing of kaolinite/PMMA composite	164
References	165
7 Conclusions and Future work	167
7.1 Conclusions	168
7.2 Future works.....	173
References	173
Appendix	186
Appendix 1. Graphene oxide and PVA composites	175

A1.1 Characterisation of GO	175
A1.2 Characterisation of GO/PVA nanocomposite.....	176
A1.3 SEM figures of GO and PVA composites made by self-drying process .	177
Appendix 2. The absorbance to thickness of MMT/PVA composite.....	179
Appendix 3. Orientation function of kaolinite	180
Appendix 4. Flexural strength and modulus of kaolinite/resin composite.....	181
Appendix 5. FTIR Spectra.....	182
Appendix 6. Figures and results of three point loading test of PMMA and PMMA/kaolinite composite by redox polymerisation	184
References	186

List of Figures

Figure 1-1. CFRC frame used in VW concept vehicle. .	22
Figure 1-2. Ashby map of strength-stiffness of materials, focusing on metals and alloys.	22
Figure 1-3. Ashby map of strength-cost of CFRC.	23
Figure 1-4. Low carbon vehicle with polypropylene/aluminium shell.	24
Figure 1-5. Air quality in China 2013.	25
Figure 1-6. Histogram of oil demands in China. A: extrapolation of oil demands between 2000 to 2020. B: extrapolation under a strategy for reducing oil consumption. C: extrapolation under a further reducing oil consumption strategy.	26
Figure 1-7. The Coal-to-Liquid process (Synfuels China, 2004–2005).	27
Figure 2-1. Different structures of PCN.	32
Figure 2-2. Photograph of the inner, iridescent region of the nacre.	33
Figure 2-3. SEM image of fracture surface of nacre.	34
Figure 2-4. High magnitude view on the platelets of nacre. Corrugated surface as white arrow point out.	34
Figure 2-5. (a) Fracture surface of nacre showing the brick-mortar structure separated by mesolayer. (b) Nanolayer of nacre and organic membrane. (c) Mesolayer and nanolayer within a partially demineralised nacreous structure.	35
Figure 2-6. Summary of nacre inspiration in advanced materials applications.	36
Figure 2-7. Schematics of sheet nacre and columnar nacre and their SEM picture.	37
Figure 2-8. Nanograins on the aragonite tablets.	37
Figure 2-9. (A) Schematic of two platelets with nanoasperities during sliding (B) The stress–strain curve of nacre shows the hardening mechanism	38
Figure 2-10. SEM images of fracture surface of shell. A distinct structure is observed in each platelets as black arrows indicated. High magnitude view on the platelets showing their connection (white arrows).	38
Figure 2-11. Transmission electron microscopy (TEM) image of nacre shows the organic phases are connected with each tablet.	39
Figure 2-12. Mineral bridges in nacre.	39
Figure 2-13. Sketch of the structure of nacre and a single platelet of nacre.	40

Figure 2-14. Three mechanism models during sliding between platelets. (A) Nanoasperities hardening (B) Organic stiffening (C) Fractured mineral bridges toughening.....	40
Figure 2-15. A cross section of the composite film prepared by evaporation.....	42
Figure 2-16. (a) The Al ₂ O ₃ -PMMA lamellar structure prepared by ice-templated (white: ceramic; black: polymer). (b) The nacre-like structure produced by pressing and sintering the lamellar scaffolds.....	43
Figure 2-17. The cross section of the Al ₂ O ₃ /epoxy resin nacre-like composite obtained by HASC.	45
Figure 2-18. (a) Processes of the artificial chitosan/MMT films. (b) Cross section of the chitosan/MMT film. (c) Stress–strain curves of chitosan/MMT film. (d) Stress–strain curves of PVA/MMT film. (e) Samples prepared by evaporation and SEM image of cross-section of the composite.	46
Figure 2-19. Electric double layer surrounding nanoparticle.....	50
Figure 2-20. Structure of MMT.....	54
Figure 2-21. Details of particle view of MMT.....	54
Figure 2-22. Structural diagram of kaolinite showing two 1:1 layers joined together by hydrogen bonding.	56
Figure 2-23. Schematic showing structure of graphene.....	56
Figure 2-24. The structure of graphene oxide.....	57
Figure 3-1. Illustration of self-assembly process.....	67
Figure 3-2. the MMT suspension after centrifugation. Left: sediment shows unexfoliated platelets and black solid impurities. Right: supernatant MMT suspension and PVA solution.	67
Figure 3-3. Schematic of vacuum impregnation system.....	70
Figure 3-4. (a) Schematic of the reactor used for polymerisations. (b) Plan of the reactor used for polymerisations. Inner diameter is 96.5 mm. Bolts are 4 mm (M4).	71
Figure 3-5. (a) A front view of photo polymerisation device. (b) A plan view of photo polymerisation device.	74
Figure 3-6. Different pH of kaolinite suspensions	75
Figure 4-1. XRD traces for composites and for MMT-as received after drying for 864 ks (240h) at ambient temperature. The samples are identified by vol. %.	84
Figure 4-2. Properties of Nanofil 116 from Rockwood, USA.	85

Figure 4-3. SEM image of fracture surface of MMT sheet slowly dried from suspension.	86
Figure 4-4. Scanning electron micrographs of cryogenic fracture surface of (a) & (b) 70 vol. % clay with 30 vol. % PVA composites; (c) & (d) 60 vol. % clay with 40 vol. % PVA composites; (e) & (f) 50 vol. % clay with 50 vol. % PVA; (g) & (h) 40 vol. % clay with 60 vol. % PVA.....	87
Figure 4-5. EDS spectrum of elements from MMT/PVA composite.	88
Figure 4-6. Particle (size around 20 μm) observed by SEM before centrifugation process.....	91
Figure 4-7. Effect of geometric discontinuities on stress distribution.	92
Figure 4-8. The effect of different cutting methods on the edge of composite samples: edge damage can affect the mechanical strength measurement. These are SEM images after preparation by (a) hot knife, (b) scissors, (c) laser cutter, (d) blade.	92
Figure 4-9. Examples of individual MMT platelets by AFM.	94
Figure 4-10. Examples for thickness analysis by AFM.	95
Figure 4-11. Sedimentation after centrifugation.	96
Figure 4-12. EDS shows the elemental composition of (a) Nanofil 116 MMT, (b) sedimentation after centrifugation.....	97
Figure 4-13. XRD data showing the intensity of the (002) peak for each tilt angle, - 10 ° to 80 ° in 5 ° step.	98
Figure 4-14. Graph showing experimental MMT orientation distribution function.	99
Figure 4-15. DSC of MMT/PVA composite. The samples are given as the volume percentage of clays.....	101
Figure 4-16. TGA of MMT/PVA composites. The samples are identified as volume fraction of MMT.....	102
Figure 4-17. An example of tensile strength test of 50 vol. % MMT/PVA composite.	106
Figure 4-18. XRD traces for Nano116 MMT and MMT/resin mixture.....	110
Figure 4-19. XRD traces for BH Natural and BH/resin mixture	110
Figure 4-20. XRD traces for laponite and laponite/resin mixture.....	111
Figure 4-21. XRD trances of MMT and PPD modified MMT.....	112
Figure 4-22. SEM of cross section of variation clays (a) Nano116 MMT, (b) BH Natural, (c) laponite, (d) PPD modified MMT.....	113

Figure 4-23. FTIR spectrums for MMT and PPD modified MMT.	114
Figure 4-24. FTIR spectra for two resins: RX672H and RX900D cured with different procedures. (a) RX900D cured after keeping at a low temperature for 72 hr, (b) RX900D cured directly at room temperature, (c) RX672H cured directly at the room temperature, (d) RX672H cured after keeping at a low temperature for 72 hr.	115
Figure 4-25. Image of MMT/resin composite sample.	116
Figure 4-26. FTIR spectra for the top surface of clay discs (A) PPD-MMT 672H-RT*, (B) PPD-MMT 672H-LT*, (C) PPD-MMT-900D-RT, (D) PPD-MMT-900D-LT, the bottom surface of clay discs (a) PPD-MMT-672H-RT, (b) PPD-MMT-672H-LT, (c) PPD-MMT-900D-RT, (d) PPD-MMT-900D-LT.	118
Figure 4-27. FTIR spectra for the top surface of MMT (a) MMT-672H-RT, (b) MMT-672H-LT, (c1) MMT-900D-RT, (c2) MMT-900D-LT, (c3) MMT-900D-LT120	119
Figure 4-28. SEM of MMT/resin composite (a) MMT-900D after cryogenic treatment, (b) PPD modified MMT-900D after cryogenic treatment.	120
Figure 4-29. The initiators decomposition to form free radicals (a) BPO, (b) AIBN.	122
Figure 4-30. Mechanism of inhibition by phenol.....	125
Figure 4-31. Mechanism for inhibition of free radical reaction by clay mineral.	127
Figure 5-1. XRD traces for PVA composites and for as-received laponite. The samples are identified by wt. % of laponite.	133
Figure 5-2. SEM of fracture surface of (a) 40wt. % laponite/PVA composites, (b) 50 wt. % laponite/PVA composites, (c) 60wt. % laponite/PVA composites, (d) 70 wt. % laponite/PVA composites.....	134
Figure 5-3. SEM of fracture surface of 60 wt. % laponite/PVA composite.	135
Figure 5-4. UV-visible transmittance of laponite/PVA nanocomposite. The samples were given as wt. %	136
Figure 5-5. Compared MMT and laponite clay film (a) transparent laponite, (b) dark yellow MMT.	137
Figure 5-6. The illustration of Beer-Lambert law.....	137
Figure 5-7. The relationship between transmittance and absorbance. T ranges from 1-100 %.	139
Figure 5-8. Graph showing absorbance to thickness of laponite composite within 400-800 nm. The samples were defined as wt. %.....	140

Figure 5-9. XRD traces of clay/polymer mixture (a) Nano116 MMT mixed with PPGDMA and TEGDMA (b) laponite mixed with PPGDMA and TEGDMA	141
Figure 5-10. FTIR spectra of clay-monomer absorbance focusing on the peak at 1318 cm^{-1} . (a) PPGDMA with Nano116 MMT at 14.4, 27.9, 121.8 and 349.6 s, (b) PPGDMA with laponite at 14.4, 27.6, 121.5 and 228.0 s, (c) TEGDMA with MMT at 14.3, 27.7, 121.5 and 590.3 s, (d) TEGDMA with laponite at 14.4, 27.8, 121.4 and 228.5 s.	144
Figure 6-1. Sedimentation graph of kaolinite suspension with different pH values plotted by sediment height versus time.	149
Figure 6-2. SEM of lower region of the kaolinite cross section at (left) pH=7.3 (right) pH=10.0.....	150
Figure 6-3. SEM of upper region of the kaolinite cross section at (left) pH=7.3 (right) pH=10.0.....	151
Figure 6-4. SEM images showing cross sections of kaolinite sheets filtered over 3 h (left) and 5 h (right).....	152
Figure 6-5. SEM images showing the bottom (left) and top (right) of a kaolinite film filtrated in 5 h.	153
Figure 6-6. Infiltration experiment of kaolinite filter cake for 1 hr and 12 hr, (a) bottom side (b) top side of kaolinite.	156
Figure 6-7. EDS mapping for vacuum impregnation sample.	157
Figure 6-8. SEM of kaolinite plates by resin vacuum impregnation.	158
Figure 6-9. Graph of three point loading test.	158
Figure 6-10. Mechanism of the redox reaction between DMPT and BPO	162
Figure 6-11. PMMA (left); PMMA/kaolinite composites (right) showing top (above) and bottom (below) side of kaolinite filter cake.	163
Figure A1-1. X-ray diffraction of prepared GO.....	175
Figure A1-2. XRD traces for GO/PVA composites after self-assembly process at ambient temperature. The samples are identified by wt. % of GO.	176
Figure A1-3. Scanning electron micrographs of fracture surface of (a) 40 wt. % GO/PVA composites (b) 50 wt. % GO/PVA composites (c) 60 wt. % GO/PVA composites (d) 70 wt. % GO/PVA composites.....	178
Figure A2-1. The absorbance to thickness of MMT/PVA composite. The sample was defined in volume percentage of MMT.	179

Figure A3-1. X-ray diffraction of the variation of the intensity of the kaolinite (002) peak reflection by changes in the tilt angle, ψ	180
Figure A3-2. Graph showing experimental kaolinite orientation distribution function	180
Figure A5-1. FTIR spectrum of Barrisurf LX kaolinite.....	182
Figure A5-2. FTIR spectrum of methyl methacrylate.....	182
Figure A5-3. FTIR spectrum of poly(methyl methacrylate) by redox polymerisation	183
Figure A5-4. FTIR spectrum of a PMMA/kaolinite composite sample polymerised under N ₂	183
Figure A6-1. Three points loading test of PMMA by redox polymerisation.....	184
Figure A6-2. Three points loading test of kaolinite/PMMA composite	184

List of Tables

Table 2-1. Summary of artificial nacre-like nanocomposites.	48
Table 2-2. The relationship between the stability and value of Zeta potential.....	51
Table 4-1. Results from XRD Figure 4-1.....	85
Table 4-2. Failure of MMT/PVA composites.	89
Table 4-3. Aspect ratio calculation from AFM Figure 4-9.....	94
Table 4-4. The degree of orientation of different tilts.	100
Table 4-5. Analysis of the TGA and DSC data.	103
Table 4-6. The raw and calculated date for tensile testing of MMT/PVA composites.	106
Table 4-7. Young's modulus of composites.	107
Table 4-8. Weibull modulus of the samples.	109
Table 4-9. Calculated data from XRD traces of clay and resin mixture.	111
Table 4-10. XRD results of two theta and changes in basal spacing.	117
Table 4-11. Thermal polymerisation of stabilised MMA with 1 wt. % and 4 wt. % BPO.....	123
Table 4-12. MMA with 4 wt. % BPO mixed with Al ₂ O ₃	125
Table 4-13. MMA with 4 wt. % BPO mixed with MMT.	125
Table 4-14. MMA with 4 wt. % BPO mixed with laponite.....	126
Table 5-1. Results from XRD traces for PVA-laponite composites from Figure 5-1.	133
Table 5-2. Calculated results from XRD traces from Figure 5-9.....	142
Table 5-3. FTIR assignment with comments corresponded to polymerisation.	143
Table 5-4. The degree of conversion of monomer and maximum rate of reaction	1445
Table 6-1. Thickness of kaolinite filter cake with different filtration rate.....	154
Table 6-2. Measured and calculated date for three point loading test.	159
Table 6-3. Results from experiments into optimisation of conditions for the thermal polymerisation of PMMA	161
Table 6-4. Results of three point loading of redox polymerised PMMA and PMMA/Kaolinite composite	164
Table A1-1. Results from XRD traces of GO/PVA composites.....	177
Table A6-1. Flexural strength and modulus of PMMA	185

Table A6-2. Flexural strength and modulus of kaolinite/PMMA composite.....	185
--	-----

Chapter 1

Introduction

1.1 General introduction

The stages of civilization of human beings are named after materials: Stone Age, Bronze Age and Iron Age. The development of materials promotes new leading technologies and promising futures.

In modern and contemporary history, engineers have been looking for a kind of material which has properties like low density, high strength and high elastic modulus. This ‘super material’ could be potentially used in industry especially in the automotive industry.

The global number of cars has exceeded 1 billion [1]. The world consumption of oil was 4.13 Pg (4130 million tonnes) in 2012 as reported by British Petroleum [2]. The greenhouse gas (CO₂) concentration increased in the atmosphere from 277 parts per million (ppm) to 404 ppm between the pre-industrial value on 1750 and June 2016 [3]. It is predicated that global temperatures will increase by 0.2 °C per decade [4]. Fossil fuels are non-renewable energy resources and it is reported [2] that global oil consumption grew by the rate of 1.9 million barrels per day (b/d) in 2015 from the historical average. Compared with the rate in 2014, which is 1.1 million b/d, it shows a significant increase. It is advisable therefore the technologies should be developed to slow down the rate of production of carbon dioxide.

Transport made up 22 % of global CO₂ emissions, which is the second largest producer following electricity and heating, which accounted for 41%. Road transport accounted for about 75 % of transport emissions [5]. Generally, it is found that fuel economy of a vehicle improves by 7 % when there is a 10 % reduction in weight [6]. Decreasing vehicle weight allows manufacturers to achieve the same level of performance with a smaller engine, smaller fuel tank and smaller emissions.

A new generation of cars in which the chassis is made from carbon fibre reinforced composites (CFRC) has been developed by Volkswagen with reported 250 mile per gallon (about 106 km per litre) performance [7] (Figure 1-1).



Figure 1-1. CFRC frame used in VW concept vehicle. [7]

CFRC was invented at the Royal Aircraft Establishment in 1963. Traditional materials, such as cast iron and stainless steel, the strength to weight ratio is around $20 \text{ kNm} \cdot \text{kg}^{-1}$ for cast iron and $30 \text{ kNm} \cdot \text{kg}^{-1}$ for stainless steel, the stiffness to weight ratio is about $12 \text{ MNm} \cdot \text{kg}^{-1}$ and $20 \text{ MNm} \cdot \text{kg}^{-1}$, respectively, as shown in Figure 1-2 [8]. Compared with traditional materials, CFRC itself has big advantages in both strength to weight ratio and stiffness to weight ratio, which are $200 \text{ kNm} \cdot \text{kg}^{-1}$ and $80 \text{ MNm} \cdot \text{kg}^{-1}$, respectively.

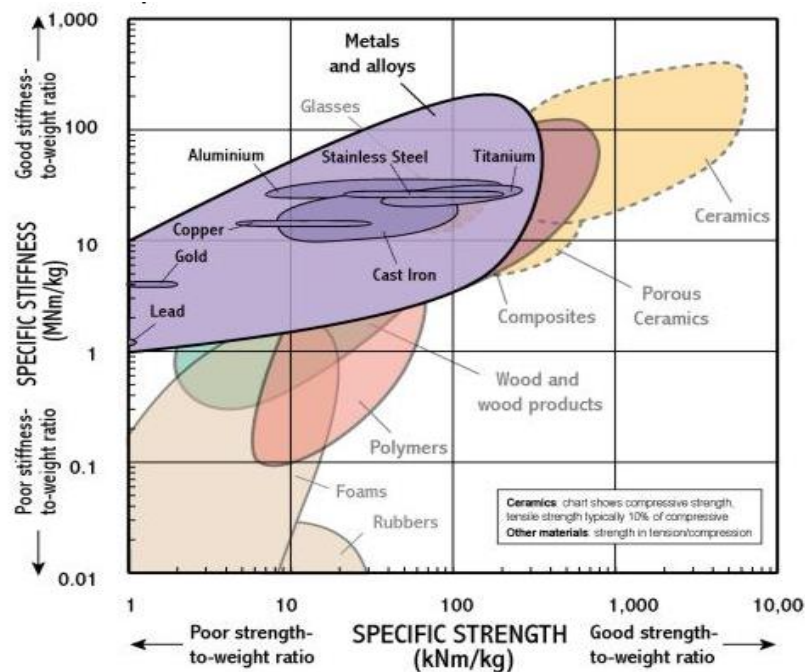


Figure 1-2. Ashby map of strength-stiffness of materials, focusing on metals and alloys. [8]

However, CFRC manufacture is very energy and labour intensive and the resulting capital cost is nearly 10 times than that of glass fibre reinforcement composites and 20 times compared with metals and alloys. This may inhibit the market penetration of such vehicles (Figure 1-3) [8]. In this case, it has taken almost 50 years for CFRC to be used in the industrial automobile as the cost of CFRC decreases with new technologies.

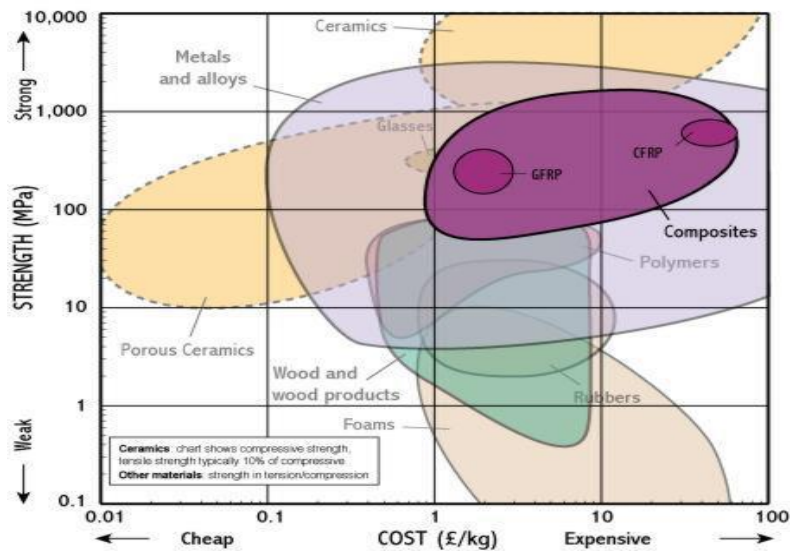


Figure 1-3. Ashby map of strength-cost of CFRC. [8]

Ajay Kapadia, the senior leader of Knowledge Transfer Network on advanced composites materials, points out that ‘carbon fibre composites currently cost five times more than their metallic equivalents. It is unlikely that the cost of carbon fibre will significantly decrease.’ [9]

There have been several attempts to utilize low-cost materials to take the place of carbon fibre composites in car shells. For instance, at the 2014 London Design Exhibition, there was a concept car of which the shell is made of polypropylene and aluminium as shown in Figure 1-4.



Figure 1-4. Low carbon vehicle with polypropylene/aluminium shell.

The challenge now is to produce a cheaper material with higher ratios of strength to weight and stiffness to weight. This research seeks materials for use in industrial processes especially in vehicle body construction that have high strength to weight ratio, high elastic modulus, toughness and low cost compared with currently available composites. The project aims to develop composites that mimic structures found in nature, particularly nacre (mother of pearl). One of the most promising potential choices is polymer-clay nanocomposites.

In 1985, Japanese scientists invented a new kind of composite called polymer-clay nanocomposites (PCN) at Toyota Central Research and Development Laboratories [10]. It became a new promising field for researchers to take part in. Compared with pure polymers, the new composite which consisted of no more than 3 vol. % clay provided better mechanical properties.

In this work, high volume fraction clay composite will be investigated. As part of the introduction to this thesis, the motivation for the work is explained by setting it in the context of an assessment of China. A comprehensive review on the available literature on biomimetic composites is presented in Chapter 2. Details of materials and the methods used are highlighted in Chapter 3. The results and discussion are given in Chapter 4-7. Conclusions are provided in Chapter 8 along with directions for further work.

1.2 Motivation for this research

The motivation of this work was created because the environment in China has become extremely polluted. China has been the second biggest economic system of the world since 2011. It can be suggested that the Chinese population was too entranced by the prospect of wealth to realize what would happen in the context of pollution. In 2012, smog happened in the Chinese capital city Beijing, just as occurred in London in 1952. Thus 60 years later, the situation is even worse than at that time in London. The air quality of major cities in China was given in Figure 1-5. In 2013, 8500 people died because of smog in the major cities in China, such as Beijing, Shanghai, Guangzhou and Xi'an.

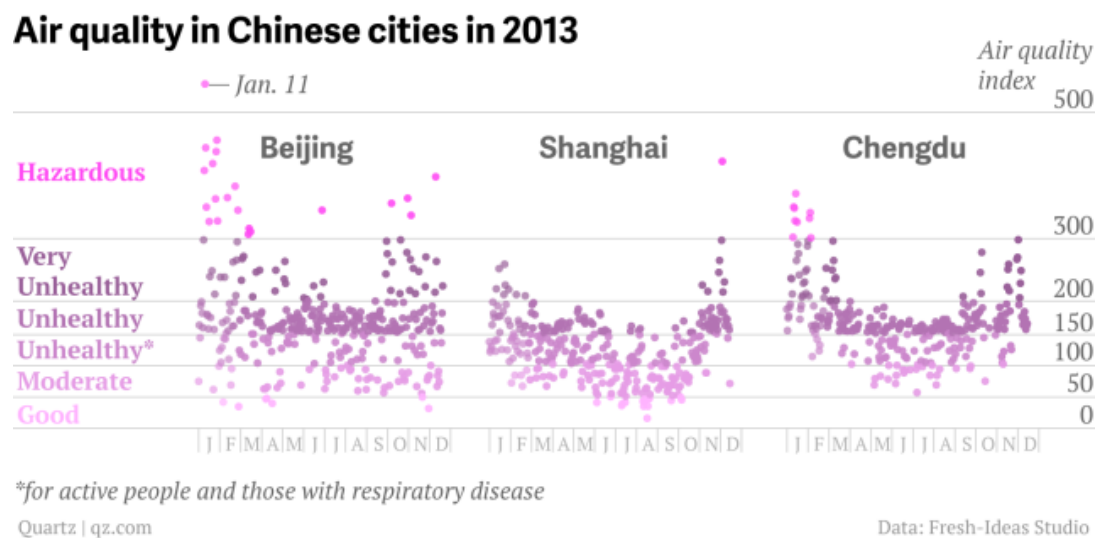


Figure 1-5. Air quality in China 2013. [11]

A journalist James Fallows, mentioned in one public report [11] as ‘at one point in mid-January, Air quality index (AQI) in Beijing soared as high as 993, far beyond levels health officials deem extremely dangerous’. The AQI in London was generally between 20 to 80 in 2013. [12]

Smog appeared in conjunction with the highest density of population. Beyond half of Chinese is suffering this pollution, which is more than 0.68 billion people. One of the causes of smog is vehicle exhaust emissions.

The domestic production of oil in China cannot meet the demand resulting from development. The shortage is becoming more and expanding rapidly. It pointed out that imported oil was about 120 million tonnes in 2004 and will expand quickly in the following decades to fulfil the economic needs [13]. Figure 1-6 shows oil demand in China between 2000 and 2020 [14]. It is estimated from the beginning of 2020, the demands of oil will be up to 500 million tonnes every year [14]. Unfortunately, the domestic oil production can only satisfy less than 40 % of the demand.

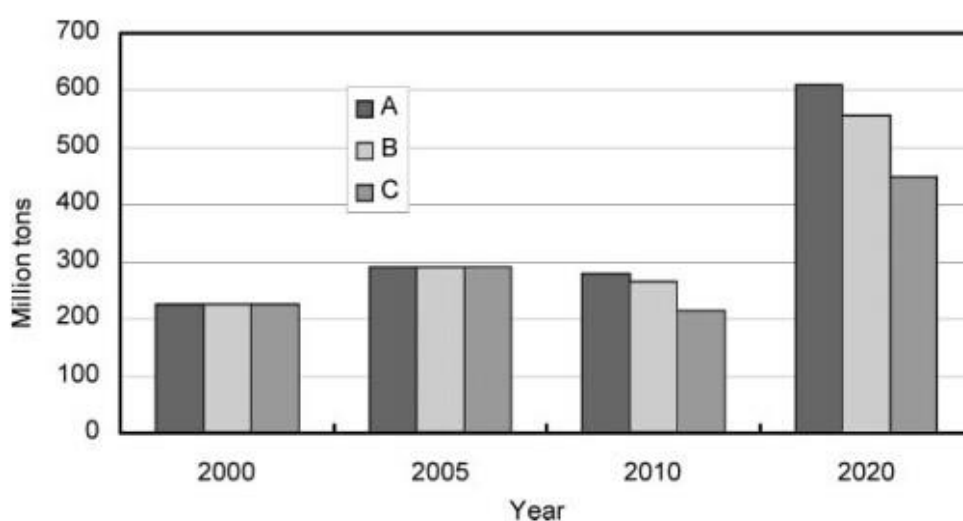


Figure 1-6. Histogram of oil demands in China. A: extrapolation of oil demands between 2000 and 2020. B: extrapolation under a strategy for reducing oil consumption. C: extrapolation under a further reducing oil consumption strategy. [14]

In this kind of emergency, China has to find oil replacements. Abundant coal reserve is the major fossil fuel resource and is about 5500 billion tonnes in China [14]. The ‘proved coal reserve’ is estimated about 115 billion tonnes and almost 40 times compared with the oil reserve in China [14]. Therefore oil substitution technology by means of coal is widely researched and developed. This may give Chinese industry a viable power solution. In other words, Coal-to-Liquid (CTL) technology will play a significant role in the long term for oil substitution production. As Figure 1-7 shows, the oil production through CTL needs water. Some reports reveal that the water consumption of 1 tonne of oil production requires up to 7 tonnes of water. The sulphurous gas emissions caused by coal is also an environment problem [14].

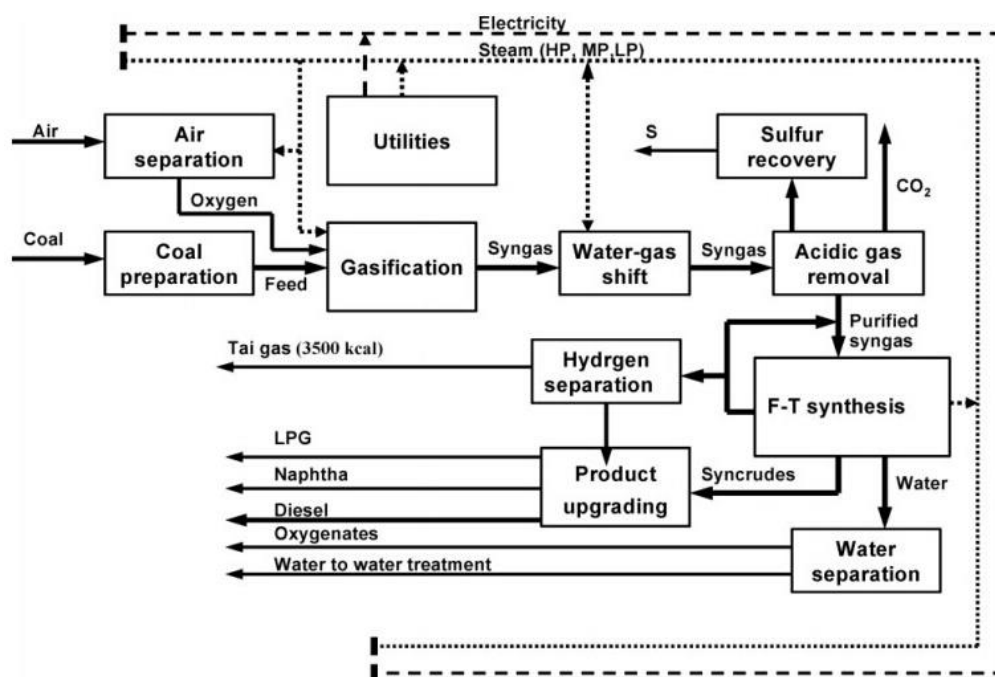


Figure 1-7. The Coal-to-Liquid process (Synfuels China, 2004–2005). [14]

China has already built the world's largest CTL project in Ningxia province. It can produce 4 million tonnes oil per year. In the meantime, it gives the environment a huge burden of pollution.

The aim of this research is to synthesise light-weight ordered composites with high mechanical properties for materials applications in the car industry. The first investigative step is to analyse the mechanism of natural nacre and to biomimetically simulate the structure using clay and polymer via a water-evaporation induced process. Next, acrylic monomers are synthesized for the polymerisation reaction with clay by heating or UV-light polymerisation. The next stage was to use potential reinforcement agents, such as montmorillonite, kaolinite. Such composites should have improved elastic modulus and barrier properties. Subsequently, the interaction of clays with the polymers is studied with the aim of preparing composites based on epoxy resin groups. Furthermore, graphene oxide will be investigated. The ultimate objective is to find appropriate conditions for polymerisation and reinforcement to prepare composites with mechanical properties in the range suitable for composite applications in the automotive industry.

References

- [1] Davis SC, Diegel SW, Boundy RG. Transportation energy data book. 31st Ed. US: Department of Energy, Oak Ridge National Laboratory; 2012.
- [2] Petroleum B. BP statistical review of world energy. UK: Pureprint Group Limited; 2016. p. 5.
- [3] Tans P. (National Oceanic and Atmospheric Administration/Earth System Research Laboratory). Trends in Atmospheric Carbon Dioxide [Internet]. [Accessed 22 August 2016]; Available from: www.esrl.noaa.gov/gmd/ccgg/trends/.
- [4] Change C. Intergovernmental Panel on Climate Change. World Meteorological Organization. 2007. p. 72.
- [5] Quadrelli R, Peterson S. The energy–climate challenge: recent trends in CO₂ emissions from fuel combustion. Energy policy. 2007 Nov 30;35(11):5938-52.
- [6] Cheah LW. Cars on a diet: the material and energy impacts of passenger vehicle weight reduction in the US (Doctoral dissertation, Massachusetts Institute of Technology). U.S.A., 2010. 117.
- [7] Schultz J. Volkswagen Previews Refreshed 261 M.P.G. XL1 Prototype. The New York Times. 2009. p. 35.
- [8] University of Cambridge. Material selection chart [Internet]. [Accessed 02 July 2015]; Available from: http://www-materials.eng.cam.ac.uk/mpsite/interactive_charts/.
- [9] Lawler R. Back to Aluminium. Materials World. 2014;14.
- [10] Treece MA, Zhang W, Moffitt RD, Oberhauser JP. Twin - screw extrusion of polypropylene - clay nanocomposites: Influence of masterbatch processing, screw rotation mode, and sequence. Polymer Engineering & Science. 2007 Jun 1;47(6):898-911.
- [11] Wang H. 2013 will be remembered as the year that deadly, suffocating smog consumed China [Internet]. 19 December 2013. [Accessed 22 August 2016]; Available from: <http://qz.com/159105/2013-will-be-remembered-as-the-year-that-deadly-suffocating-smog-consumed-china/>
- [12] Real-time air quality index [accessed 12 December 2016]; Available from: <http://aqicn.org/city/london/>

-
- [13] International energy agency, CO₂ emission from fuel combustion 2012.
Organisation for Economic Cooperation and Development Publishing, Pairs. 2012
- [14] Hao X, Dong G, Yang Y, Xu Y, Li Y. Coal to liquid (CTL): Commercialization prospects in china. Chemical Engineering & Technology. 2007 Sep 1;30(9):1157-65.

Chapter 2

Literature Review

2.1 Composite materials

Composite material is a type of material which is made up of more than one constituent with different physical or chemical properties. Hull and Clyne found that the composite contains a strong and stiff reinforcement and a softer matrix [1]. The strong and stiff constituent is generally in the elongated form, which is implanted in the softer matrix [1]. There are natural composite materials in the world, for instance, wood and bone. Wood contains fibrous chains of cellulose and the cellulose is combined with lignin to form the wood. Bone has a complex structure with stiff inorganic component embedded in tough organic constituent served as matrix, known as collagen [1]. Composite can be described as materials which consist of 'one or more discontinuous phases embedded in a continuous phase', this definition was given by Agarwal and Broutman [2].

Normally, the discontinuous phase shows stiffer and stronger mechanical properties than the continuous phase. The discontinuous phase in a composite is known as the reinforcement and the continuous phase is named as matrix. The reinforcement of discontinuous material can undertake the applied excess stress and/or load with matrix in the material, hence suppress cracking of the matrix. Therefore, stress and/or load should be transferred between the reinforcement and the matrix through interaction, otherwise the matrix would be over loaded and lead to cracking. Also, the reinforcement mechanism involves absorbing energy before fracture. This is achieved through increasing toughness, for example, fibre pull-out in fibre-reinforced composites when over loaded [2]. The fibre sizes of the traditional polymer composites are in microns levels, while the reinforcement of PCN is usually in the scale of nanometre (1-100 nm), the size of reinforcement is the main difference between traditional polymer composites and PCN. Nevertheless, the aspect ratios can be very high. More interfacial interaction between reinforcement and matrix would be probable since the size of clay particles is $\sim 10^3$ times smaller than that of the traditional fibres [2]. In PCN materials, the clay particles serve as nano-material reinforcement. Unlike a continuous fibre reinforced composite, thermoplastic nanocomposites can be processed by extrusion, injection moulding and similar processes.

2.2 Structure of polymer-clay nanocomposites

There are three types of structure that develop in PCN when polymers are introduced to clays—conventional, intercalated and exfoliated. Most composites are made up of a mixture types. Basal spacing is defined as the distance between the (001) plane in the unit cell and the (001) plane in the next unit. If the polymer does not enter the galleries (basal spacing does not change), the composite is designated ‘conventional’. An increase in basal spacing indicates the polymer enters into clay’s interlayer, but the clay can still keep its structure; it is called intercalated. If the polymer penetrates the clay galleries in the meanwhile the polymer breaks down the layered structure, resulting in the platelets separating and the clay layers are evenly distributed among the polymer, the structure is called exfoliated [3]. Figure 2-1 indicates the three modes of PCN structure.

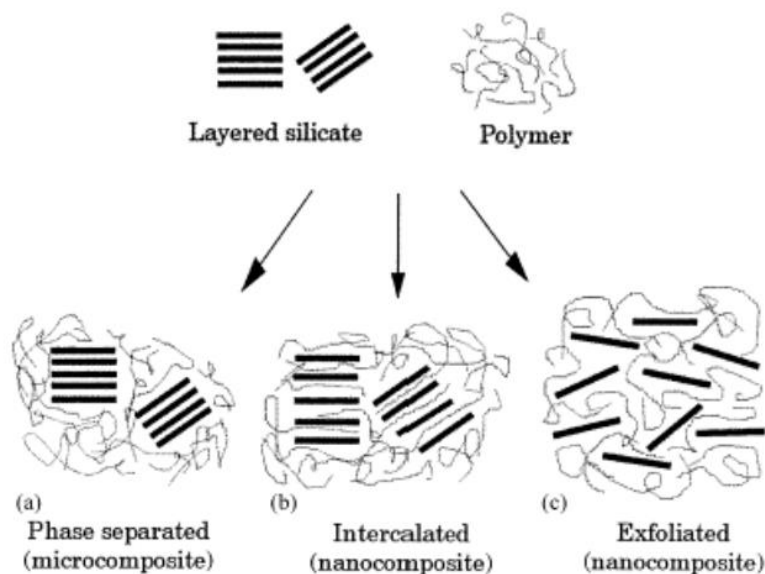


Figure 2-1. Different structures of PCN. [3]

2.3 Principles of biomimetics

Biomimetics is an interesting idea to simulate the way that nature has used to survive. Nature has used more than five millions of years to evolve and adapt [4]. Thus there is an assumption that some mechanisms for survival developed in this time are thought to be the best and the simplest.

This research is biomimetic as it attempts to develop a strong and light as well as high strength and tough high-performance material. A composite with such properties already exists in nature and it is called nacre, sometimes referred to as ‘mother of pearl’ because of its optical lustre.

2.3.1 The properties of nacre

Nacre, which arises about 600 million years ago, can prevent molluscs being eaten by their predators and being harmed from stone or tide with their protective structure [5, 6]. The creature itself creates the superb structure at ambient conditions using abundant calcium-based materials, mainly aragonite (calcium carbonate). They can combine calcium carbonate with their own protein to form a layered structure, the inner side of which is iridescent (Figure 2-2) [4].

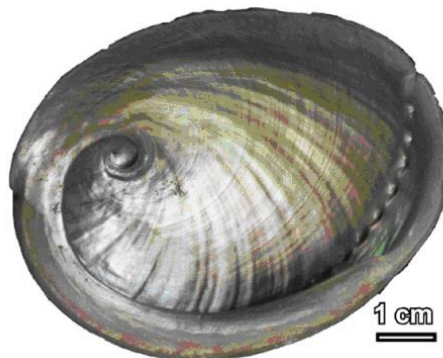


Figure 2-2. Photograph of the inner, iridescent region of the nacre. [4]

In the 1960s to 1980s, researchers have investigated the layered structure of nacre by scanning electron microscopy (SEM). Figure 2-3 shows the structure of nacre [4, 7, 8].

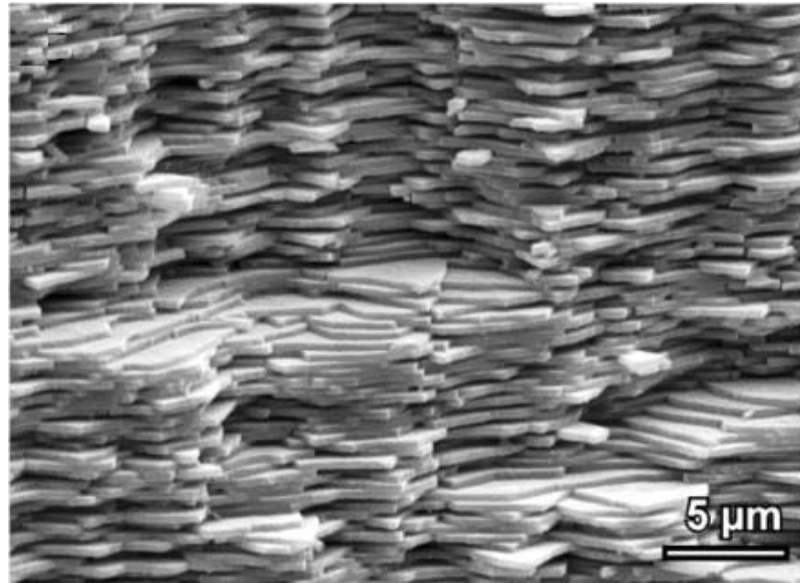


Figure 2-3. SEM image of fracture surface of nacre. [4]

The layers grow confluent and are highly organised as an ordered mineral structure, shown in Figure 2-4. This material which is created by the mollusc with a small amount organic component (about 5 wt. %) between mineral layers gives nacre itself outstanding mechanical properties. The hierarchical structure can be up to 2000 layers. The single aragonite platelet (or tablet) is 5 to 10 μm in diameter and the height is around 0.5 μm.

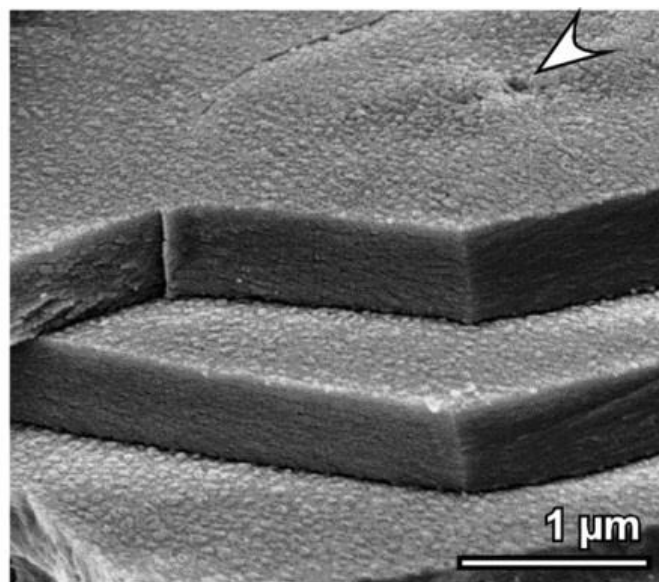


Figure 2-4. High magnification view on the platelets of nacre. Corrugated surface as white arrow point out. [4]

In the meanwhile, there is another hierarchical level called a mesolayer which is caused by temperature and food fluctuations (Figure 2-5). Generally, a mesolayer is around 20 μm thick. It is made of organic material and is reported to 'appear approximately every 300 μm separating regions of regular platelet stacking' [9-12].

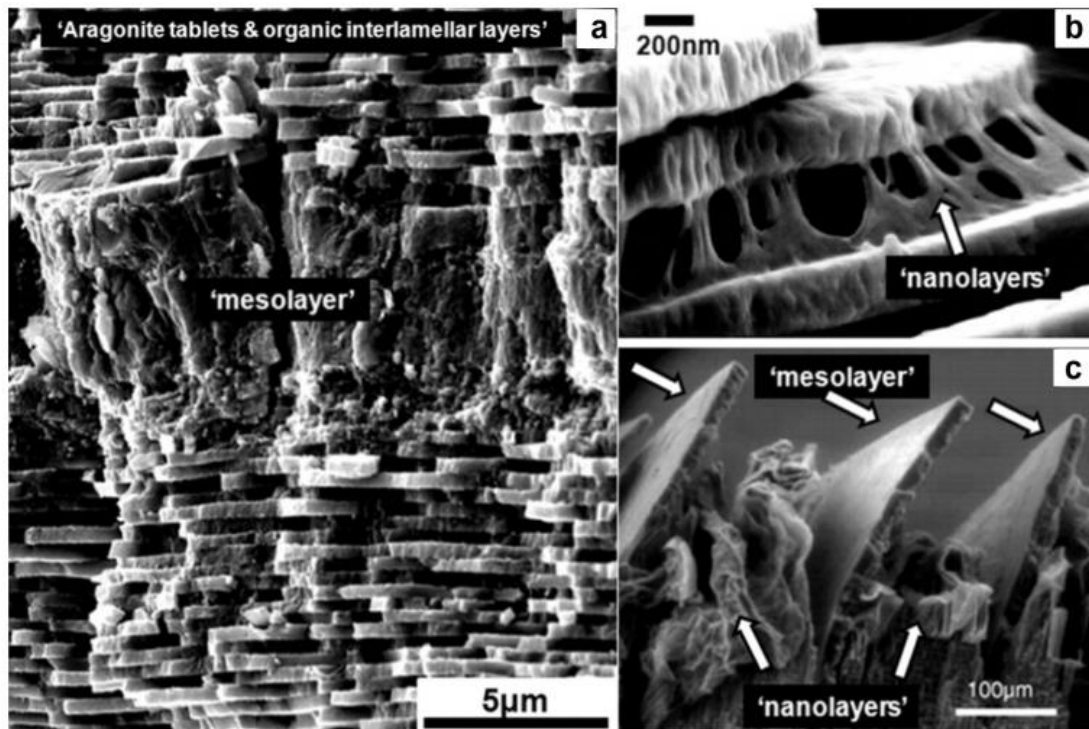


Figure 2-5. (a) Fracture surface of nacre showing the brick-mortar structure separated by mesolayer. (b) Nanolayer of nacre and organic membrane. (c) Mesolayer and nanolayer within a partially demineralised nacreous structure. [4]

The process of shell formation is described as an 'organic matrix-mediated' [13] process. During growth, the organic part can be added into inorganic layers as long as the mineralization happens. Nacre can organize the structure by forming inorganic and organic layers alternatively using molecular recognition and interactions. Therefore, nacre gets a highly controlled structure using both inorganic and inorganic materials to deliver mechanical properties and organic beauty as well as humid and corrosion resistance in the sea [13, 14].

The material can be defined as a self-assembled polymer/mineral composite. This material has outstanding properties which have drawn lots of attentions from different disciplines, especially in material science [15]. The organization of nacre

has inspired numerous interesting ideas, some of them are shown in Figure 2-6.

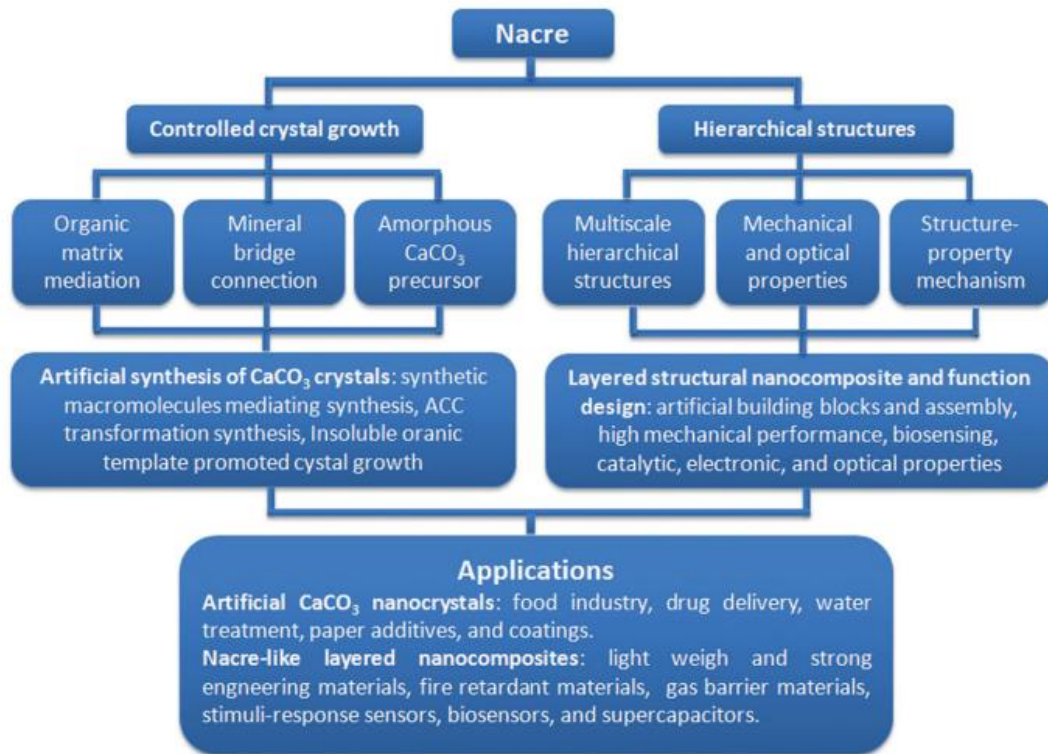


Figure 2-6. Summary of nacre inspiration in advanced materials applications. [15]

Nacre, made of 95 wt. % calcium carbonate and 5 wt. % protein with $K_{IC}=3-10 \text{ MPa}\cdot\text{m}^{1/2}$, has achieved 100 to 1000 times tougher than that calcium carbonate from which it is made [16]. Tensile strength can be up to 40-100 MPa [17] and Young's modulus is 60-70 GPa [18]. The 5 wt. % organic parts are generally embedded in the interface between tablets [17]. The organic fraction can affect the toughening mechanism of nacre due to cohesion between the tablets in a certain distance [11].

As mentioned before, the three dimensional aragonite tablets are about $0.5 \mu\text{m}$ thick and $5-10 \mu\text{m}$ in diameter. In columnar nacre, the tablets are arranged in columns [17] while in sheet nacre, they arrange in a random way, shown in Figure 2-7.

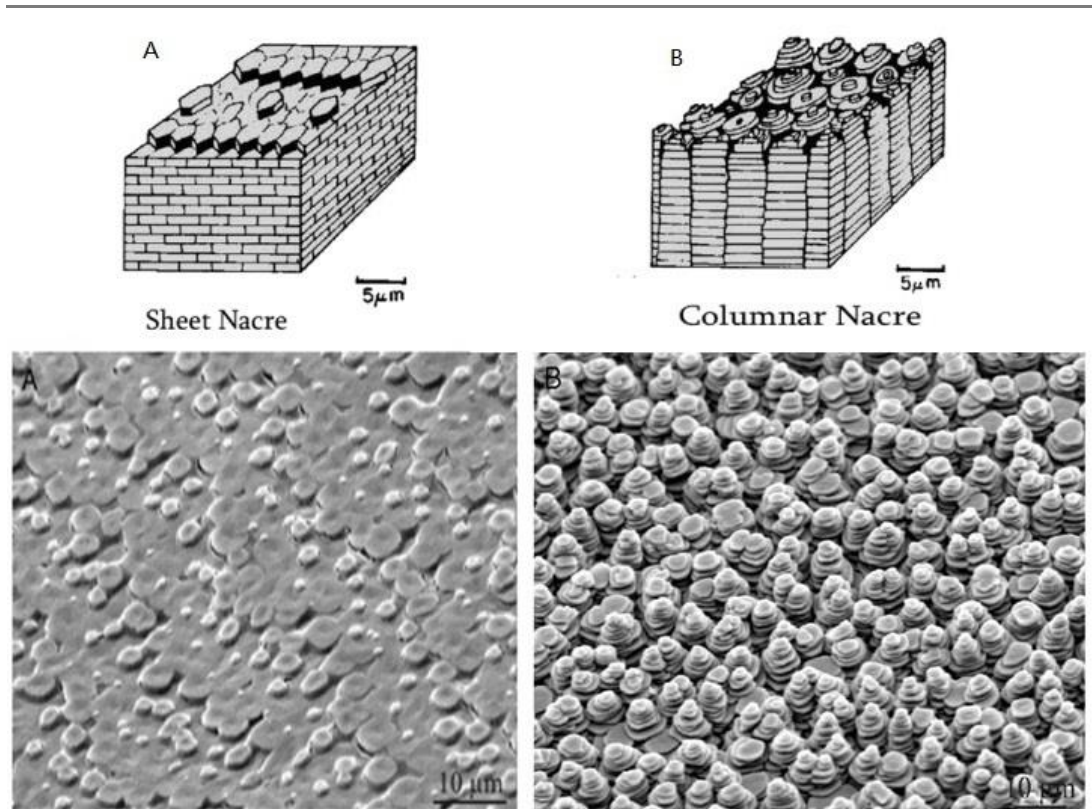


Figure 2-7. Schematics of sheet nacre and columnar nacre and their SEM picture. [19, 20]

From 1970 to 1995, it is believed that the tablets are made up of a few twinned small crystals [21]. However, recent reports [22, 23] using atomic force microscopy show that the tablets are composed of nanograins or called nanoasperities instead (Figure 2-8), and are separated by a well-designed network of organic protein [11].

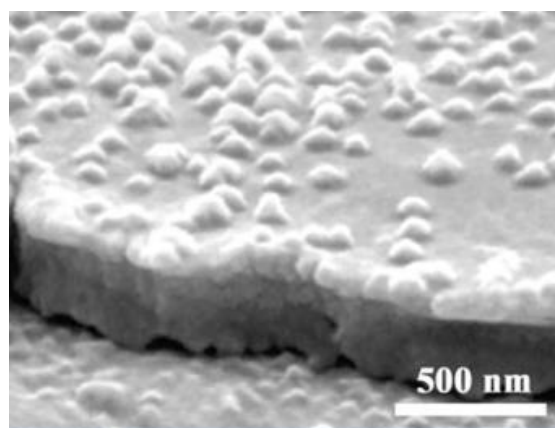


Figure 2-8. Nanograins on the aragonite tablets. [11]

Because of the nanoasperities, nacre can interlock the tablets between each other resulting in great mechanical properties. When tensile loaded in the direction parallel to the tablets, the nanoasperities can limit crack propagation as indicated in the schematic Figure 2-9 [4].

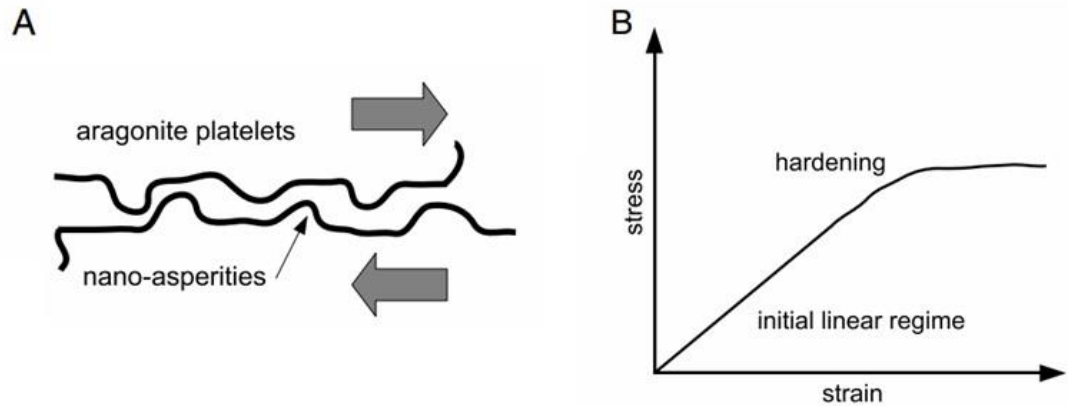


Figure 2-9. (A) Schematic of two platelets with nanoasperities during sliding (B) The stress–strain curve of nacre shows the hardening mechanism. [4]

The aragonite tablets are stacked vertically and connected tight with the adjacent parts. Among these tablets, there was 5 wt. % protein which act as glue to stick them together (Figure 2-10 and 2-11). When subjected to tensile loading, the soft organic bio-polymer between tablets can endure high stretching and dissipate energy by visco-plastic deformation [4, 24].

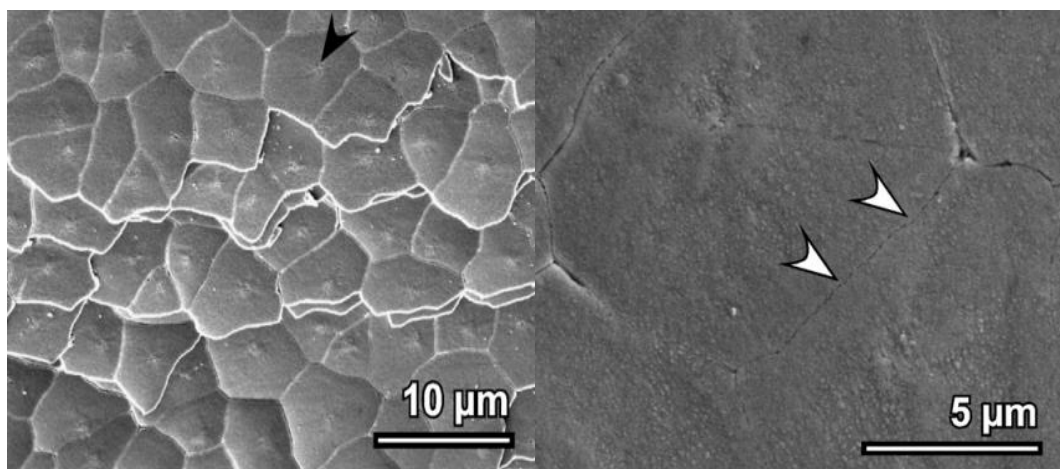


Figure 2-10. SEM images of fracture surface of shell. A distinct structure is observed in each platelet as black arrows indicated. High magnification view on the platelets shows their connection (white arrows). [4]

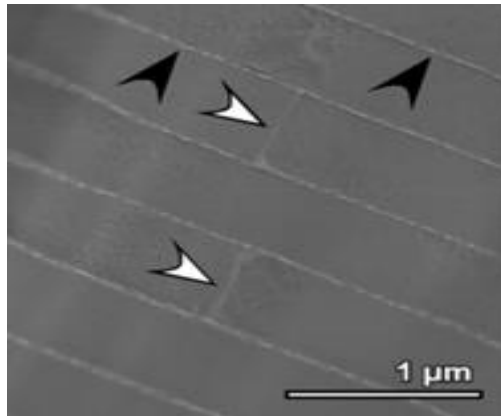


Figure 2-11. Transmission electron microscopy (TEM) image of nacre shows the organic phases are connected with each tablet. [24]

Mineral bridges, which are embedded in organic layers, have been confirmed as another toughening mechanism in nacre (Figure 2-12) [25].

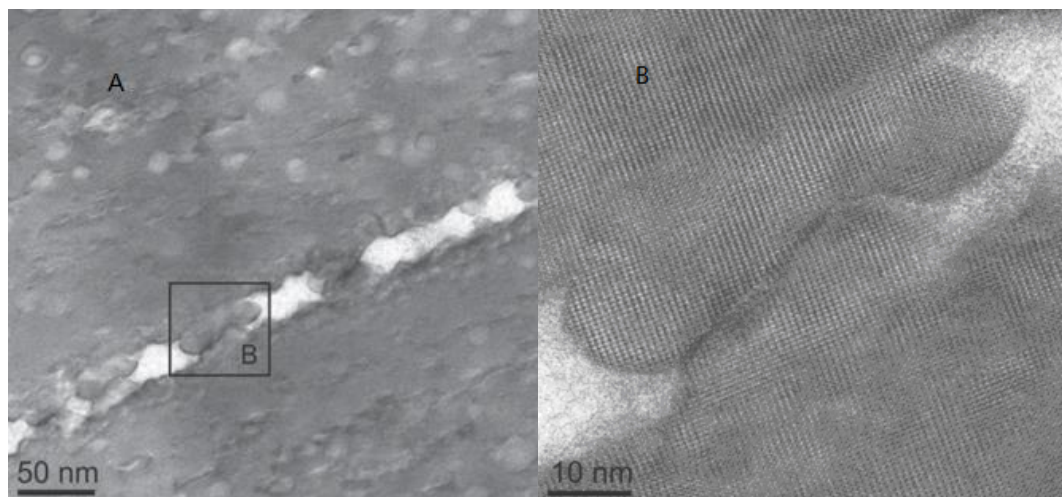


Figure 2-12. Mineral bridges in nacre. [25]

Meyers and Lin reported that when loaded parallel to the tile direction in nacre, two principal mechanism of failure may occur, one is failure of the tile and another is sliding along the tile surface [10, 11]. In this case, the nanoasperites on the surface of aragonite tablets can inhibit the sliding movement of the tile. The mineral bridges among these bricks can interlock the bricks and the organic protein which can act as glue to limit the sliding to a certain distance. These three different models synergize together resulting in the high mechanical properties of nacre, and they are shown as schematics in Figure 2-13 and 2-14 [11, 26].

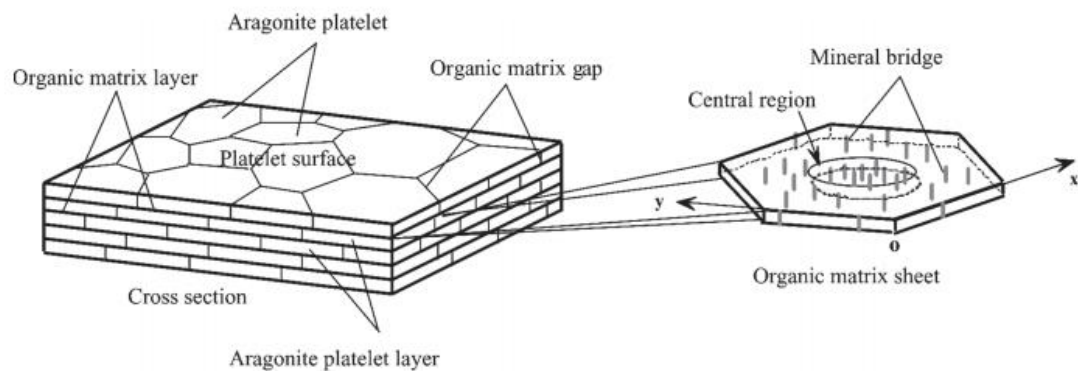


Figure 2-13. Sketch of the structure of nacre and a single platelet of nacre. [26]

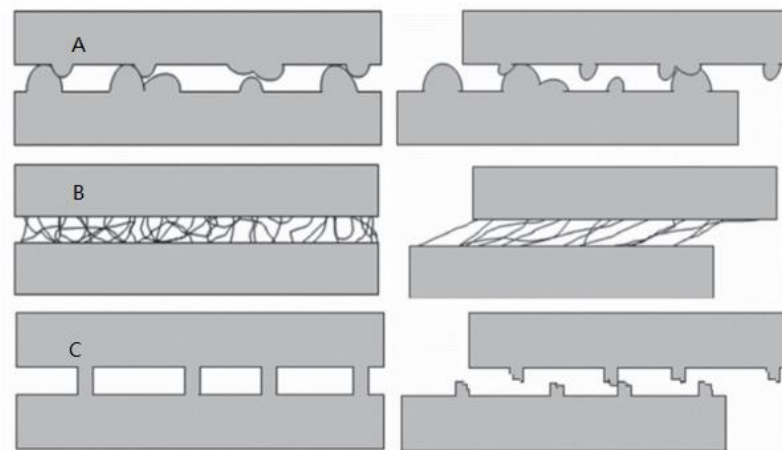


Figure 2-14. Three mechanism models during sliding between platelets. (A) Nanoasperities hardening (B) Organic stiffening (C) Fractured mineral bridges toughening. [11]

Inspired by nacre, this work attempts to simulate 'bricks and mortar' structure and intends to achieve this by adding polymer (which is intended to act in the same way as protein) into high volume fraction clay or graphene oxide (to act as calcium carbonate) ordered structures.

2.3.2 Attempts to replicate the nacre structure

In 1998, poly (dodecylmethacrylate) (PDM) /silica nanocomposite was prepared by Sellinger et al., which is a dip-coating self-assembly approach [27]. This process began with mixing silicate solution and monomer in assistance with coupling agent,

surfactant and initiators in an ethanol/water solvent [27]. The ethanol evaporated during dip-coating, so the concentration of nonvolatilizable components increased and formed micelles in the solution. The formation of the composite was promoted by the continuous evaporation of ethanol. This leads to prompt organization of reinforcement and matrix precursors into a laminated structure together. The organic polymerisation can be induced by application of light or heat to stabilize the structure of composite and to generate covalent bonds at the interfaces between matrix and reinforcement. The hardness increased from 0.1-0.4 GPa to 0.8-1.0 GPa through polymerisation, measured by the nanoindentation of the nanocomposites [27].

Layer-by-layer assembly (LBL) was investigated to mimic the nacre structure in 2003 [28]. LBL relies on combination of different charged clays and polyelectrolyte to generate a hierarchical structure in nanoscale. In the films, ordered clays were cooperated with polymer to create covalent and hydrogen bonding. When loaded, load transfer can occur between clay sheets and the polymer resulting in good mechanical properties. Cationic poly (diallyldimethylammonium chloride) (PDDA) and anionic montmorillonite (MMT) were used to form layered structures using LBL. The PDDA/MMT nanocomposites show high mechanical properties. The tensile strength of the composite films obtained was 106 MPa due to the strong attractive electrostatic and van der Waals interactions at the interface of MMT platelets and the polymer chains [28]. Moreover, poly (vinyl alcohol) (PVA)/MMT layered composites have also been prepared by this method [29]. The film has high flexibility and transparency. After glutaraldehyde cross-linking, tensile strength of the film reached 400 MPa and 106 GPa Young's modulus was obtained. The acetal bridges after cross-linking, the hydrogen bonding between PVA and MMT, and the Al-O-C bonding forming by organic-inorganic phases contributed to the high mechanical properties of composite. Various polymers have been combined with MMT to prepare the nacre-like structure via LBL by the same group [30, 31].

Bennadji-Gridi and co-workers reported the preparation of films by slowly evaporating the MMT suspension and sodium hexametaphosphate (HMPP) or sodium polyacrylate (SPA) mixture in 2006 [32]. They obtained a nacre-like sample, the platelets overlapped each other and the direction of platelets was parallel to the

original substrate, as indicated in Figure 2-15 [32]. A three point flexure testing was carried out to analyse the mechanical properties of the film. The bending strength of the thinner samples were 112 MPa, whereas the thickest samples ($>140\text{ }\mu\text{m}$) showed a much lower value about 45 MPa [32]. This is caused by the numerous perpendicular cracks to the film surface which may be created when the water was evaporating. It is reported that the bending strength of samples increased when decreasing the rate of evaporation [32].

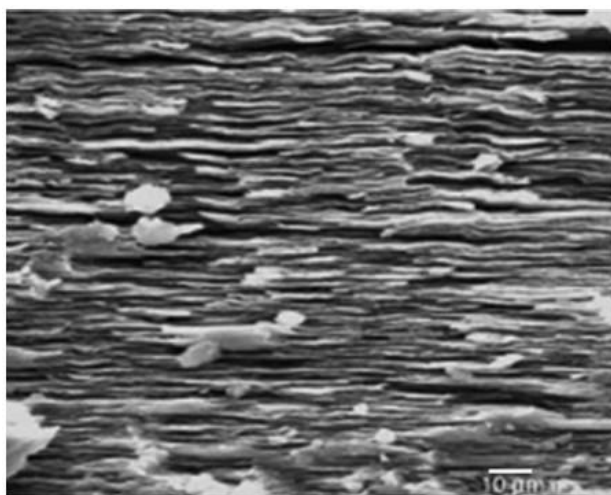


Figure 2-15. A cross section of the composite film prepared by evaporation. [32]

Lamellar nanocomposite materials have been generated by evaporation-induced self-assembly [33]. The material was created by forming the poly (tripropylene glycol diacrylate) (PTPGDA) and indium–tin–oxide (ITO) layers alternatively [33]. As ethanol/water solution evaporated, the concentration of the non-volatile constituents increased. The continuous evaporation promoted the combination of the reinforcement and matrix components, resulting in production of layered structure. A free-radical polymerisation process was then carried out to generate a polymer/ITO composite with average layer spacing of 3 nm [33].

Ice-templated, or freeze casting is the method to simulate the structure of nacre by Tomsia and co-workers [34-36]. The method was illuminated by eliminating the solutes from the suspension during ice formation when cooled to low temperature. Eliminated solutes were then entrapped in the gaps between each ice crystal. Tomsia et al. prepared a water-based suspension which was made of 50 wt. % of alumina

particles and organic additives [34], followed by cooling the suspension to $-80\text{ }^{\circ}\text{C}$. At this stage, the lamellar ice grows directionally desorbing the Al_2O_3 particles, thus a template was formed by Al_2O_3 particles and acted as the ceramic scaffold. Then the obtained templates were freeze-dried to get rid of water, fired to $400\text{ }^{\circ}\text{C}$ for the organic additives removal, and finally sintered at $1500\text{ }^{\circ}\text{C}$ for creating a ceramic scaffold [34, 35].

This ceramic scaffold was used to generate the nacre structure by infiltration with a polymer under a perpendicular pressure to the lamellae. The polymer was used to produce a dense packed structure as well as consolidate the composite. The thickness and length of these sintered ceramic layers were in the range of $5\text{--}10\text{ }\mu\text{m}$ and $20\text{--}100\text{ }\mu\text{m}$, respectively [34, 36]. Poly (methyl methacrylate) (PMMA) was then infiltrated into the ceramic scaffolds. The average thickness of the polymer layers is $1\text{--}2\text{ }\mu\text{m}$, acting as the protein layers in nacre [34, 36]. The structures are shown in Figure 2-16.

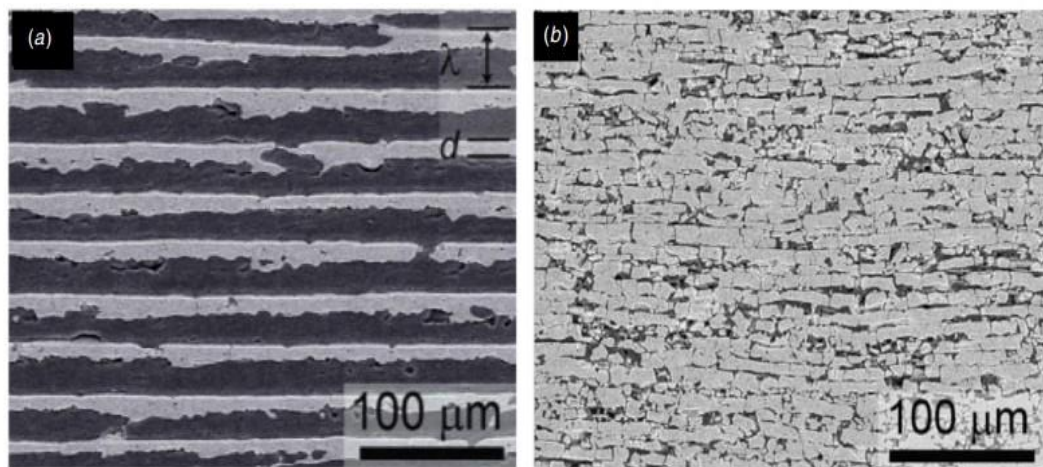


Figure 2-16. (a) The Al_2O_3 -PMMA lamellar structure prepared by ice-templated (white: ceramic; black: polymer). (b) The nacre-like structure produced by pressing and sintering the lamellar scaffolds. [34]

In a bending test, this kind of hybrid material produces similar stress-strain curves compared to nacre. Before failure, the inelastic deformation of both materials were higher than 1% . The flexural strengths of lamellae and the nacre-like structures were 120 and 210 MPa , respectively. Whereas the flexural strength value of alumina was 320 MPa and natural nacre was 135 MPa . In terms of the fracture toughness, both

composites are higher than that of natural nacre [34-36]. The flexural strength can further improved by reducing the thickness of the ceramic layers and the crack-initiation fracture toughness can increase as well. The flexural strength can be determined by adjusting the cooling rate during the free drying stage, the particle size of alumina, additives as well as the suspension concentration [37-39]. It also can be promoted by chemically grafting a methacrylate group on the surface of alumina particles before infiltrating the polymer in to form robust bonding between organic-inorganic system [34, 36]. It was also reported that the chemical grafting increased the strength by 80 % and toughness of the nacre-like structure 70 %, respectively [34]. This is because of organic polymer which is located between the inorganic layers acts as viscoelastic ‘glue’ that allows interfacial sliding but in a limited range.

Electrophoretic deposition (EPD) is another method to generate films rapidly with adjustable thickness and shape. Since 1970s, EPD has been widely operated to obtain advanced ceramics and now it has been applied to produce layered nanocomposites [40]. It depends on the motion of charged particles which can gather at corresponding electrode under applied electric field. To obtain a layered composite, EPD is operated by depositing clay alone into an ordered structure, then infiltrating the polymer into clay layers. It can also achieved by depositing clay and polymer at the same time if they are dispersed homogenously in the suspension [40].

Lin et al. produced a nacre-like structure using gibbsite nanoplatelets and poly (ethylenimine) (PEI) [41]. Different potentials were applied to suspension in a parallel plate cell. Gibbsite and PEI were adsorbed to the cathode to generate composite. The preferred direction of formed nanoplatelets is parallel to the electrode. The results of nanoindentation measured on the coatings illustrated that the reduced modulus of the coating depends on the contact depth add ranges from 2.20 to 5.17 GPa. The modulus of the composite was 0.4 GPa which was lower than that of gibbsite films [41]. This is caused by the soft PEI component located between the gaps of the hard clay layers. In another study, using sol-gel method, Liu obtained the surface roughness which was similar to that of nacre by coating silica onto the surface of gibbsite [42]. After polymerisation of photosensitive monomer, the cured polymer was penetrated in the galleries between the clay layers to create the composite. The tensile strength of the composite was around 30 MPa, and the

toughness was 10 times higher than that of the PEI [42].

Hot-press assisted slip casting (HASC) is another technique to generate layered structure, which has been used to obtain Al_2O_3 /epoxy resin composites [43]. The composite is produced in the following steps: Firstly, the alumina and epoxy resin were mixed together, then the mixtures were poured into a mould, followed a hot-pressed procedure for half hour at 150 °C for polymer curing. The loading pressure forced epoxy resin matrix to flow among the whole mould and aligns alumina perpendicular to the pressing direction. The obtained composite was made up of around 60 vol. % highly ordered alumina [43]. The microstructure was shown in Figure 2-17.

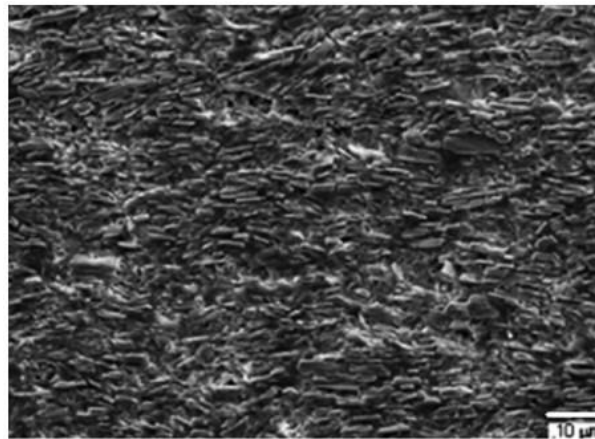


Figure 2-17. The cross section of the Al_2O_3 /epoxy resin nacre-like composite obtained by HASC. [43]

Three-point bending measurement illustrated that fractures occur along the interface of two components due to debonding between alumina and epoxy. To compare the performance of composite with pure epoxy, the flexural modulus of epoxy resin were 2.78 GPa, the strength was 122 MPa, while the flexural modulus of the composite were significantly improved to 19-23 GPa and the strength increased to 133-155 MPa. The flexural strength of the composite was close to that of natural nacre which is 135 MPa [34, 36].

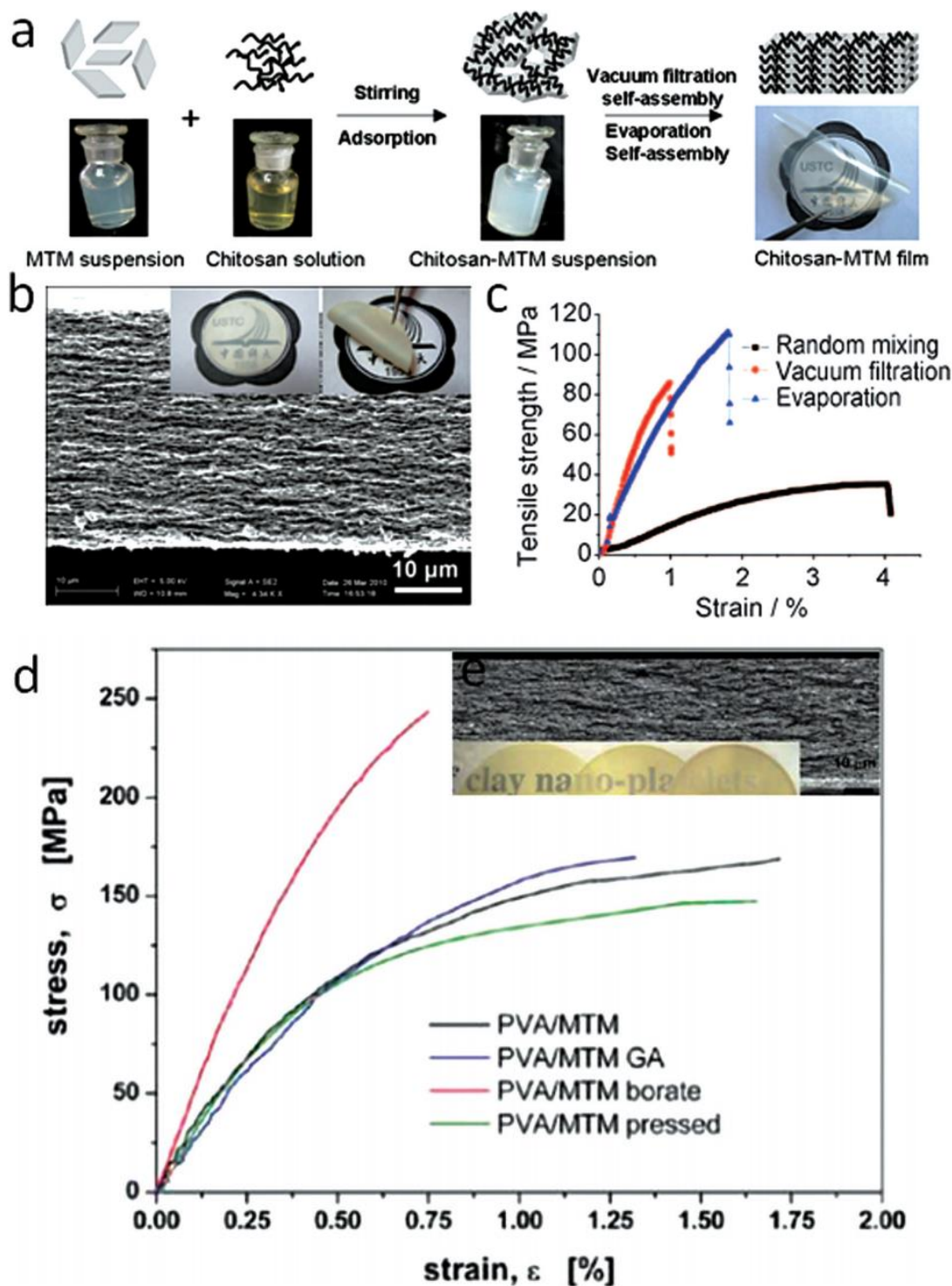


Figure 2-18. (a) Processes of the artificial chitosan/MMT films. (b) Cross section of the chitosan/MMT film. (c) Stress-strain curves of chitosan/MMT film. [44] (d) Stress-strain curves of PVA/MMT film. [45] (e) Samples prepared by evaporation and SEM image of cross-section of the composite.

In recent years, a self-assembly method has been used to produce the clay based

ordered composite. Compared with LBL techniques, this process is simple and timesaving. Yao and co-workers [44] and Walther's group in Helsinki [45, 46] produced layered polymer/MMT composite using this method. The clay nanoplatelets were covered by polymer randomly during mixing and stirring, followed by centrifugation to remove excess polymer. The ordered composites is formed after self-assembly process (Figure 2-18) [44, 45].

The tensile strength of chitosan/MMT nanocomposite films is as high as 100 MPa due to the load transfers from chitosan to MMT layers. (Figure 2-18 (c)) [44]. The mechanical properties can be further improved by adding cross-linking agent into ordered nacre-like PVA/MMT nanocomposite films. The tensile strength and Young's modulus for the composite with glutaraldehyde cross-linking are 165 MPa and 27 GPa, respectively; while with boric acid cross-linking, the values can reach to 248 MPa and 50 GPa. (Figure 2-18 (d), (e)) [45]. Furthermore, PDDA/MMT hybrid film with counter ions can be generated with the same method, but with different charges due to the counter-ion exchange mechanism [46]. It is reported that the higher charge of the counter ions enhanced the mechanical properties. To be specific, the tensile strength of the composite with PO_4^{3-} increased to 151 MPa and Young's modulus of the hybrid composite with PO_4^{3-} reached 33 GPa.

In 2012, Li and Zeng [47] obtained nacre-like structure using calcium carbonate nanotablets (CCNs). They made the calcium carbonate particles by mixing CaCl_2 and urea together, then adding hexadecyl-trimethylammonium bromide (CTAB), ethylene glycol (EG) and polyoxyethylene sorbitan monolaurate (Tween-20) in the solution. The CTAB, EG and Tween-20 can inhibit the nanoparticles growth and stabilize the structure of it. The solution was then heated in autoclave, centrifuged and washed to obtain the final CaCO_3 nanoparticles. The wet CaCO_3 nanoparticles were then mixed with gelatine and through vacuum evaporation to obtain the nacre-like composite. The ultimate strength of layered composite was 97 ± 4.6 MPa, and Young's modulus can be as high as 4.5 GPa. The mechanical properties of different artificial nacre-like composites are given in Table 2-1.

Table 2-1. Summary of artificial nacre-like nanocomposites.

Layered composite	Method	Inorganic fraction /vol. %	Tensile strength /MPa	Young's modulus /GPa	Years	Ref.
PDM /silica	Dip-coating	N/A	N/A	N/A	1998	27
MMT/PDDA	Layer by layer	30	106±11	11±2	2003	28
MMT/PVA	Layer by layer	50	150±40	13±2	2007	29
MMT/PVA with GA cross-linking	Layer by layer	50	400±40	13±2	2007	29
MMT/HMPP	Evaporation	87.7*	N/A	N/A	2006	32
TPGDA/ITO	Evaporation	N/A	N/A	N/A	2006	33
Al ₂ O ₃ /PMMA	Ice-template	80	160	N/A	2008	34
MMT/Polyacrylamide	Electrophoretic deposition	89.6*	N/A	16.92	2007	40
MMT/Chitosan	Vacuum filtration	60	100	10.7	2010	44
MMT/PVA+borate	Vacuum filtration	50	248±19	45.6±3.9	2010	45
MMT/PDDA+ PO ₄ ³⁻	Vacuum filtration	50	151	33	2010	46
CaCO ₃ /Gelatine	Vacuum evaporation	19.1*	97±4.6	4.5	2012	47

* recalculated from weight percentage with density of 3100 kg·m⁻³ for MMT, 2480 kg·m⁻³ for HMPP, 1320 kg·m⁻³ for Polyacrylamide, 2711 kg·m⁻³ for CaCO₃ and 1300 kg·m⁻³ for gelatine.

2.3.3 Factors influencing self-assembled montmorillonite during drying

Walley and co-workers designed a series of experiments on different factors influencing the structure of dried clay layers. These factors included the concentration of clay, pH value and drying rate, each of which influences the

structure of composites [48].

Walley found that the ordered microstructure generated from a 1 wt. % untreated montmorillonite suspension can obtain the structure compared with films generated from 2-3 wt. % suspensions [48], while the structure deteriorated when the composition of clay increased further. When the composition of clay increased to 5 wt. % in the suspension, the structure of clay was disordered. The reason is that the 5 wt. % has high viscosity, and it is hard for MMT platelets rotation. Thus, it suppressed the movement of particles to obtain ordered layers. During drying, the concentration of suspension was increased from 5 wt. % [48]. This implied that the ordered structure was generated in a low concentrated suspension, where platelets were able to rotate in the suspension and the subsequent drying process latched the platelets in fixed position. The appearance of drying cracks and high radius were accompanied by the microstructural change, which was not observed in the film obtained from clay with lower concentrations. Hence the disordered microstructure had degraded mechanical properties because of weak interface interactions [48].

Considering the influence of pH value, under lower pH condition, the viscosity increased due to H^+ ions binding to the edge of layers. This can promote the edge-face interactions. While at a higher pH value, platelets dispersed well. Although layered structure can be generated in all cases, the clay tactoids were curved under lower pH conditions [48].

The drying rate is another important factor which can influence the quality of texturing, ordering (scientifically) and manufacturing time (commercially). The self-drying process of clay films has a lower opportunity cost compared with other methods, such as LBL and ice-templated, since no labour and few capital inputs are required. Therefore, it can be tolerated for the slow drying rate, because of higher structural order and lower opportunity cost.

A higher temperature or air flow can lead to a faster drying rate. Through the SEM figures, Walley [48] found the film was generated irregularly with replete with cracks at the fastest rate ($231 \text{ nm}\cdot\text{s}^{-1}$). The SEM showed layered structure of the composite, but it is accompanied by undulations, scrolls and distortions [48].

2.3.4 Introduction of electric double layers and zeta potential

When dispersed in suspension or emulsion, particles usually bring a negative charge because of (1) chemical groups at the surface of the particle that can ionize leading to a charged surface; (2) chemical compounds adsorbed by the particle leading to a charged surface [49]. Some properties of suspension or emulsion are determined by the charge amount of particles.

When the nanoparticles carry a negative charge, positive ions in the solution could be adsorbed strongly at the charged surface of the particles [50]. The charge of the particles can influence the ion distribution nearby. An electrical double layer (EDL) is organised at the interface of particle-liquid system [51]. An EDL is usually divided into two parts: an adsorbed layer or an inner layer formed by tightly bonded particle surface and ions; and a diffuse layer or an outer layer where the ion distribution contributes to the balance of electrostatic attractions and thermal motion of ions, as shown in Figure 2-19. The electric potential between the adsorbed layer and diffuse layer is called Zeta potential. The value of Zeta potential commonly ranges from +100 mV to -100 mV [52]. At a sufficient distance, the potential can be as the same as the bulk solution value [51].

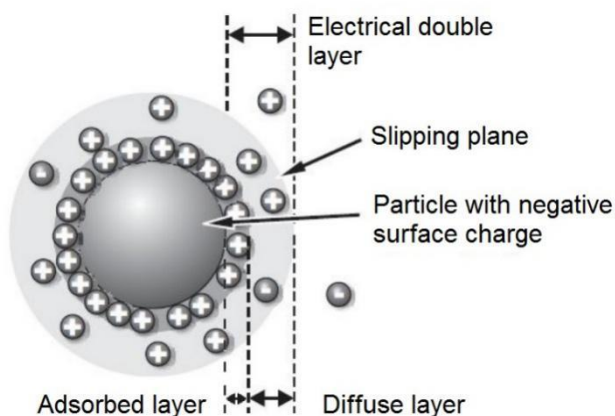


Figure 2-19. Electric double layer surrounding nanoparticle. [52]

The value of the Zeta potential can be used to predict the stability of colloid. High degree of stability can be obtained with Zeta potential values higher than +25 mV or lower than -25 mV of the nanoparticles [52]. Dispersion will tend to aggregate with a low value because of the dominant van der Waals inter-particle attractions. When the

potential equals zero, the colloid will precipitate into a solid [53]. The relationship between the stability and value of Zeta potential is summarized by Riddick in Table 2-2 [50].

Table 2-2. The relationship between the stability and value of Zeta potential. [50]

Stability characteristics	Avg. Zeta potential (mV)
Maximum agglomeration and precipitation	0 to +3
Range of strong agglomeration and precipitation	+5 to -5
Threshold of agglomeration	-10 to -15
Threshold of delicate dispersion	-16 to -30
Moderate stability	-31 to -40
Fairly good stability	-41 to -60
Very good stability	-61 to -80
Extremely good stability	-81 to -100

The charged particle can be moved under an electric field. The amount of the charge determines the speed of the movement. Generally, a bigger charge on a particle moves it faster [49]. In an electrophoretic process, the Zeta potential depends on the moving rate of charged particles. Zeta potential is widely used in many industrial applications such as ceramics, pharmaceuticals, medicine, mineral processing, electronics and water treatment [54].

2.3.5 Clay and electric double layers

The adsorbed layer is a thin layer of hydrated cations and it is close to the clay particle surface. The thickness is generally several angstroms. Adsorbed cations and clay particles move together and they are difficult to separate due to the high concentration of ions and the small distance between layers which gives rise to a strong electrostatic attraction force [55].

The diffuse layer is a thicker ion layer compared with the adsorbed layer. It consists of aqueous cations and anions and extends from the outside of the adsorbed layer until where the solution concentration is homogeneous. The cations in this part of the

layer diffuse from the outside of the adsorbed layer with lower concentrations because of thermal motion. Therefore, as the distance between cations and particles becomes larger, the electrostatic force decreases. The cation distribution in the diffuse layer is heterogeneous and increasing when close to the diffusion layer. According to the type of clay and its concentration, the thickness of the diffuse layer can be in the range from 10 to 100 Å [55].

A slipping plane is located between adsorbed and diffuse layers (Figure 2-19). Cations of the adsorbed layer move together with clay particles whereas cations in the diffuse layer exhibit hysteresis. This hysteresis happens because when clay particles move; the cation movement lags behind that of clay when it realises the change of electric balance and this results in the formation of a slipping plane [55].

There is a potential difference between a clay particle surface and the place where the concentration of ions in aqueous solution is homogeneous, which is called thermal potential. It depends on the number of negative charges on the clay particles. The higher thermal potential the negative charges of clay particles have, the more cations can be adsorbed by clay particle [55].

A potential difference exists between the slipping plane and place where the concentration of ion is homogeneous, this potential is named Zeta potential. This potential depends on the negative charge of clay particles and the positive charge of adsorbed cationic layers. The higher Zeta potential indicates more adsorbed cations of the diffuse layer which results in a thicker diffuse layer [55].

The type of cation determines the electrovalence and hydration ability of cations. When clay particles adsorb cations, these cations neutralize the negative charges of the clay surface. The negative charge of clay is constant, so when the cations have higher charge, fewer cations are needed. Then the Zeta potential and the cation number in the diffuse layer decreases; a lower number of cations and a thinner hydration film of clay surface results in a clay system that is easier to congeal. If the cations adsorbed by clay particles have low electrovalence (Na^+), the Zeta potential and the cation number in the diffuse layer increases, the hydration film of the clay surface becomes thicker and clay particles are difficult to congeal [56].

Cations (for example Na^+) have high hydration ability and the hydration film is thick which can produce a stable slurry, but there is an ideal range of the Na^+ . If Na^+ concentration is too high, it will also make the slurry congeal instead of dispersing. There are two reasons for this: (1) high concentration gives cations more opportunity to squeeze into the adsorbed layer, resulting in decrease of Zeta potential, a thinner diffuse layers and hydration films. The well-dispersed system turns to congeal; (2) higher cation concentration or a large number of cations gives a weaker hydration ability. Meanwhile the cation hydration process can take water molecules away from the clay, therefore hydration films near clay particles become thinner and a well-dispersed system turns to congeal [56].

Cations which are adsorbed on clay surfaces can hydrate and so hydration films form at clay particle surfaces. The higher Zeta potential the system has, the thicker are the diffuse layers and hydration films. This allows a higher repulsion force between clay particles, and the system has better dispersibility. Therefore, when clay particle surfaces carry the same amount of charge, hydration dispersibility of the clay in a suspending liquid depends on the Zeta potential [56].

In acid and neutral clay suspension liquids, OH^- of the Al-OH bond, O^{2-} of the Si-O bond on clay platelet edges leave the bonds because of ionization or bond breaking. As a result, clay particle edges present positive charges to form a diffuse electric double layer with positive charge. Compared with the negative charges of the clay surface, the positive charges at edges are much less and as a result, clay particles present net negative charge [56].

The properties of clays that result from the charges on clay particle surfaces depend on the pH value of the whole solution. When the pH value increases, the edges can change and present negative charge instead of positive. When the pH value reduces, the negative charges on clay particle surfaces (faces) can change to be positive. Therefore in order to ensure that clay particles bring stable negative charges to form stable negative charged diffuse electric double layer, the suspension liquid must be alkaline. The pH value is generally 8.0-9.0, sometimes this value can reach 9-10 [56].

2.4 Structure of clays and graphene oxide

2.4.1 Structure of montmorillonite

Montmorillonite is one of the smectite family and known as an ion-exchangeable clay which is generally made up of aluminosilicate layers. The formula of it can be written as $(\text{Na,Ca})_{0.33}(\text{Al,Mg})_2(\text{Si}_4\text{O}_{10})(\text{OH})_2 \cdot n\text{H}_2\text{O}$ [57].

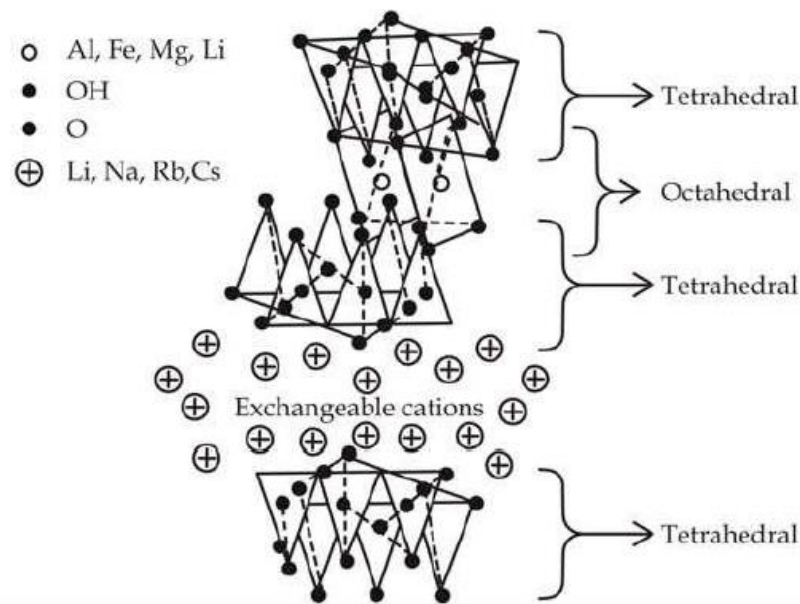


Figure 2-20. Structure of MMT. [57]

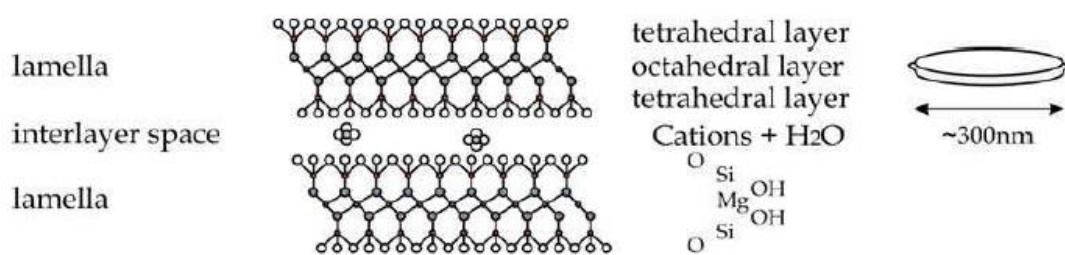


Figure 2-21. Details of particle view of MMT. [57]

The layered structure, shown in Figure 2-20, presents one octahedral sheet of alumina (aluminosilicate) or magnesium silicate sandwiched by two silica tetrahedrons [57]. ‘Each layer has small net negative charge because of an isomorphous substitution of ions in the framework’, shown in Figure 2-21 [57]. A small portion of the metal cations in the central octahedral layer is replaced by

cations of lower valence but similar size. This produces an electrical charge imbalance that is corrected by the presence of cations held outside and between each of the sheets. The cations located at interlayer positions are named as exchangeable cations. Montmorillonite can contain different species in the rooms of interlayer to provide intercalation type composite [57].

2.4.2 Structure of laponite

Laponite is also known as ‘hydrous sodium lithium magnesium silicate’ [58]. It is an artificial layered clay with similar crystal structure and composition to MMT. The composition of it are indicated as SiO₂, 65.82 %; MgO, 30.15 %; Na₂O, 3.20 %; LiO₂, 0.83 %, reported by Levitz et al. [58].

The density of laponite is given as 2530 kg·m⁻³. It is reported that laponite single crystals are layered discs with the size of 25 nm in diameter and 0.92 nm in thickness [59]. The laponite discs are arranged into stacks and sharing interlayer cations like Na⁺ ions.

2.4.3 Structure of kaolinite

Kaolinite is a hydrated aluminum disilicate mineral formed by natural hydrothermal decomposition that commonly exists in soils or sedimentary rocks. Kaolinite has a general composition as Al₂Si₂O₅(OH)₄. Unlike MMT, it has a 1:1 dioctahedral phyllosilicate structure which means kaolinite has structurally asymmetric layers. The aluminium atoms bonded with apical oxygen atoms and inner hydroxyl in one octahedron while the other layer side is composed of a silicate layer structure with silicon atoms connected tetrahedrally to oxygen atoms [60]. The structure of kaolinite is shown in Figure 2-22 [61]. In addition to abundant mineral availability, kaolinite also has advantages of high crystallinity and purity. However, a limited amount of research on intercalated kaolinite/polymers composite has been reported [61]. The reason might lie in the hydrogen-bonding between the layers that makes the interaction between interfaces of kaolinite and polymers quite different from other smectite clay/polymer. Additionally, kaolinite was reported with a poor swell

as well as a low cation-exchange capacity (1-15 meq/100g) compared with other mineral clays such as MMT (80-150 meq/100 g) [60, 62-65].

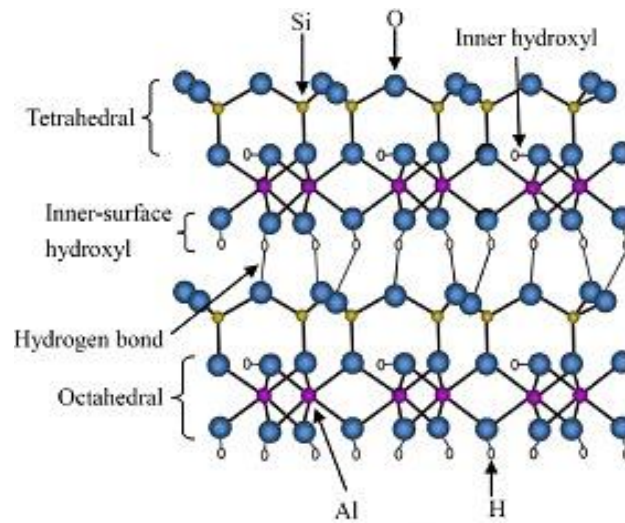


Figure 2-22. Structural diagram of kaolinite showing two 1:1 layers joined together by hydrogen bonding. [61]

2.4.4 Structure of graphene oxide

Graphene is constituted by ‘planar monolayer of conjugated sp^2 carbon atoms bonded in six-membered rings’, the structure is shown in Figure 2-23 [66]. The thickness of single-layered graphene is less than 1 nm, which is reported as the thinnest material discovered among the world. The width of the graphene sheet is varied from 10 nm to 1 cm. Besides, graphene is the strongest material at present. Single-layered graphene was found to exhibit Young’s modulus and tensile strength of 1100 GPa and 130 GPa, respectively [67].

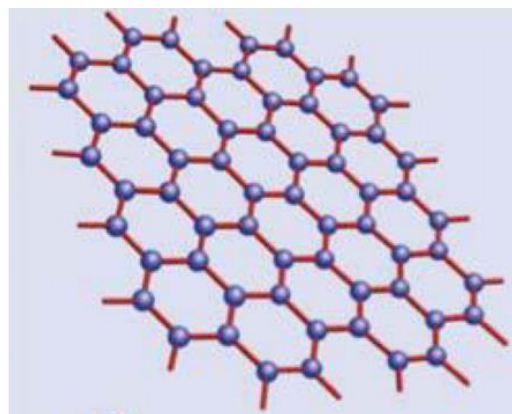


Figure 2-23. Schematic showing structure of graphene. [66]

The main structure of graphene oxide is the same as the structure of graphene but with functional groups, such as OH and COOH. The structure of graphene oxide is shown in Figure 2-24 [68]. With these functional groups, the graphene oxide is much easier to react with chemicals as compared with graphene, and GO can form bonds between its functional groups (-OH or -COOH) with some polymers [68].

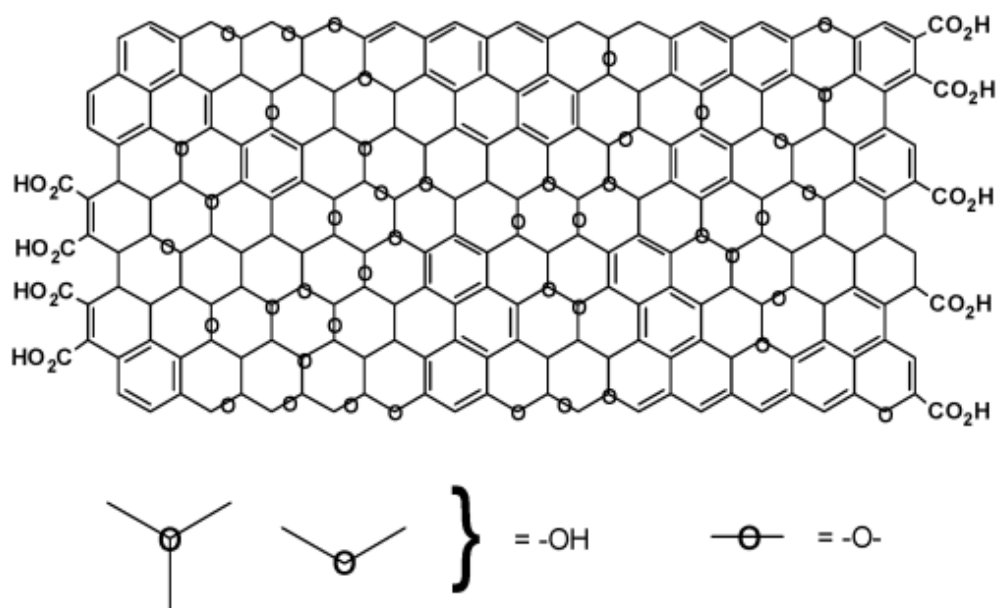


Figure 2-24. The structure of graphene oxide. [68]

References

- [1] Hull D, Clyne TW. An introduction to composite materials. Cambridge University press; 1996 Aug 13.
- [2] Agarwal BD, Broutman LJ, Chandrashekhara K. Analysis and performance of fiber composites. John Wiley & Sons; 2006 Jul 11.
- [3] Pinnavaia TJ, Beall GW, editors. Polymer-clay nanocomposites. John Wiley; 2000.
- [4] Heinemann F, Launspach M, Gries K, Fritz M. Gastropod nacre: structure, properties and growth—biological, chemical and physical basics. Biophysical chemistry. 2011 Jan 31;153(2):126-53.
- [5] Wada K. Crystal growth of molluscan shells. Japan: Bulletin of the National Pearl Research Laboratories; 1961.
- [6] Erben HK. On the structure and growth of the nacreous tablets in gastropods. Biomineralization. 1974;7:14-27.
- [7] Nakahara H. An electron microscope study of the growing surface of nacre in two gastropod species, *Turbo cornutus* and *Tegula pfeifferi*. Venus. 1979.
- [8] Bevelander G. Abalone: gross and fine structure. Boxwood Press; 1988.
- [9] Menig R, Meyers MH, Meyers MA, Vecchio KS. Quasi-static and dynamic mechanical response of *Haliotis rufescens* (abalone) shells. Acta Materialia. 2000 May 29;48(9):2383-98.
- [10] Lin A, Meyers MA. Growth and structure in abalone shell. Materials Science and Engineering: A. 2005 Jan 15;390(1):27-41.
- [11] Meyers MA, Lin AY, Chen PY, Muyco J. Mechanical strength of abalone nacre: role of the soft organic layer. Journal of the Mechanical Behavior of Biomedical Materials. 2008 Jan 31;1(1):76-85.
- [12] Su X, Belcher AM, Zaremba CM, Morse DE, Stucky GD, Heuer AH. Structural and microstructural characterization of the growth lines and prismatic microarchitecture in red abalone shell and the microstructures of abalone “flat pearls”. Chemistry of Materials. 2002 Jul 15;14(7):3106-17.
- [13] Snow MR, Pring A, Self P, Losic D. The origin of the color of pearls in iridescence from nano-composite structures of the nacre. American Mineralogist. 2004 Oct 1;89(10):1353-8.
- [14] Meyers MA, Chen PY, Lin AY, Seki Y. Biological materials: structure and

mechanical properties. *Progress in Materials Science*. 2008 Jan 31;53(1):1-206.

[15] Yao HB, Ge J, Mao LB, Yan YX, Yu SH. 25th anniversary article: artificial carbonate nanocrystals and layered structural nanocomposites inspired by nacre: synthesis, fabrication and applications. *Advanced Materials*. 2014 Jan 1;26(1):163-88.

[16] Wegst UG, Ashby MF. The mechanical efficiency of natural materials. *Philosophical Magazine*. 2004 Jul 21;84(21):2167-86.

[17] Barthelat F. Nacre from mollusk shells: a model for high-performance structural materials. *Bioinspiration & Biomimetics*. 2010 Aug 20;5(3):035001.

[18] Meyers MA, Chen PY, Lin AY, Seki Y. Biological materials: structure and mechanical properties. *Progress in Materials Science*. 2008 Jan 31;53(1):1-206.

[19] Currey JD, Taylor JD. The mechanical behaviour of some molluscan hard tissues. *Journal of Zoology*. 1974 Jul 1;173(3):395-406.

[20] Checa AG, Cartwright JH, Willinger MG. The key role of the surface membrane in why gastropod nacre grows in towers. *Proceedings of the National Academy of Sciences*. 2009 Jan 6;106(1):38-43.

[21] Sarikaya M, Aksay IA. *AIP Series in Polymers & Complex Materials*. New York: AIP Press Woodbury;1995.

[22] Li X, Chang WC, Chao YJ, Wang R, Chang M. Nanoscale structural and mechanical characterization of a natural nanocomposite material: the shell of red abalone. *Nano Letters*. 2004 Apr 14;4(4):613-7.

[23] Rousseau M, Lopez E, Stempflé P, Brendlé M, Franke L, Guette A, Naslain R, Bourrat X. Multiscale structure of sheet nacre. *Biomaterials*. 2005 Nov 30;26(31):6254-62.

[24] Fritz M, Belcher AM, Radmacher M, Walters DA, Hansma PK, Stucky GD, Morse DE, Mann S. Flat pearls from biofabrication of organized composites on inorganic substrates. *Nature*. 1994 Sep 1;371(6492):49-51.

[25] Checa AG, Cartwright JH, Willinger MG. Mineral bridges in nacre. *Journal of Structural Biology*. 2011 Dec 31;176(3):330-339.

[26] Song F, Soh AK, Bai YL. Structural and mechanical properties of the organic matrix layers of nacre. *Biomaterials*. 2003 Sep 30;24(20):3623-31.

[27] Sellinger A, Weiss PM, Nguyen A, Lu Y, Assink RA, Gong W, Brinker CJ. Continuous self-assembly of organic-inorganic nanocomposite coatings that mimic nacre. *Nature*. 1998 Jul 16;394(6690):256-60.

-
- [28] Tang Z, Kotov NA, Magonov S, Ozturk B. Nanostructured artificial nacre. *Nature Materials*. 2003 Jun 1;2(6):413-8.
- [29] Podsiadlo P, Kaushik AK, Arruda EM, Waas AM, Shim BS, Xu J, Nandivada H, Pumphlin BG, Lahann J, Ramamoorthy A, Kotov NA. Ultrastrong and stiff layered polymer nanocomposites. *Science*. 2007 Oct 5;318(5847):80-3.
- [30] Podsiadlo P, Michel M, Lee J, Verploegen E, Wong Shi Kam N, Ball V, Lee J, Qi Y, Hart AJ, Hammond PT, Kotov NA. Exponential growth of LBL films with incorporated inorganic sheets. *Nano Letters*. 2008 May 17;8(6):1762-70.
- [31] Podsiadlo P, Tang Z, Shim BS, Kotov NA. Counterintuitive effect of molecular strength and role of molecular rigidity on mechanical properties of layer-by-layer assembled nanocomposites. *Nano Letters*. 2007 May 9;7(5):1224-31.
- [32] Bennadji-Gridi F, Smith A, Bonnet JP. Montmorillonite based artificial nacre prepared via a drying process. *Materials Science and Engineering: B*. 2006 Jun 15;130(1):132-6.
- [33] Zhang X, Liu C, Wu W, Wang J. Evaporation-induced self-assembly of organic-inorganic ordered nanocomposite thin films that mimic nacre. *Materials Letters*. 2006 Aug 31;60(17):2086-9.
- [34] Munch E, Launey ME, Alsem DH, Saiz E, Tomsia AP, Ritchie RO. Tough, bio-inspired hybrid materials. *Science*. 2008 Dec 5;322(5907):1516-20.
- [35] Deville S, Saiz E, Nalla RK, Tomsia AP. Freezing as a path to build complex composites. *Science*. 2006 Jan 27;311(5760):515-8.
- [36] Launey ME, Munch E, Alsem DH, Barth HB, Saiz E, Tomsia AP, Ritchie RO. Designing highly toughened hybrid composites through nature-inspired hierarchical complexity. *Acta Materialia*. 2009 Jun 30;57(10):2919-32.
- [37] Munch E, Saiz E, Tomsia AP, Deville S. Architectural Control of Freeze-Cast Ceramics Through Additives and Templating. *Journal of the American Ceramic Society*. 2009 Jul 1;92(7):1534-9.
- [38] Deville S, Saiz E, Tomsia AP. Ice-templated porous alumina structures. *Acta Materialia*. 2007 Apr 30;55(6):1965-74.
- [39] Launey ME, Munch E, Alsem DH, Saiz E, Tomsia AP, Ritchie RO. A novel biomimetic approach to the design of high-performance ceramic-metal composites. *Journal of the Royal Society Interface*. 2010 May 6;7(46):741-53.
- [40] Long B, Wang CA, Lin W, Huang Y, Sun J. Polyacrylamide-clay nacre-like nanocomposites prepared by electrophoretic deposition. *Composites Science and*

Technology. 2007 Oct 31;67(13):2770-4.

- [41] Lin TH, Huang WH, Jun IK, Jiang P. Electrophoretic co-deposition of biomimetic nanoplatelet–polyelectrolyte composites. *Electrochemistry Communications*. 2009 Aug 31;11(8):1635-8.
- [42] Lin TH, Huang WH, Jun IK, Jiang P. Bioinspired assembly of surface-roughened nanoplatelets. *Journal of Colloid and Interface Science*. 2010 Apr 15;344(2):272-8.
- [43] Ekiz OO, Dericioglu AF, Kakisawa H. An efficient hybrid conventional method to fabricate nacre-like bulk nano-laminar composites. *Materials Science and Engineering: C*. 2009 Aug 1;29(6):2050-4.
- [44] Yao HB, Tan ZH, Fang HY, Yu SH. Artificial Nacre - like Bionanocomposite Films from the Self-Assembly of Chitosan-Montmorillonite Hybrid Building Blocks. *Angewandte Chemie International Edition*. 2010 Dec 27;49(52):10127-31.
- [45] Walther A, Bjurhager I, Malho JM, Pere J, Ruokolainen J, Berglund LA, Ikkala O. Large-area, lightweight and thick biomimetic composites with superior material properties via fast, economic, and green pathways. *Nano Letters*. 2010 Mar 10;10(8):2742-8.
- [46] Walther A, Bjurhager I, Malho JM, Ruokolainen J, Berglund L, Ikkala O. Supramolecular Control of Stiffness and Strength in Lightweight High-Performance Nacre - Mimetic Paper with Fire-Shielding Properties. *Angewandte Chemie International Edition*. 2010 Aug 23;49(36):6448-53.
- [47] Li XQ, Zeng HC. Calcium carbonate nanotablets: bridging artificial to natural nacre. *Advanced Materials*. 2012 Dec 11;24(47):6277-82.
- [48] Walley P, Zhang Y, Evans JR. Self-assembly of montmorillonite platelets during drying. *Bioinspiration & Biomimetics*. 2012 Jul 27;7(4):046004.
- [49] The zeta potential. *colloidal Dynamics*. Electroacoustics tutorials. [Accessed 06 September 2016]; Available from: <http://www.colloidal-dynamics.com/docs/CDEITut1.pdf>
- [50] What is zeta potential. *Filtration & separations society*. [Accessed 06 September 2016]; Available from: <http://www.afssociety.org/filtration-media/62-what-is-zeta-potential>
- [51] What is zeta potential. *Brookhaven instruments corporation*. [Accessed 06 September 2016]; Available from: <http://www.brookhaveninstruments.com/what-is->

zeta-potential

- [52] Zeta potential analysis of nanoparticles. Nano composix. [Accessed 06 September 2016]; Available from: <http://50.87.149.212/sites/default/files/nanoComposix%20Guidelines%20for%20Zeta%20Potential%20Analysis%20of%20Nanoparticles.pdf>
- [53] Zeta potential definition. About education. [Accessed 06 September 2016]; Available from: <http://chemistry.about.com/od/chemistryglossary/g/Zeta-Potential-Definition.htm>
- [54] Zeta potential. Malvern. [Accessed 06 September 2016]; Available from: <http://www.malvern.com/en/products/measurement-type/zeta-potential/>
- [55] Zeta Potential: A Complete Course in 5 Minutes. [Accessed 06 September 2016]; Available from: <http://www.zeta-meter.com/5min.pdf>
- [56] Yukselen-Aksoy Y, Kaya A. A study of factors affecting on the zeta potential of kaolinite and quartz powder. *Environmental Earth Sciences*. 2011 Feb 1;62(4):697-705.
- [57] Davidovic M, Nikolic A, Jovanovic D, Kutin M, Pissis P, Linic S, Sredic S, Mioc U, Nedic Z. Nanocomposite based on natural materials. INTECH Open Access Publisher; 2011.
- [58] Levitz P, Lecolier E, Mouchid A, Delville A, Lyonnard S. Liquid-solid transition of Laponite suspensions at very low ionic strength: Long-range electrostatic stabilisation of anisotropic colloids. *EPL (Europhysics Letters)*. 2000 Mar 1;49(5):672.
- [59] Cummins HZ. Liquid, glass, gel: The phases of colloidal Laponite. *Journal of Non-Crystalline Solids*. 2007 Nov 1;353(41):3891-905.
- [60] Matusik J, Stodolak E, Bahranowski K. Synthesis of polylactide/clay composites using structurally different kaolinites and kaolinite nanotubes. *Applied Clay Science*. 2011 Jan 31;51(1):102-9.
- [61] Li X, Liu Q, Cheng H, Zhang S, Frost RL. Mechanism of kaolinite sheets curling via the intercalation and delamination process. *Journal of Colloid and Interface Science*. 2015 Apr 15;444:74-80.
- [62] Gardolinski JE, Carrera LC, Cantao MP, Wypych F. Layered polymer-kaolinite nanocomposites. *Journal of Materials Science*. 2000 Jun 1;35(12):3113-9.
- [63] Carrado KA, Xu L. In situ synthesis of polymer-clay nanocomposites from silicate gels. *Chemistry of Materials*. 1998 May 18;10(5):1440-5.

-
- [64] Alexandre M, Dubois P. Polymer-layered silicate nanocomposites: preparation, properties and uses of a new class of materials. *Materials Science and Engineering: R: Reports*. 2000 Jun 15;28(1):1-63.
- [65] Zhang J, Wang A. Study on superabsorbent composites. IX: synthesis, characterization and swelling behaviors of polyacrylamide/clay composites based on various clays. *Reactive and Functional Polymers*. 2007 Aug 31;67(8):737-45.
- [66] Zhu Y, Murali S, Cai W, Li X, Suk JW, Potts JR, Ruoff RS. Graphene and graphene oxide: synthesis, properties, and applications. *Advanced Materials*. 2010 Sep 15;22(35):3906-24.
- [67] Lee C, Wei X, Kysar JW, Hone J. Measurement of the elastic properties and intrinsic strength of monolayer graphene. *science*. 2008 Jul 18;321(5887):385-8.
- [68] Lerf A, He H, Forster M, Klinowski J. Structure of graphite oxide revisited. *The Journal of Physical Chemistry B*. 1998 Jun 4;102(23):4477-82.

Chapter 3

Experimental Details

3.1 Details of materials and their sources

The montmorillonite (MMT) used in all experiments were Nanofil 116® (Rockwood Company, Southern Clay Products Inc. USA) and BH Natural MMT (Blackhill Bentonite LLC, Wyoming, USA). The theoretical density of MMT powder is $3100 \text{ kg}\cdot\text{m}^{-3}$. Laponite used was laponite Rd® (Rockwood Company, Southern Clay Products Inc. USA). The density of laponite powder is $2530 \text{ kg}\cdot\text{m}^{-3}$ given by supplier. The theoretical density of kaolinite is $2460 \text{ kg}\cdot\text{m}^{-3}$ from Barrisurf LX kaolin (Imerys Minerals Ltd., Cornwall, UK). All of these four clay samples were received as dry powders.

Graphene oxide (GO) was synthesized following a modified Hummer's method [1]. A sample of 10 g graphite powder ($<20 \text{ }\mu\text{m}$, Sigma Aldrich, UK) was stirred with cold concentrated sulphuric acid (230 mL at $0 \text{ }^{\circ}\text{C}$) in an ice bath, followed by adding 30 g potassium permanganate slowly to make sure the temperature of the mixture was less than $20 \text{ }^{\circ}\text{C}$, then cooled to $2 \text{ }^{\circ}\text{C}$. After that, the mixture was stirred gradually at room temperature for at least 15 min. Distilled water (230 mL) was added slowly to the mixture and the temperature kept under $98 \text{ }^{\circ}\text{C}$. Before adding hydrogen peroxide (100 mL), the diluted suspension was stirred for 15 mins and further diluted with distilled water to 1.4 L. Finally, GO particles were centrifuged from the suspension and washed with distilled water until $\text{pH}=7$ and freeze-dried to remove water. The products were then added to distilled water and subjected to an ultrasonic probe (Hielscher UB200S from IKA Labortechnik, Staufen, Germany) at 0.5 duty cycle and 50 % power (120 W) for 72 hr to get a well dispersed GO suspension.

3.2 Solution-casting process of clay and GO/PVA composite

3.2.1 Self-assembled process of clay discs

The self-assembled clay discs were made as Walley reported [2]. Using MMT as an example, a suspension of 1 wt. % MMT was made in distilled water (10 g Nanofil 116 in 990 mL in 1500 mL capacity bottles). After stirring the suspension vigorously for 6 hr, the suspension was subjected to an ultrasonic probe. The suspension was

poured into polystyrene petri dishes of 86 mm diameter and left to dry under a perspex cover to prevent dust and to slow the evaporation rate at a temperature of $(23 \pm 2 \text{ }^{\circ}\text{C})$ and relative humidity $60 \pm 10 \%$. The MMT sheets were dried at an evaporation rate of $12 \text{ nm}\cdot\text{s}^{-1}$ within 864 ks to produce 100 % MMT ordered film.

3.2.2 Original process of solution casting from Walley [2]

A suspension of 1 wt. % MMT was made in distilled water (10 g Nanofil 116 in 990 g in 1500 mL capacity bottles). After stirring the suspension vigorously for 6 hrs, the suspension was subjected to ultrasonic probe for 30 min at 0.5 duty cycle and 50% power (120 W). Polyvinyl alcohol powder ($M_w=85000\text{-}124000$, 99+ % hydrolyzed, Sigma Aldrich, UK) was dissolved in water at $80 \text{ }^{\circ}\text{C}$ under magnetic stirring for a 0.6 wt. % solution.

A suspension of 0.6 wt. % laponite was made by adding 6 g laponite powder into 994 g distilled water and stirred for 605 ks (7 days) and subjected to ultrasonic for 30 min at 0.5 duty cycle and 50% power (120 W).

To prepare the clay/PVA film, the PVA solution was slowly poured into clay suspensions. Then, the clay/polymer mixture was stirred for an extra 43 ks (12 h) at room temperature for polymer adsorption by clay particles. In the end, this suspension was poured into 86 mm petri-dishes and left at room temperature for film formation. It took about 1.2 ms (14 days) to form the thin film until a constant weight of each sample. A series of clay/PVA composite films with different clay weight/volume fractions were generated. Figure 3-1 indicated the process of self-assembly.

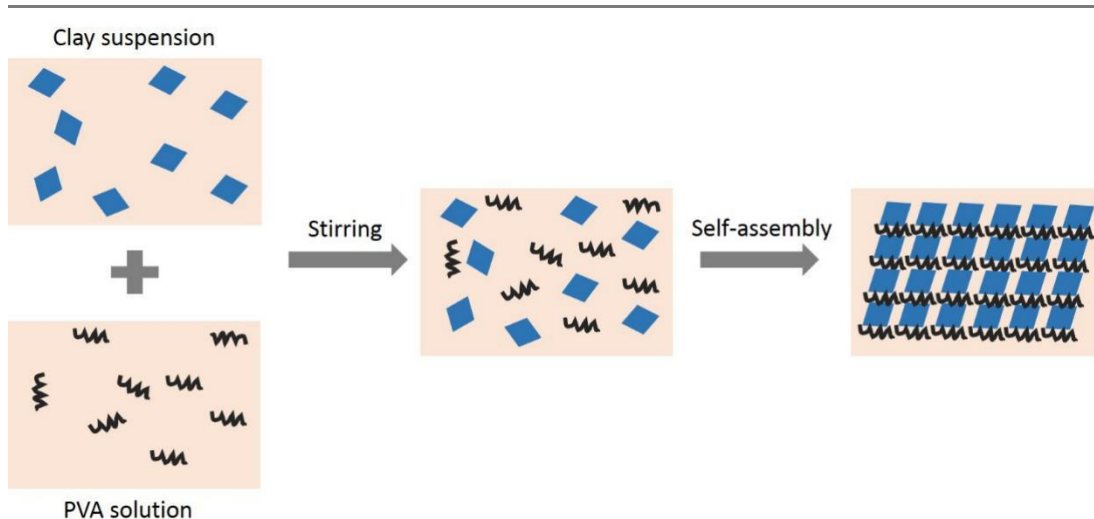


Figure 3-1. Illustration of self-assembly process.

A dispersion of 0.2 wt. % graphene oxide was made by adding 2 g graphene oxide powder into 998g distilled water and subjected to ultrasonic probe for 259 ks (72 h) at 0.5 duty cycle and 50 % power.

3.2.3 Modified process of solution casting of MMT/PVA nanocomposite

A suspension of 1 wt. % MMT was made in distilled water (10 g Nanofil 116 in 990 g in 1.5 L capacity bottles).

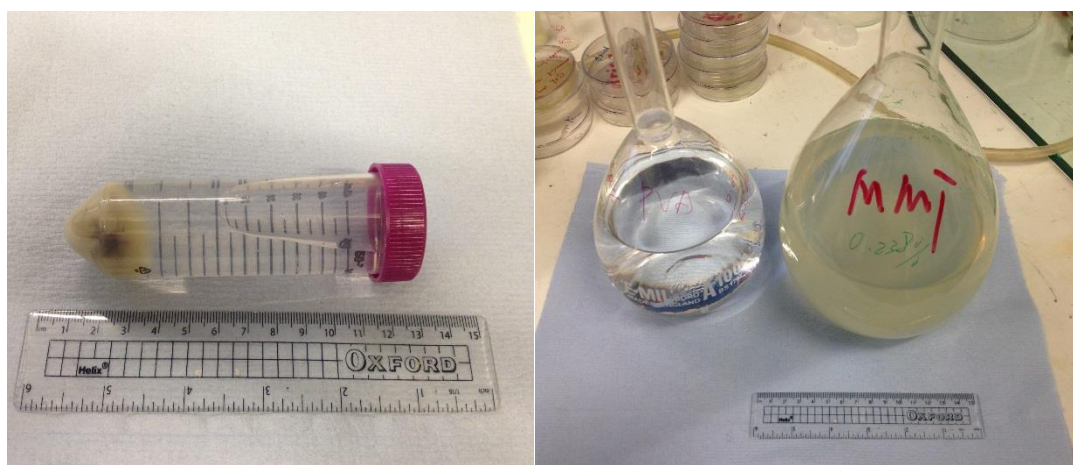


Figure 3-2. The MMT suspension after centrifugation. Left: sediment shows unexfoliated platelets and black solid impurities. Right: supernatant MMT suspension and PVA solution.

After stirring the solution vigorously for 6 hrs, the solution was subjected to an ultrasonic probe for 30 min at 0.5 duty cycle and 50 % power (120 W).

Then the suspension was introduced to a Heraeus Biofuge Primo Centrifuge machine with 6000 rpm (RCF=3340 g) for 30 min to remove unexfoliated platelets and impurities in MMT. Then the supernatant was collected and the new suspension's concentration is 0.238 wt. % (taking 50 g suspension and dried in oven, calculated by the ratio of the residual and 50 g) as shown in Figure 3-2. Then the new clay suspension was used to make the clay/PVA composites.

3.3 MMT/epoxy resin composite

Epoxy resin RX 672H/BK and RX 900D/BK with hardeners HX672H/NC and HX900D/NC were purchased from Robnor Resins Ltd. UK and used as received. P-phenylenediamine (1,4-diaminobenzene, PPD), 37 % hydrochloric acid (HCl) and 28 % ammonia solution were purchased from Sigma Aldrich Ltd. UK.

3.3.1 Mixture of clays and epoxy resins

1) 5 mL epoxy resin RX672H and 2.5 mL hardener HX672H was mixed in 2:1 volume ratio, then the mixture was stirred to form a fluid. 5.0 g Nanofil 116 was gradually added to the resin mixture, and stirred for 10 mins to make sure the MMT evenly dispersed in the mixture. After stirring, the mixture was poured into preformed moulds which were made by aluminium foil and put the moulds in a vacuum oven at 80 °C for 2 hr for resin curing. In the end, aluminium foil was peeled off then the cured disc was polished to get a flat surface for XRD.

2) Procedures 1 were repeated with BH natural clay, laponite and kaolinite instead of Nanofil 116.

3) 5 mL epoxy resin RX900D and 2.3 mL hardener HX900D was mixed in 100:46 volume ratio and stirred for a homogeneous fluid.

4) Epoxy resin RX900D and hardener HX900D were taken place of RX672H and HX672H in 1 and 2 with curing time 4 hr at 80 °C in the vacuum oven.

3.3.2 Self-assembled clay discs

The process to make self-assembled clay discs was the same process as used in section 3.2.1. An extra centrifugation for 30 min at 6000 rpm was applied for BH natural MMT to remove impurities of the suspension.

3.3.3 Ion-exchanged MMT

PPD was one of modifiers for MMT and this ion-exchange process was undertaken based on an existing method [3, 4].

Nanofil 116 MMT (5 g) was gradually added into 200 mL of distilled water and placed on a magnetic stirrer at 1000 rpm stirring for 1 hr at room temperature. 0.65 g (6 mmol) of PPD and 0.5 g of HCl were mixed in a beaker and stirred for at least 15 min. Then the PPD mixture was gradually poured into the clay suspension and stirred for another 12 hr followed by centrifugation at 6000 rpm for 15 min. The ion-exchanged suspension was washed with acetone several times. Finally, the suspension was poured into a 86 mm petri-dish and dried in the a vacuum oven at 60 °C.

3.3.4 Vacuum impregnation

A vacuum impregnation method was used to increase the probability of intercalating epoxy resins into clays. The vacuum condition may pump out the gas in MMT structure and when the vacuum environment is released, the pressure from outside may also enhance the chance for penetration of epoxy resins into clays.

Epoxy resin RX672H and HX672H were mixed in a mass ratio of 2.4:1. A preformed MMT sheet was placed in a glass petri dish. The petri dish was then

placed inside a vacuum desiccator. The desiccator was sealed with a high-vacuum silicone grease (Sigma Aldrich Ltd. UK) and pumped for 300 s. The RX672H and its hardener was added gradually from a dropping funnel (Figure 3-3) onto the surface of clay by adjusting the valve on top of the desiccator. The vacuum was held for a further 5 min, and the vacuum atmosphere released.

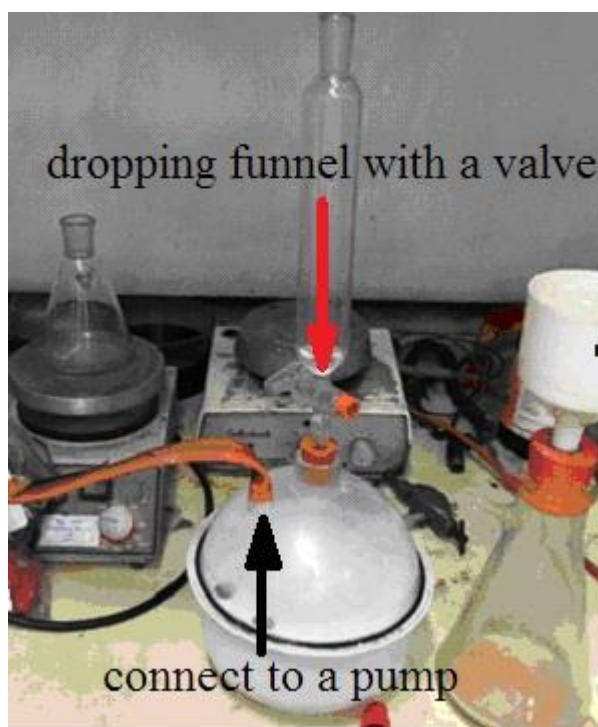


Figure 3-3. Schematic of vacuum impregnation system.

The same process was repeated using another epoxy resin RX900D and PPD modified MMT discs.

The resin-clay discs were treated by three different systems before curing: 1) the discs were left at room temperature. 2) The discs were placed into a refrigerator and kept for 72 hr then allowed to cure under room temperature. 3) The discs were placed into a refrigerator and kept for 120 hr then allowed to cure under room temperature.

The comparison experiment was set to prove the influence of time on resin curing. Even though the two kinds of resin have a long curing time compared with industrial resin, it could also cure at room temperature and inhibit the intercalation of the resin

because curing increases the resin viscosity.

3.4 Polymerisation of methyl methacrylate (MMA) and MMA/clay composites

Benzoyl peroxide (75 % BPO and 25 % water) and methyl methacrylate 99 % stabilized (MMA) were purchased from Sigma Aldrich Ltd.UK and used without any treatment.

1 wt. % and 4 wt. % BPO/MMA mixtures were made by adding 0.4 g BPO into 29.7 g MMA and 0.8 g BPO into 19.4 g MMA. The mixtures were prepared in all experiment with 0.5:1, 1:1 and 1:1.5 weight ratio with MMT, laponite, alumina and kaolinite, respectively.

Heat polymerisation was undertaken on a hot plate in a sealed aluminium reactor. The holder was designed with gas entry and exit as well as a drilled hole to accommodate a thermocouple (Figure 3-4). Before heating to the polymerisation temperature (80 °C), nitrogen is passed through a silicon pipe and through the holder for 1 min to replace air in the whole system.

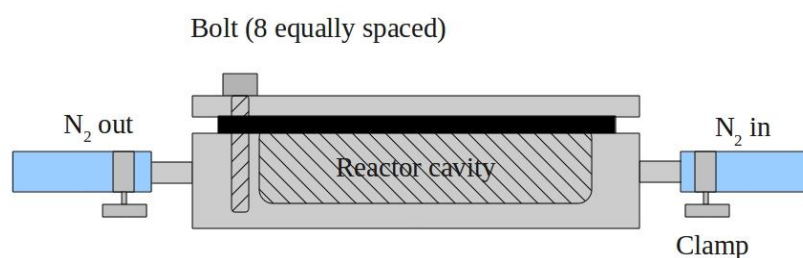


Figure 3-4. (a) Schematic of the reactor used for polymerisations.

A rubber 'O' ring was used to seal the reactor, shown in Figure 3-4 (b). After several cycles of polymerisation, the 'O' ring was replaced with a new one as it swells. The clamps were closed and a balloon was set at the nitrogen outside to keep a nitrogen atmosphere after the 1 min nitrogen flow.

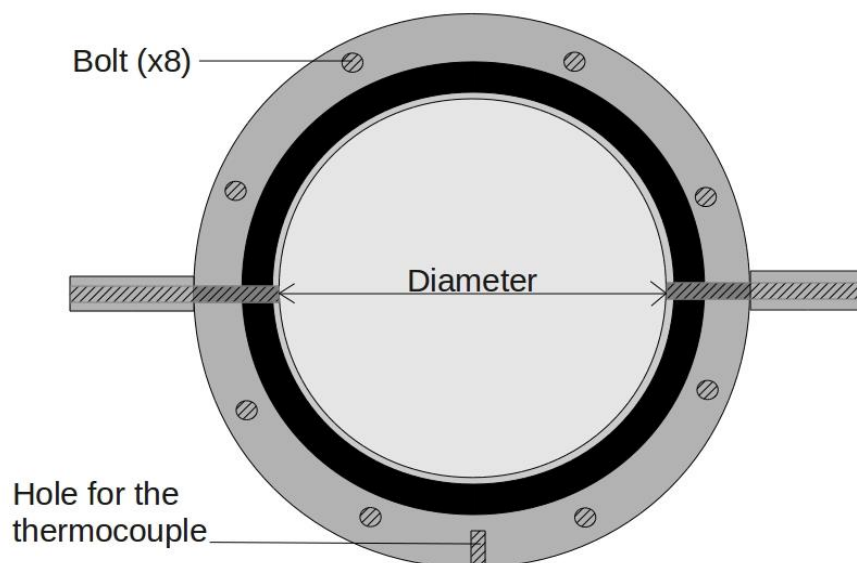


Figure 3-4. (b) Plan of the reactor used for polymerisations. Inner diameter is 96.5 mm. Bolts are 4 mm (M4) in diameter.

3.5 Photo polymerisation of laponite/polymer composite

The monomers used in this part were tri (ethyleneglycol) dimethacrylate (TEGDMA) (Sigma-Aldrich Ltd. UK) and poly (propylene glycol) dimethacrylate (PPGDMA) (Sigma Aldrich Ltd. UK). The average molecular weight of TEGDMA is $286.32 \text{ g}\cdot\text{mol}^{-1}$ and PPGDMA is $560 \text{ g}\cdot\text{mol}^{-1}$. Camphorquinone (Sigma Aldrich Ltd. UK) was used as photoinitiator the amine accelerator used was N,N-dimethyl-p-toluidine (DMPT) (Merck Chemicals, UK). All chemicals were used without any further treatment.

The monomer solution was made up of 98 wt. % monomer (both TEGDMA and PPGDMA), 1 wt. % camphorquinone and 1 wt. % DMPT. The mixture was then introduced to a magnetic stirrer in 200 rpm for 5 mins to make sure the photoinitiator dispersed well. The solution was placed in a brown glass bottle and kept in a refrigerator.

3.5.1 Infiltration of monomer in self-assembled structure

Due to the sensitive property of the monomer, experiments were carried out in a dark area within a short time. Camphorquinone can initiate the polymerisation under blue light of the wavelength 465 nm. However, sunlight can be also trigger the reaction in a longer time range. The procedures below show the steps about how the experiment was carried out.

A preformed clay sheet was put in a glass petri dish and immersed in monomer solution (98:1:1 solution) for 24 hr, as a comparison another clay was immersed for 72 hr. The glass petri dishes were left in a dark place and covered with aluminium foil to avoid evaporation before polymerisation. Polymerisation will be indicated in section 3.5.2.

A comparison experiment was set up with a vacuum impregnation method. The clay disc was placed in a vacuum desiccator and pumped for 10 min. The monomer solution was gradually added from a dropping funnel onto the clay surface. The system was kept under vacuum conditions for 60 s and then the vacuum was released. The disc was then polymerised.

Experiments with the monomer solution (both TEGDMA and PPGDMA) were conducted in a vacuum desiccator but the clay discs were kept under vacuum conditions for different ranging from 540 s to 68.82 ks. (540 s, 960 s, 1680 s, 3006 s, 21.6 ks, and 68.82 ks). Then the discs were polymerised.

3.5.2 Polymerisation of clay discs

Oxygen in the atmosphere acts as an inhibitor of the photo polymerisation reactions. Therefore, the monomers were polymerised in an oxygen free atmosphere. A device was set to polymerise the discs as seen in Figures 3-5 (a) and (b). The device was made up of poly (methyl methacrylate) and was designed with gas entry and exit in order to let nitrogen go through all the system. It was sealed by a neoprene rubber 'O' ring.

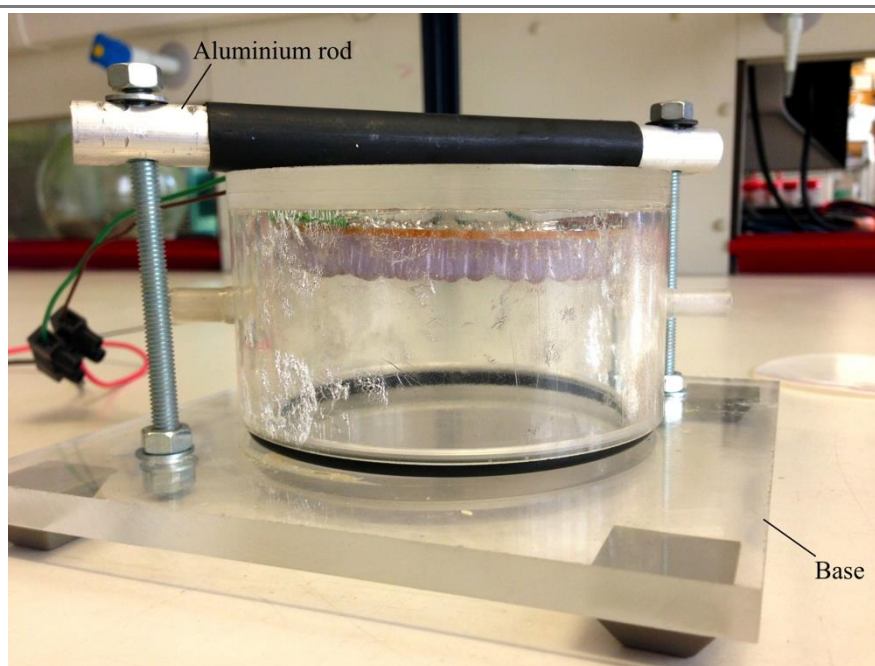


Figure 3-5. (a) A front view of photo polymerisation device.

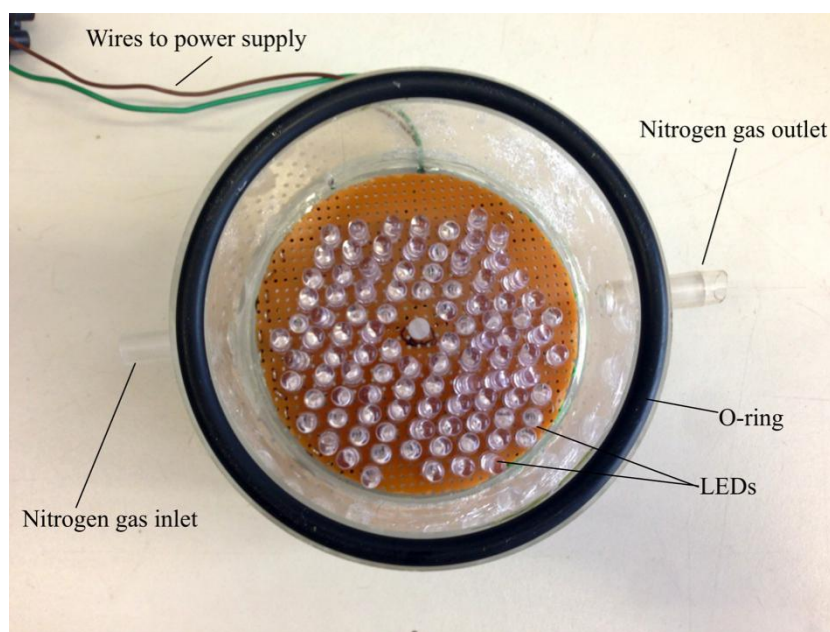


Figure 3-5. (b) A top view of photo polymerisation device.

The photoinitiator, camphorquinone is reported to have the highest absorption peak under blue light with a wavelength of 465 nm [5]. The polymerisation device was embedded a group of light emitting diodes (LEDs) on a circuit board so that it can emit light for photo polymerisation.

The monomer/clay disc was located on a piece of polytetrafluoroethylene (PTFE)

sheet, followed by sealing the whole system. A nitrogen gas flow introduced for 300 s to remove oxygen inside the device. The LEDs were turned on in a darkroom for polymerisation.

3.6 Study of kaolinite and kaolinite composite

This part of work was cooperated with two Masters students, Hao Su and Kate Sanders who were under my supervision and advice.

3.6.1 Kaolinite sedimentation process

A 1 vol. % kaolinite suspension was made by adding 24.6 g kaolinite into 990 mL water in a 1500 mL glass beaker and then introduced to a magnetic stirrer at 1000 rpm at room temperature for 10 min. After stirring, the suspension was treated by an ultrasonic probe for 30 min at 0.5 duty and 50 % power. This experiment was set up to modify determine pH value which optimizes kaolinite particle dispersion. Then, the suspension was chosen to make a batch of 10 mL samples in which the pH value is varied from 1-10 (adjusted by HCl or ammonium hydroxide). This batch was then put on the bench as shown in Figure 3-6. The sedimentation height was recorded as a function of time.

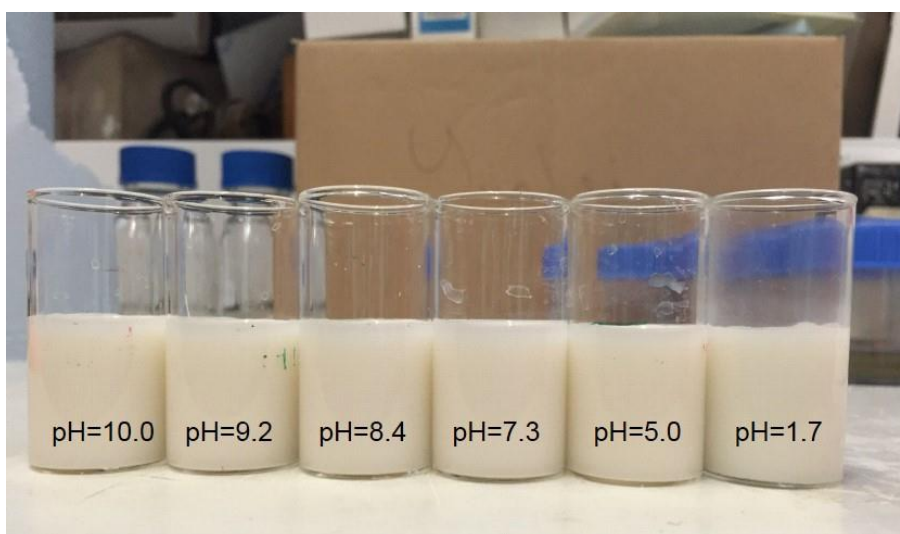


Figure 3-6. Kaolinite suspensions at different pH values.

3.6.2 Kaolinite epoxy resin system

This part of work took two main steps 1) A preformed kaolinite sheet was made either by the self- assembly process as in section 3.2.1 or vacuum assisted filtration method. 2) Epoxy resin was penetrated into clay by vacuum impregnation (section 3.3.4) and self -infiltration at ambient conditions.

Vacuum filtration: this method was used to scale up the kaolinite sheet. Compared with MMT or laponite, kaolinite itself has larger plates and based on the previous experiment, it is less possible for the epoxy resin to get into the interlayers of MMT due to the long carbon chain of resin which gives resin a high viscosity. However, epoxy resin is a structurally strong polymer so that it is worth making large plates of kaolinite-resin composite. The filtration plates were prepared by a hierarchy filter system. The filter system was layered by two pieces of Whatman grade 1 filter paper (pore size 11 μm) and two pieces of Whatman grade 2 filter paper (pore size 8 μm), followed by a layer of nitrocellulose membrane (pore size 5 μm). These layers were designed in sequence and moistened with distilled water before use to make sure no trapped air or folds were present which could cause an irregular surface of the kaolinite filter cake. A frame with size 200 ± 0.25 mm in length and 150 ± 0.25 mm in width was set at the top of the filter system and clamped tight to hold the kaolinite suspension during filtration.

Self-infiltration method: a desired mixture of resin and its hardener was dropped at both top side and bottom side of kaolinite filter cake to identify the influence by the size of kaolinite. Generally, the size of kaolinite plates was smaller on the top compared with that at the bottom. The kaolinite sheets were left at ambient conditions until the mixture fully cured.

3.6.3 Kaolinite/MMA composite

MMA was washed twice by a 10 % sodium hydroxide solution, followed by washing with distilled water until the pH=7. The inhibitor was removed by the previous step and then MMA was filtered and stored in a refrigerator.

N,N-dimethyl-p-toluidine (DMPT) was purchased from Sigma Aldrich Ltd. UK without any further purification with a $M_w=135.21 \text{ g}\cdot\text{mole}^{-1}$.

3.6.3.1 Redox polymerisation of MMA

MMA was mixed with BPO at the desired concentration, and the mixture was added to DMPT. The DMPT:BPO molar ratio should be 1:1. The pre-polymerisation mixture was stirred for 30 s before being polymerised at room temperature. The polymerisation was checked every 300 s. An even mixing of the MMA/BPO solution with DMPT leads in a viscous orange liquid as a semi-polymerised state.

Experiments with MMA and BPO: 1, 1.5, 2 and 4 wt. % concentration BPO was added to the unstabilised MMA, in the meanwhile, a 1:1 molar ratio of DMPT:BPO was mixed with BPO-MMA. Considering the 75 % purity benzoyl peroxide (molecule weight is $242.23 \text{ g}\cdot\text{mole}^{-1}$), the mass ratio should be 1:2.389. MMA from which the inhibitor had been removed was then mixed with 2 and 4 wt. % BPO as well as the same molar ratio of DMPT.

3.6.3.2 Redox polymerisation of kaolinite and MMA

Redox polymerisations were conducted with both raw kaolinite powder, and filter cake of kaolinite under nitrogen. The MMA/BPO/DMPT mixture was prepared as detailed in section 3.6.3.1. When the mixture was added into the kaolinite powder, it polymerised immediately while in terms of the filter cake, the mixture was left for 300 s at room temperature before added in the kaolinite filter.

3.7 Characterisation of instruments and their operation

3.7.1 Fourier transform infrared spectroscopy (FTIR)

FTIR spectra were obtained with an ALPHA Bruker Optics FTIR spectrophotometer equipped with ZnSe ATR crystal. The samples were scanned from $400\text{-}4000 \text{ cm}^{-1}$ wavenumber with a 32 scan for each sample.

3.7.2 X-Ray diffraction (XRD)

For the purpose of measurement of basal plane spacing of clays and other plate-like reinforcements, XRD data were collected using a Siemens D500 X-Ray diffractometer using Cu $K\alpha_1$ radiation with a wavelength of 0.154056 nm. The diffractometer was operated at 40 kV and 30 mA. Scans began at a low angle of 2° and scanned to 24° of 2 θ in 0.05° steps at 4 s per step.

For characterisation of the orientation function of the clay/polymer composite, XRD Bruker D-8 discover was used. The angle θ was set at the peak corresponding to d_{002} of the MMT mineral or its composite generally giving 2 θ at ~7.5° and kept constant. The angle ψ was initially set at -10° and was rotated to 80° in 5° /steps. A recording was made on the detector at each step of ψ . A trace of intensity as a function of θ at each ψ step was then plotted. The scan was measured under DA VINCI solution with a VANTEC 500 detector with a voltage of 50 kV and current of 1 mA. The baseline was constructed and the peak area was integrated using Bruker software. Details of the method of obtaining an orientation function from this data set are described in Section 4.3.3.

3.7.3 Measurement of mechanical properties

Tensile testing of the polymer and its nanocomposites was performed using a Hounsfield H10KM/0348 testing machine, presently maintained by Tinius Olsen (Salford Redhill, Surrey, UK). In general a 100 N load cell was used with a crosshead speed of 5 mm per min. The calibration of the machine was done using dead weight and the deviation between recorded and actual force was 0.4 % upon which a calibration factor was based. Gauge length was measured using a Vernier caliper and was generally set at 70 mm. The tensile stress and strain were calculated as follows,

$$\text{Tensile stress: } \sigma = \frac{F}{A} \quad (3-1)$$

$$\text{Tensile strain: } \varepsilon = \frac{\Delta L}{L_0} \quad (3-2)$$

In some cases, the Young's modulus, E , was estimated from the slope of stress-strain curve at the origin designated, a tangent modulus for the various polymers as follows.

$$\text{Young's modulus: } E = \frac{\sigma}{\varepsilon} = \frac{F \cdot L_0}{A \cdot \Delta L} \quad (3-3)$$

3.7.4 Differential scanning calorimetry (DSC)

The thermal behaviour of the films was investigated by differential scanning calorimetry (DSC) using a DSC 822 (Mettler Toledo) instrument at a heating rate of 5 °C per min under N₂ from 25 °C to 300 °C.

3.7.5 Scanning electron microscopy (SEM)

The SEM, JEOL JSM-6700F Field Emission Scanning Electron Microscope (FESEM), was used to observe the cross-sections of the ordered structures under 10 kV and 10 µA with the pressure no higher than 3×10^{-4} Pa. The samples were placed in vacuum to remove adsorbed water or solvents from the surface. The samples were coated with Au/Pt for 45 s in argon atmosphere to increase their electrical conductivity.

3.7.6 Energy dispersive X-ray spectroscopy (EDS)

An EDS was used to detect the elemental composition of the samples as well as elemental distribution. This device was combined with SEM 6700F with a working distance between 8-15 mm. The data was analysis by INCA system.

Another EDS used in this project was an independent Energy dispersive X-ray fluorescence spectrometer. This EDS 7000 (Shimadzu, Japan) was operated to detect the elements in the bulk material under 50 KV and 100 µA in helium atmosphere. Each scan was taken 60 s and each sample has 2 scans. The report can be created with oxygen elements in and out.

3.7.7 Thermogravimetric analysis (TGA)

Thermal analysis of the polymers and nanocomposites were conducted on Q500 thermal analyser. Samples (~10-20 mg) were heated using an aluminium pan at a constant rate of $10^{\circ}\text{C}\cdot\text{min}^{-1}$ under N_2 at a flow rate of $40\text{-}60\text{ mL}\cdot\text{min}^{-1}$ between 25°C and 800°C .

3.7.8 Atomic force microscopy (AFM)

Surface morphology was analysed under AFM multimode-8 Bruker. The centrifuged MMT suspension was diluted to 10^{-3} wt. % and dropped to a new mica disc and dried at room temperature. For AFM imaging, the mode was set as peak force mode with frequency 2 kHz, the chips point set as $x=0$, $y=0$, $z=1\text{-}2$ micro meter and was moved slowly to contact the sample under a voltage of 0.03 V. The data was analysed with software Nanoscope 1.7.

3.7.9 UV-VIS spectrometer

A UV-Visible (Lambda 950, Perking Elmer) was used to determine the transparency of the samples. Before readings were taken, a background scan was performed. The transmission spectra of each disc was recorded in the range between 800 and 400 nm.

3.7.10 Laser cutter

Laser cutter (Universal 3000, USA) was used to cut the sample into small strips with the dimension 10 mm width and 50 mm long under 10 % power under 100 speed, 1000 PPI and 0.30 Z Axi.

3.7.11 Ultrasonic probe

Ultrasonic vibrations were used to assist in the dispersion of the monomer and

polymer into the clay galleries. Ultrasonic homogenizer sonicator model U200S-Control from IKA Labortechnik Staufen, Germany was used at duty cycle 0.5 with constant amplitude of 50 %.

References

- [1] Hummers WS, Offeman RE. Preparation of graphitic oxide. *Journal of the American Chemical Society*. 1958 Mar;80(6):1339.
- [2] Walley P, Zhang Y, Evans JRS. Self-assembly of montmorillonite platelets during drying. *Bioinspiration & Biomimetics*. 2012 Jul 27;7(4):046004.
- [3] Akelah A, Kelly P, Qutubuddin S, Moet A. Synthesis and characterization of "epoxyphilic" montmorillonites. *Clay Minerals*. 1994;29:169-78.
- [4] Zaarei D, Sarabi AA, Sharif F, Gudarzi MM, Kassiriha SM. Using of p-phenylenediamine as modifier of montmorillonite for preparation of epoxy-clay nanocomposites: Morphology and solvent resistance properties. *Polymer-Plastics Technology and Engineering*. 2010 Jan 29;49(3):285-91.
- [5] Uhl A, Sigusch BW, Jandt KD. Second generation LEDs for the polymerization of oral biomaterials. *Dental Materials*. 2004 Jan 31;20(1):80-87.

Chapter 4

Development of Clay/Polymer Composites

4.1 Montmorillonite and polyvinyl alcohol nanocomposites by solution casting

In this part of work, high volume fraction MMT composites (40-70 vol. %) with water-soluble polymer poly (vinyl alcohol) were investigated by different instruments.

4.1.1 X-ray diffraction of MMT and its composite

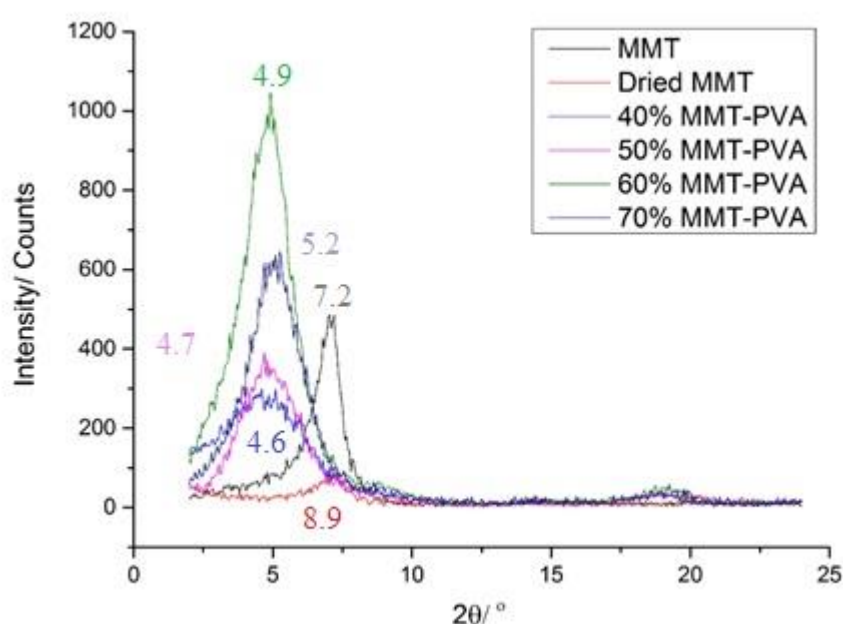


Figure 4-1. XRD traces for composites and for MMT-as received after drying for 864 ks (240h) at ambient temperature. The samples are identified by vol. %.

The results of the XRD peaks were given in Table 4-1. Untreated MMT has a peak at $2\theta=7.2^\circ$ which has a calculated d_{001} of 12.26 Å by Bragg's law and is in agreement with the properties shown in Figure 4-2, in which the interlayer spacing is 1.25nm.

Table 4-1. Results from XRD Figure 4-1.

Clay sample vol. % MMT	2 θ / °	Basal spacing/ Å	Change of d ₀₀₁ / Å
MMT	7.2	12.26	-
Dried MMT	8.9	9.93	-2.33
40	4.6	19.19	+6.93
50	4.7	18.79	+6.53
60	4.9	18.02	+5.76
70	5.2	16.98	+4.72

Nanofil® 116

Description:

Nanofil 116 is a natural montmorillonite.

Designed Used:

Nanofil 116 is an additive for plastics and rubber to improve various physical properties, such as reinforcement, CLTE, synergistic flame retardant and barrier.

Typical Properties:

Product Form: Powder
 Color: Off White
 Bulk Density: 340g/l
 Median Particle Size: 12 μ m
 Loss on Ignition: 8%
 Moisture Content: 11%
 Modifier Content: none
 Interlayer Spacing: 1.25nm
 Modifier: none
 Cation Exchange Capacity: 116meq/100g clay

Figure 4-2. Properties of Nanofil 116 from Rockwood, USA.

When MMT was dried in a vacuum oven at 60 °C for 12 hr, gallery water was lost and the inter-planar spacing decreased to 9.93 Å. There is about 6-11 wt. % gallery water and the collapse has been observed by others [1]. The graphs of composites (40 vol. %, 50 vol. %, 60 vol. % and 70 vol. %) showed a shift in peak to a lower angle, which meant that the basal spacing increased and the polymer intercalated without breaking the MMT structure.

4.1.2 SEM figures of MMT and PVA composites

The polymer-modified and unmodified clay sheets have a similar microstructure where the alignment of clay platelets and groups of platelets is obvious and unidirectional at the magnification observed. This shows that the PVA does not

disrupt the ordered structure obtained by slow drying of clay suspension despite the fact that it would have adsorbed on the clay and acted as a steric stabilizing adsorbate, potentially changing the way the platelets assemble. The structure of the unmodified MMT sheet seen in Figure 4-3 agrees with the results observed by Walley et al. [2]. The voids within the structures of the MMT sheets are relatively large compared to a single platelet and seem to be empty of polymer Figure 4-4 (a-d).

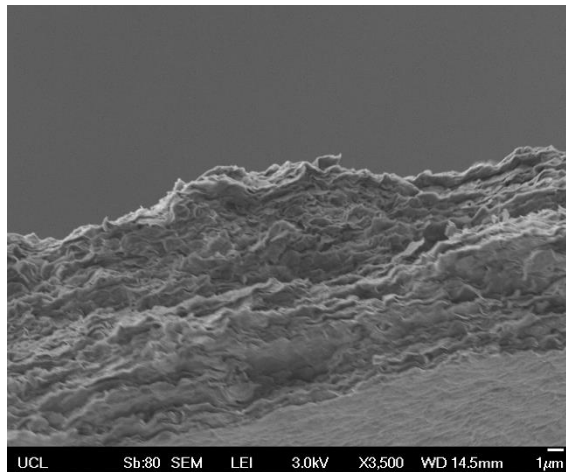
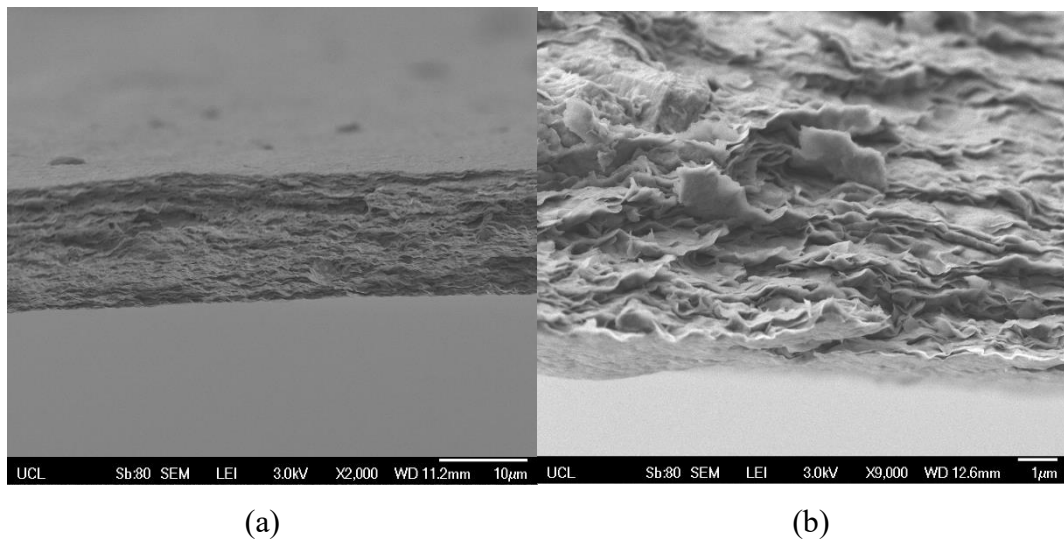


Figure 4-3. SEM image of fracture surface of MMT sheet slowly dried from suspension.



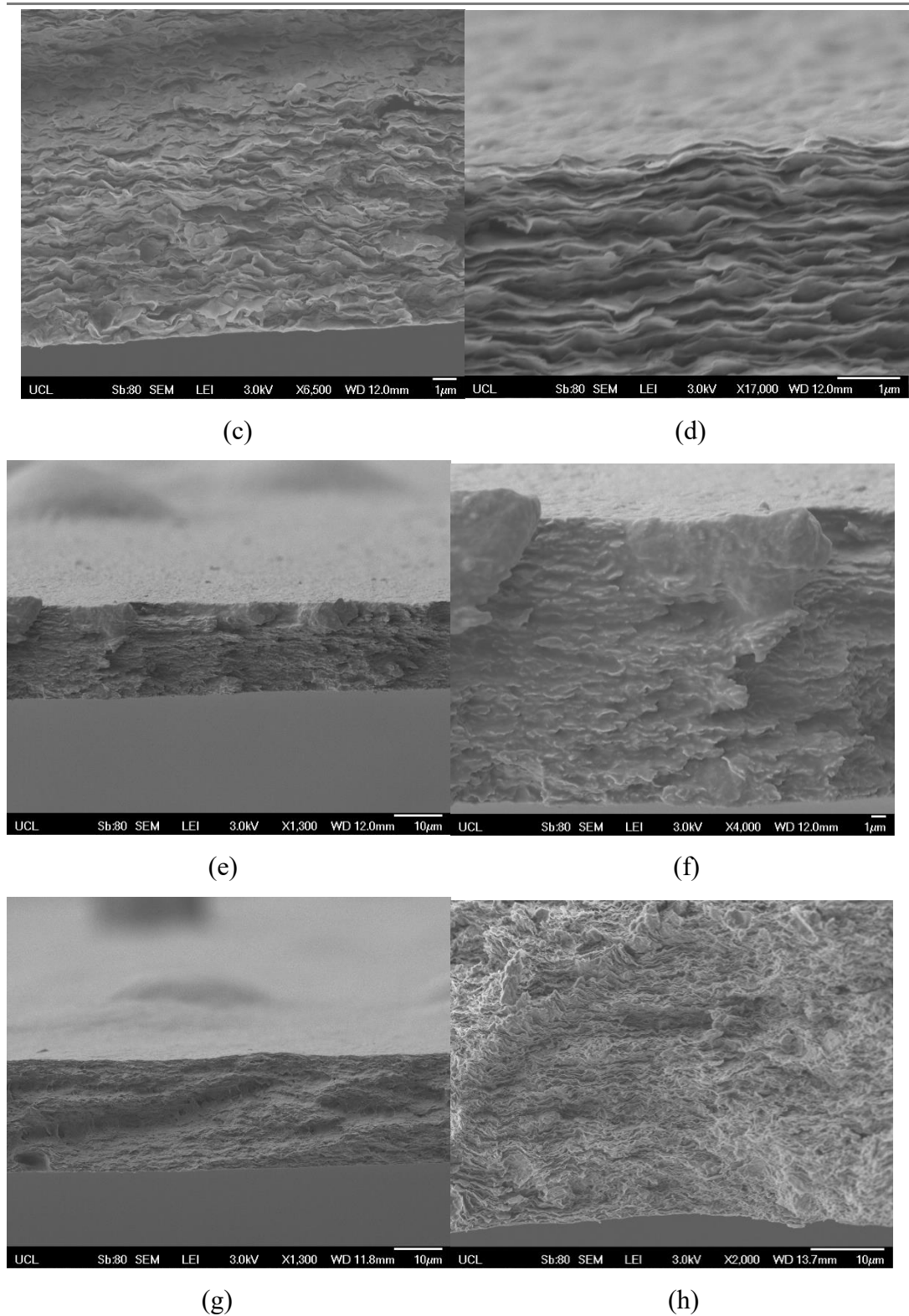


Figure 4-4. Scanning electron micrographs of cryogenic fracture surface of (a) & (b) 70 vol. % clay with 30 vol. % PVA composites; (c) & (d) 60 vol. % clay with 40 vol. % PVA composites; (e) & (f) 50 vol. % clay with 50 vol. % PVA; (g) & (h) 40 vol. % clay with 60 vol. % PVA.

As shown in Figure 4-4, the ordered structure was obtained for all these diverse clay volume fractions. PVA was absorbed at the surface of clay and a repulsion force between polymers can determine the spacing between two clay layers.

4.1.3 EDS of 50 vol. % MMT/PVA nanocomposite

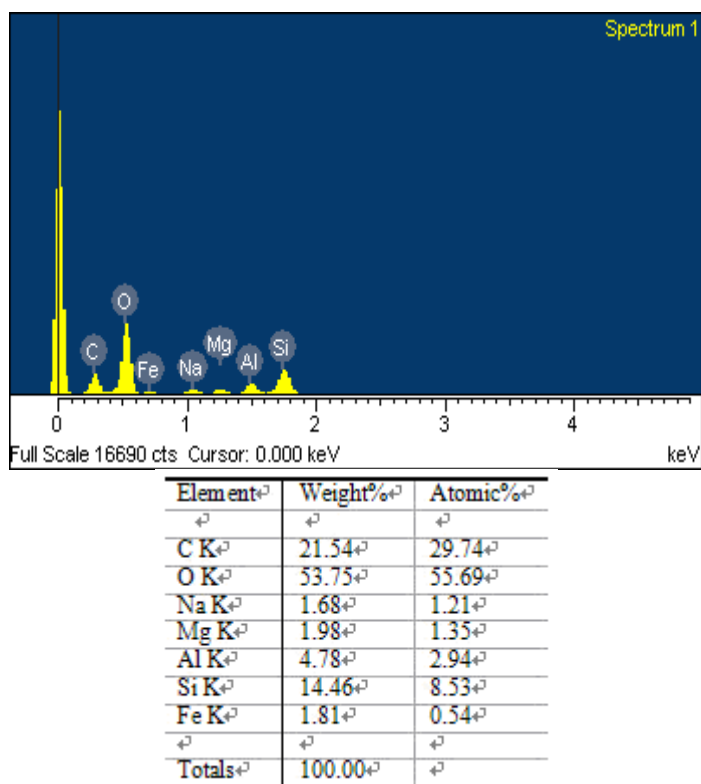


Figure 4-5. EDS spectrum of elements from MMT/PVA composite.

The EDS spectrum came from the cross section of the 50 vol. % MMT/PVA composites. Figure 4-5 shows the elements come from PVA (carbon and oxygen) and MMT (sodium, magnesium, aluminium, silicon, oxygen and iron). It is noteworthy that a significant iron content (approximately 1.81 wt. %) is found.

4.1.4 Mechanical testing

Mechanical testing was carried out on small number of samples and the results are displayed in Tables 4-2. All of the samples were cut by hot knife and the width was 10 ± 0.1 mm. The thickness of each sample was read by micrometer. The calibration of tensile test machine is 95 %.

Table 4-2. Failure of MMT/PVA composites.

vol. % MMT	Thickness / μm	Load Failure / N	Stress* at failure MMT/PVA composite /MPa
40	45 ± 0.5	12.2	26.7 ± 0.4
50	38 ± 0.5	15.4	40.5 ± 0.6
60	30 ± 0.5	3.6	12.0 ± 0.2
70	35 ± 0.5	2.4	6.9 ± 0.1

* mean of three tests

As Table 4-2 shown, the tensile strength is quite low compared with nature nacre even with the same brick and mortar structure. The best result of composites is just 40.5 ± 0.6 MPa coming from a 50 vol. % MMT/PVA composite.

The results shown in Table 4-2 are partly because less polymer gets involved in the structure: there are more spaces between MMT plates that need to be filled as the volume fraction of MMT increases and there is less PVA. Therefore, the distance between layers decreased when the MMT volume fraction increased.

The reason why MMT/PVA composite is a layer-by-layer structure is because during drying, Na^+ and Ca^{2+} concentration increase which may repel some cations into the adsorbed layer and neutralize the negative charge of clay particles. This appearance can lead to a thinner electrical double layer. Under this situation, the repulsion force between clay layers decreased and allowed them to arrange in layers by van der Waals attraction.

The mechanical test results show a decrease in failure stress on going from a high-polymer 50 vol. % clay sheet to low-polymer content sheet (30 vol. %) of 40.5 MPa to 6.9 MPa. As previous research indicated [3, 4] the MMT platelets could be covered by about a 0.5 nm thickness layer of polymer on top and bottom, forming a sandwich structure of 0.5-1-0.5 nm polymer/MMT system. Therefore, a high clay content cannot be fully covered due to the shortage of polymer. Based on this, MMT could easily gather and form an agglomerated structure which can lead to a stress concentration and lower mechanical properties.

As reported [5] the strength of natural nacre is between 40-100 MPa. However, the material which comprised MMT/PVA in this work has much lower strength compared with nacre. One group in Helsinki [3] reported the material they made reached approximately 165 MPa. Moreover, the group in Michigan [6] who synthesised similar nanocomposites by the LBL method accomplished 150 MPa and after crosslinked by glutaraldehyde, their strength of composites was as high as 400 MPa.

The reason why the MMT/PVA composite has such a low tensile strength will be further discussed in section 4.2.

4.2 Factors affecting mechanical properties of MMT/PVA composite

To account for the tensile strength differences, three hypotheses can be raised. The first is the clay which was used in this research, being different in origin to that used in comparative work provides weak mechanical properties. In this case, a different clay was chosen to use in the project. Black Hills bentonite, a raw montmorillonite clay was treated by sedimentation as a purification step which drops 20 % of coarse particulate impurity and then treated by the same method as the Nano116 MMT film formation procedure which was described in Section 3.2.1. After drying for two weeks, the film was tested and the result (20-40 MPa) shows there is not a significant difference compared with the Nanofil116 grade MMT.

It could be argued that the reduced strength obtained in the results reported in Section 4.1.4 compared with those reported in the literature by Wang and co-workers [7] was attributable to the different grades of polymer. Wang et al. used grade 99%+ hydrolyzed PVA from Sigma-Aldrich with molecular weight 146-186 kDa whereas the results reported in Section 4.1.4 used 85-124 kDa also from Sigma Aldrich. The former was therefore obtained and the experiments repeated exactly without modifying other variables.

The results provide a comparison for several volume fractions, 40, 50, 60 vol. % and

70 vol. % clay and indicate that irrespective of volume fraction there is no significant difference attributable to the PVA type despite small differences in molecular weight. Subsequent experiments therefore addressed other differences between the two laboratories.

The last one was the method by which the clay was dispersed in this research. The group in China [7] centrifuged the MMT suspension before mixed with PVA. The centrifugation step was then undertaken. The impurities and unexfoliated MMT were removed from the suspension after centrifugation. Figure 4-6 shows an example of large particles in the MMT/PVA composite without centrifugation which can degrade the mechanical properties.

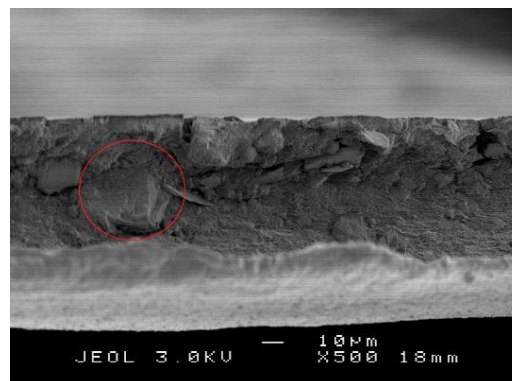


Figure 4-6. Particle (size around 20 μm) observed by SEM before centrifugation process.

All of those particles are the main cause of defects in MMT/PVA thin film introducing stress concentration effects which are indicated below. Geometric discontinuities, such as notches and holes as well as foreign particles or even large platelets, can form a higher stress field nearby. In consequence, a material could break at a lower strength than its theoretical value due to the concentrated stress [8]. Therefore, removing such defects or contaminants increased the failure strength of composite.

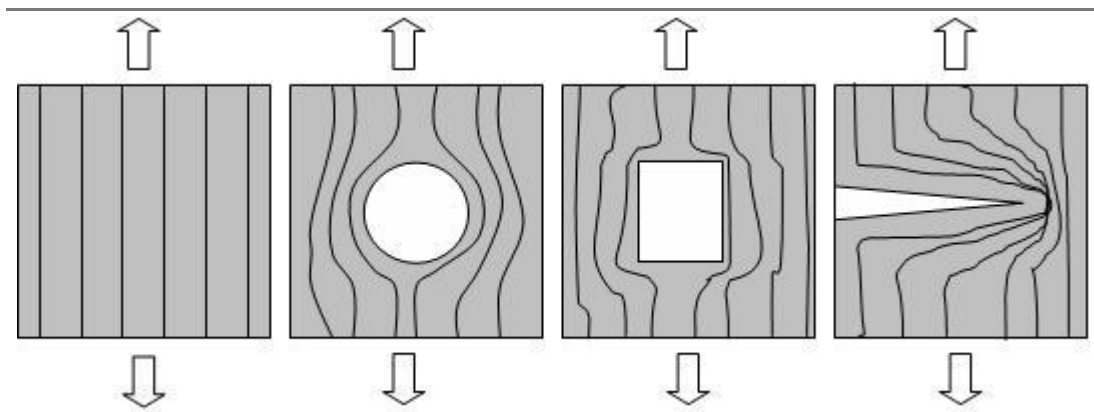


Figure 4-7. Effect of geometric discontinuities on stress distribution. [9]

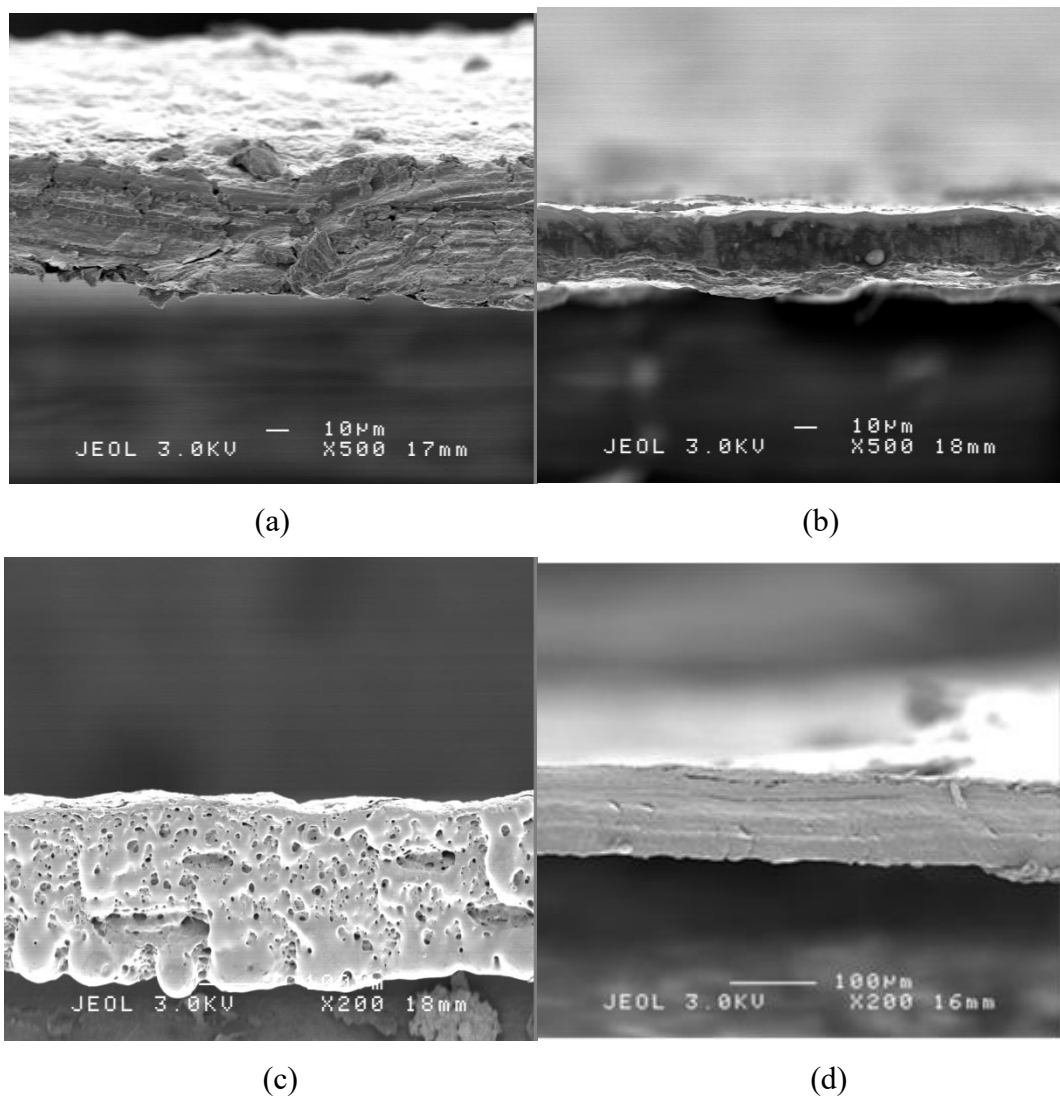


Figure 4-8. The effect of different cutting methods on the edge of composite samples: edge damage can affect the mechanical strength measurement. These are SEM images after preparation by (a) hot knife, (b) scissors, (c) laser cutter, (d) blade.

Despite the innate geometric discontinuities of the MMT/PVA composite, the surface irregularities such as cutting lines and depression created by SEM sample preparation could also cause the stress concentration. See Figure 4-8.

The samples were cut by a hot knife in the tensile testing reported in Section 4.1.4. After heating for 2 min, a hot knife was introduced to the edge of the sample. The edge collapsed during cutting by the shrinkage of PVA which can cause the degradation of mechanical strength. (Figure 4-8(a))

Figure 4-8 (b) shows samples prepared by scissors appeared depression, while in Figure 4-8 (c), the composite was cut into stripes by a laser cutter. Due to the high energy of the laser, polymers were melted and formed beads along the edge. Theoretically, all of these defects can degrade the tensile strength of composite.

Thus, a low temperature process was used and the samples were cut into stripes with a blade. They were placed on graph paper and a disposable scalpel was applied to cut composites in a straight parallel direction (Figure 4-8 (d)).

Given that the cutting process may introduce the residual stresses, annealing was used after blade cutting.

4.3 Characterisation of modified composites

4.3.1 Study of MMT size after centrifugation

Atomic force microscopy was operated to characterise the size of MMT clay platelets. As reported by Das [10], the mean aspect ratio is calculated by:

$$\text{Aspect ratio} = \frac{d}{t} \quad (4-1)$$

where d is the diameter and t is the thickness of MMT.

For the irregular clay platelets, the aspect ratio was given as the ratio of square root of area to the thickness [7], which was written as

$$S = \frac{\sqrt{A}}{t} \quad (4-2)$$

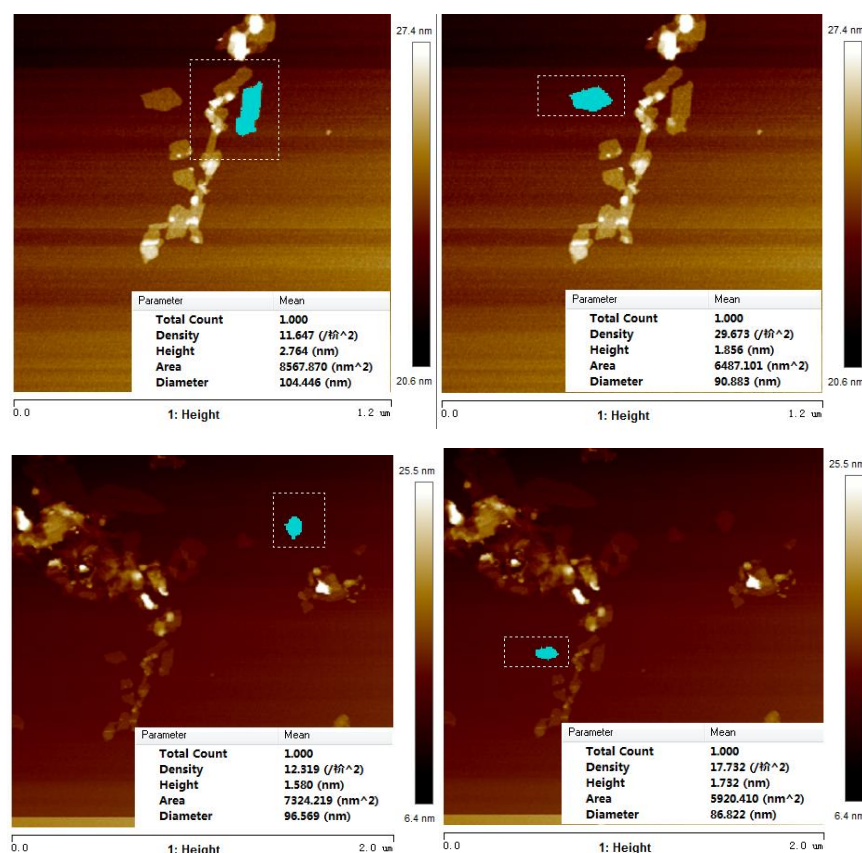


Figure 4-9. Examples of individual MMT platelets by AFM.

Table 4-3. Aspect ratio calculation from AFM Figure 4-9.

Sample Number	Diameter / nm	Thickness / nm	Aspect ratio
1	90.1	1.9	49.0
2	79.3	2.4	33.4
3	115.6	3.4	33.6
4	104.4	2.8	37.8
5	75.8	1.8	42.6
6	86.9	1.7	50.2
7	96.6	1.6	62.1
Mean	92.8	2.2	44.1
Standard Deviation	± 13.0	± 0.6	± 9.6
Standard Error of the Mean*	± 4.9	± 0.2	± 3.6

*Standard error was calculated as the ratio of the standard deviation to the square root of the number of samples (n=7)

Therefore, the aspect ratio can be given as 44.1 ± 3.6 . In the meanwhile, the thickness of MMT was analysed by ‘section’ function of the software Nanoscope Analysis 1.7 as showing in Figure 4-10.

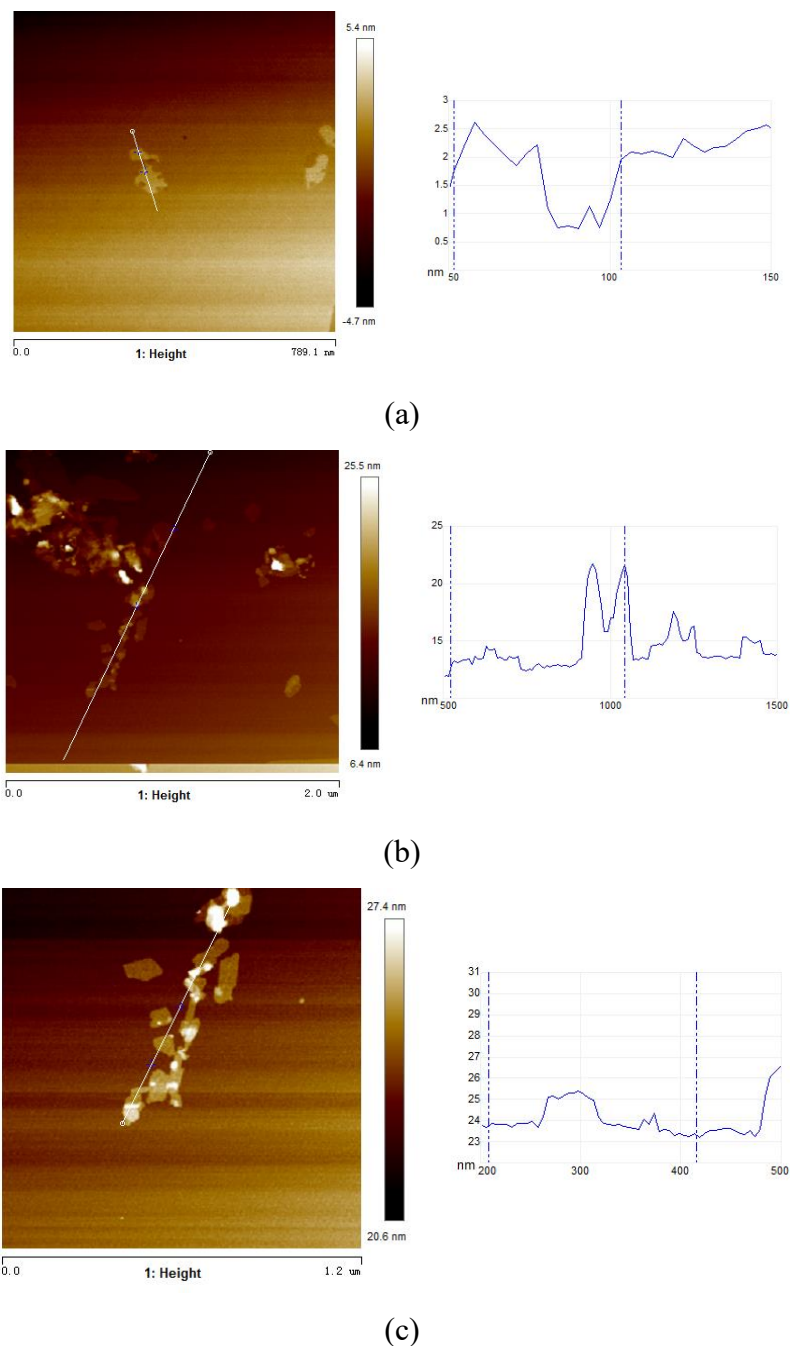


Figure 4-10. Examples for thickness analysis by AFM.

As seen in Figure 4-10, the thickness of MMT plates is less than 30 nm after centrifugation. The larger particles were removed and the remaining particles are smaller which is only no more than 30 layers, calculated as the ratio of the thickness

to the interlayer spacing of MMT (calculated from XRD trace in section 4.1.1) which is around 1.26 nm.

4.3.2 EDS analysis of elemental composition before and after centrifugation

Two kinds of samples were analysed by EDS 7000, a raw Nanofil 116 MMT powder as received and another of the dried sediment which was obtained after centrifuging the MMT suspension at 6000 rpm (RCF=3340 g) for 30 min, as shown in Figure 4-11.




Figure 4-11. Sedimentation after centrifugation.

Before EDS detection, the sediment was dried in a vacuum oven at 80 °C for 2 hr.

Analysis Report							
No.		Operator		Sample Image			
Sample Name	MMT bottle		Meas.Date	2015-07-27 15:56			
Group	Yi Shi Helium		Comment	Quick&easy Air-Metal			
Memo	<div></div>						
<input checked="" type="checkbox"/> Measurement Condition							
Instrument: EDX-7000 Atmosphere: He Collimator: 5(mm) Sample Cup:Polypropylene							
Analyte	TG	kV	uA	FI	Acq.(keV)	Anal.(keV)	Time(sec) DT(%)
Al-U	Rh	50	76-Auto	----	0 - 40	0.00-40.00	Live- 60 30
Na-Sc	Rh	15	618-Auto	----	0 - 20	0.00- 4.40	Live- 60 30
Fe	Rh	50	76-Auto	----	0 - 40	6.20- 6.60	Live- 60 30
<input checked="" type="checkbox"/> Quantitative Result							
Analyte	Result		[3-sigma]	Proc.-Calc.	Line	Int.(cps/uA)	
Si	22.361 %		[0.066]	Quan-FP	SiKa	27.9088	
Al	7.745 %		[0.061]	Quan-FP	AlKa	3.7631	
Mg	2.700 %		[0.065]	Quan-FP	MgKa	0.3269	
Fe	2.347 %		[0.008]	Quan-FP	FeKa	153.6998	
Ca	1.200 %		[0.009]	Quan-FP	CaKa	4.3126	
K	0.180 %		[0.006]	Quan-FP	K Ka	0.4597	
Ti	0.179 %		[0.004]	Quan-FP	TiKa	3.4345	
Er	0.079 %		[0.009]	Quan-FP	ErLa	2.1346	
Sr	0.043 %		[0.001]	Quan-FP	SrKa	12.2850	
S	0.040 %		[0.003]	Quan-FP	S Ka	0.1473	
Zn	0.020 %		[0.001]	Quan-FP	ZnKa	2.4312	
Zr	0.017 %		[0.001]	Quan-FP	ZrKa	5.1577	
Cu	0.017 %		[0.001]	Quan-FP	CuKa	1.7438	
V	0.015 %		[0.002]	Quan-FP	V Ka	0.4163	
Mn	0.014 %		[0.002]	Quan-FP	MnKa	0.7001	
P	0.006 %		[0.006]	Quan-FP	P Ka	0.0100	
O	63.038 %		[-----]	Balance		-----	

(a)

Analysis Report							
No.		Operator		Sample Image			
Sample Name	MMT impurities		Meas.Date	2015-07-27 16:48			
Group	Yi Shi Helium		Comment	Quick&easy Air-Metal			
Memo	<div></div>						
<input checked="" type="checkbox"/> Measurement Condition							
Instrument: EDX-7000 Atmosphere: He Collimator: 5(mm) Sample Cup:Polypropylene							
Analyte	TG	kV	uA	FI	Acq.(keV)	Anal.(keV)	Time(sec) DT(%)
Al-U	Rh	50	76-Auto	----	0 - 40	0.00-40.00	Live- 60 30
Na-Sc	Rh	15	676-Auto	----	0 - 20	0.00- 4.40	Live- 60 29
Fe	Rh	50	76-Auto	----	0 - 40	6.20- 6.60	Live- 60 30
<input checked="" type="checkbox"/> Quantitative Result							
Analyte	Result		[3-sigma]	Proc.-Calc.		Line	Int.(cps/uA)
Si	12.702 %		[0.039]	Quan-FP		SiKa	22.9128
Al	4.737 %		[0.040]	Quan-FP		AlKa	3.0288
Mg	1.633 %		[0.043]	Quan-FP		MgKa	0.2462
Fe	1.260 %		[0.005]	Quan-FP		FeKa	146.1772
Ca	0.819 %		[0.005]	Quan-FP		CaKa	5.0001
K	0.161 %		[0.002]	Quan-FP		K Ka	0.6963
Ti	0.111 %		[0.002]	Quan-FP		TiKa	3.6681
Er	0.076 %		[0.005]	Quan-FP		ErLa	3.6372
S	0.038 %		[0.002]	Quan-FP		S Ka	0.2355
Sr	0.032 %		[0.000]	Quan-FP		SrKa	17.5353
Zr	0.016 %		[0.000]	Quan-FP		ZrKa	9.5942
P	0.015 %		[0.003]	Quan-FP		P Ka	0.0431
Zn	0.009 %		[0.000]	Quan-FP		ZnKa	2.0336
V	0.007 %		[0.001]	Quan-FP		V Ka	0.3111
Mn	0.006 %		[0.001]	Quan-FP		MnKa	0.5310
Cu	0.004 %		[0.001]	Quan-FP		CuKa	0.8121
Y	0.002 %		[0.000]	Quan-FP		Y Ka	1.3667
O	78.370 %		[-----]	Balance			-----

(b)

Figure 4-12. EDS shows the elemental composition of (a) Nanofil 116 MMT, (b) sedimentation after centrifugation.

It is worth mentioning that before centrifugation was applied, the Fe takes up 2.347 ± 0.001 % in raw material and the Fe in sedimentation account for 1.260 ± 0.001 %. The Fe in MMT could affect optical and mechanical properties of MMT/PVA composite but it could also influence the catalytic effect on the clay on adjacent polymerisation reactions in Section 4.5.

4.3.3 Orientation function of Nanofil 116 MMT

In order to quantify the degree of MMT platelet orientation, a quantitative orientation function was sought; XRD measurements were undertaken to analysis the preferred orientation developed in a self-drying MMT sheet as indicated in Section 3.7.2.

The data were analysed by DIFFRAC.EVA software and Microsoft Excel. After integrating the line which corresponds to the MMT (002) plane where the peak is $2\theta=14^\circ$. The intensity of the (002) peak with the specific tilt angle is shown in Figure 4-13.

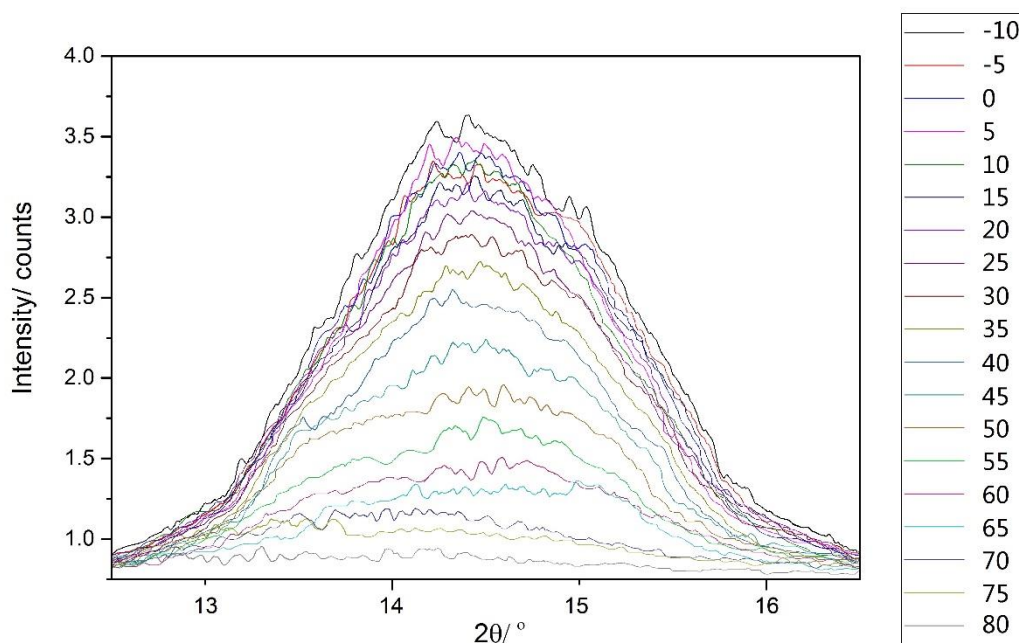


Figure 4-13. XRD data showing the intensity of the (002) peak for each tilt angle, - 10° to 80° in 5° step.

Then, the integrated intensity of each peak was plotted against a given tilt angle to

acquire an orientation function curve. A Gaussian function was given as:

$$I(\psi) = Ae^{\frac{-\psi^2}{2\sigma^2}} \quad (4-3)$$

Introducing the Gaussian function into Excel, using the ‘Solver’ function, the parameters A (scaling factor) and σ (standard deviation) were obtained as 20.54 and 18.24, respectively.

Then using the fitting parameters A and σ , Equation 4-3 can be plotted as Figure 4-14.

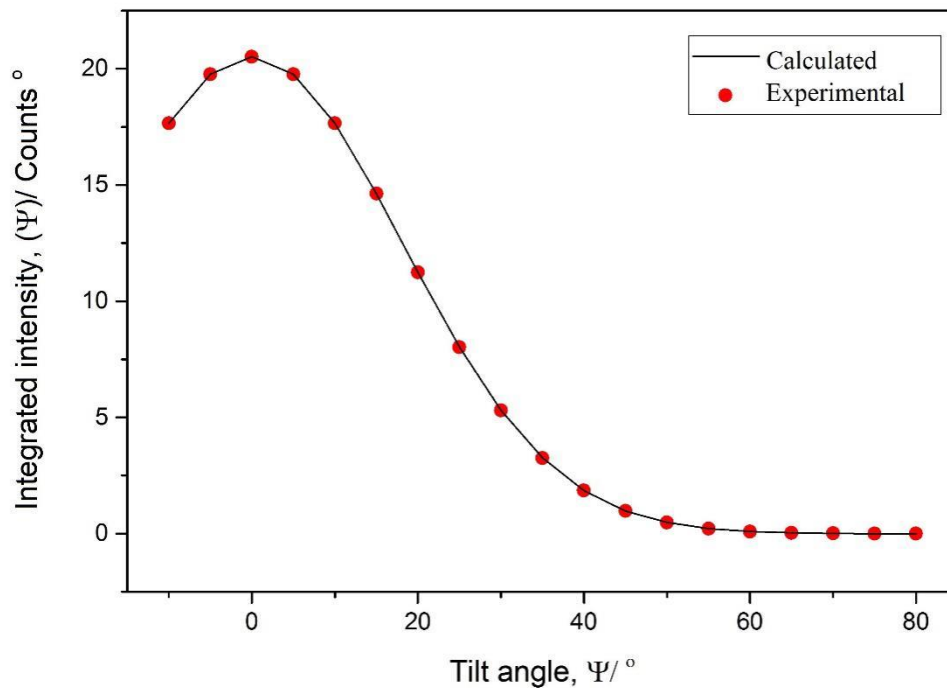


Figure 4-14. Graph showing experimental MMT orientation distribution function.

The distribution shows that a very strongly ordered structure was obtained by the self-drying process and the orientation function curve showed preferred orientation were occurred within the absolute value of tilt angle $\leq |15^\circ|$ which agrees with Figure 4-4 (b) and (d). The derivation from the pure planar-random arrangement is also seen in other work on ordered clay composites such as Podsiadło [6], though it was not measured quantitatively as in this work. The clay platelets tend to undulate [11] and the majority of platelets are not arranged exactly parallel as observed by the SEM figures of MMT cross sections. Das [10] used a method to quantify the orientation

function as

$$\text{Degree of orientation} = \frac{(180 - FWHM)}{180} \times 100\% \quad (4-4)$$

where FWHM is the full width at the half maximum of the peak in the azimuthal intensity profile. The sample (MMT/PVA composite) measured by Das in a tilt angle 10-15 ° which gave a 78 % degree of orientation [10].

Table 4-4. The degree of orientation of different tilts.

Tilt degree/ °	I(ψ)	Degree of orientation / %
-10	17.652 ± 0.001	12.478 ± 0.001
-5	19.758 ± 0.001	13.967 ± 0.001
0	20.515 ± 0.001	14.502 ± 0.001
5	19.758 ± 0.001	13.967 ± 0.001
10	17.652 ± 0.001	12.478 ± 0.001
15	14.629 ± 0.001	10.341 ± 0.001
20	11.246 ± 0.001	7.950 ± 0.001
25	8.020 ± 0.001	5.669 ± 0.001
30	5.305 ± 0.001	3.750 ± 0.001
35	3.255 ± 0.001	2.301 ± 0.001
40	1.853 ± 0.001	1.310 ± 0.001
45	0.978 ± 0.001	0.691 ± 0.001
50	0.479 ± 0.001	0.339 ± 0.001
55	0.218 ± 0.001	0.154 ± 0.001
60	0.092 ± 0.001	0.065 ± 0.001
65	0.036 ± 0.001	0.025 ± 0.001
70	0.013 ± 0.001	0.092 ± 0.001
75	0.004 ± 0.001	0.031 ± 0.001
80	0.001 ± 0.001	0.001 ± 0.001
Total	141.465 ± 0.001	100 %

Degree of orientation of MMT sheets at various tilts is given in Table 4-4. The degree is calculated by a given tilt I (ψ) divided the total I (t). To be concluded, the

degree of orientation in the range -10° to 10° tilt angle is sum by $I_{(-10^\circ)}$ to $I_{(10^\circ)}$, which is then given as $67.392 \pm 0.001 \%$.

4.3.4 Thermal analysis of MMT/PVA composites

Thermal behaviour of the MMT/PVA composites was analysed by differential scanning calorimetry (DSC) and thermal gravimetric analysis (TGA). The results are given in Figure 4-15 and 4-16.

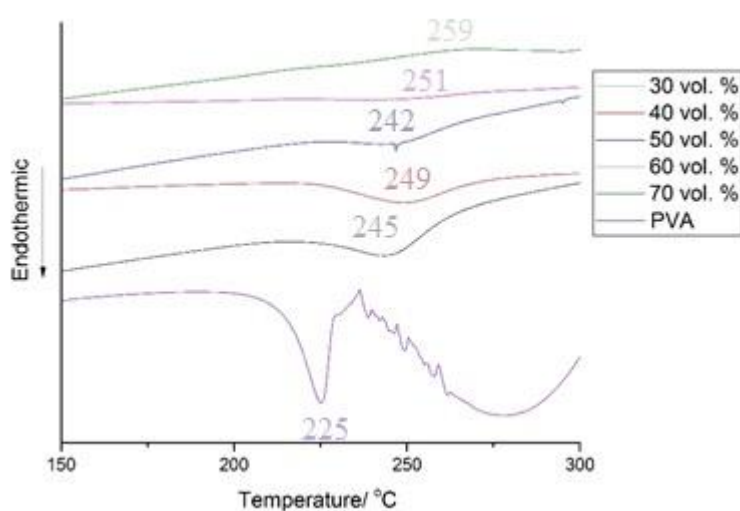


Figure 4-15. DSC of MMT/PVA composite. The samples are given as the volume percentage of clays and each T_m of the sample was given as number.

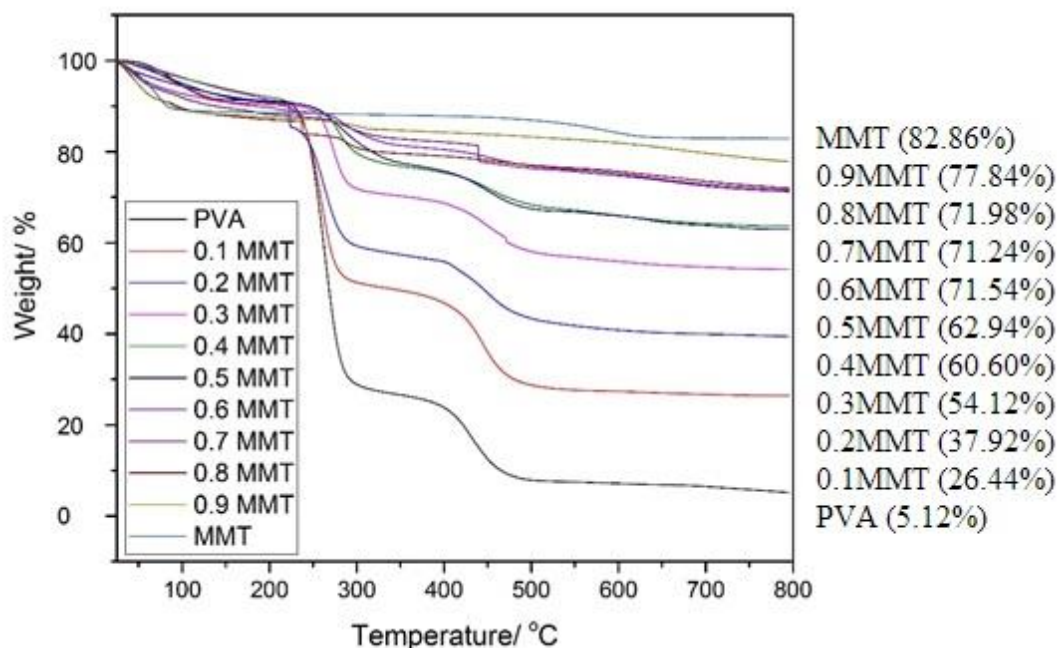


Figure 4-16. TGA of MMT/PVA composites. The samples are identified as volume fraction of MMT.

The melting temperature of PVA was given as 220-260 °C by the supplier. The melting temperature of the composite was shown to have slightly increased in Figure 4-15. It could be a possible explanation that the clay content confined the movement of polymer segments by adsorption on the high available surface area ($650 \text{ m}^2 \cdot \text{g}^{-1}$ for fully exfoliated MMT) and this produced the increase in melting point. If so, it should also lead to a low-permeability nanocomposite system because gaseous diffusion is restricted in the region of immobilised adsorbate [12, 13].

Table 4-5. Analysis of the TGA and DSC data.

Sample	wt. % MMT calculated from vol. %	wt. % of material residue after TGA	wt. % of MMT calculated from TGA results	T _m / °C	ΔH _m / J g ⁻¹	X _c %
Pure PVA	0	5.12	0	-	30.52	22.02
10 vol. % MMT	21.35	26.44	27.43	-	-	
20 vol. % MMT	37.92	39.41	44.10	-	-	
30 vol. % MMT	51.15	54.12	63.03	-	8.74	17.06
40 vol. % MMT	61.96	60.60	71.37	243.39	5.66	14.25
50 vol. % MMT	70.95	62.94	74.37	248.94	5.15	14.51
60 vol. % MMT	78.56	71.54	85.44	-	-	-
70 vol. % MMT	85.07	71.24	85.05	-	-	-
80 vol. % MMT	90.72	71.98	86.00	-	-	-
90 vol. % MMT	95.65	77.84	93.54	-	-	-
Pure MMT	100	82.86	100	-	-	-

The degree of crystallinity was calculated by parameters deduced from the TGA and DSC traces, and is given in Table 4-5. The degree of crystallinity was found from equation 4-5,

$$X_c = \frac{\Delta H_m}{\Delta H_0 \times (1 - w)} \quad (4-5)$$

where ΔH_m is the melting enthalpy measured in Origin by integrating the melting peak. ΔH_0 is the enthalpy of 100 % crystallinity PVA given as $138.6 \text{ J}\cdot\text{g}^{-1}$ [14-16]. w is the weight percentage of the MMT content in composites, which is calculated by wt. % of the composite after TGA minus 5.12 (data from 100 wt. % PVA after TGA), and then divided the wt. % from 100 wt. % MMT after TGA (given as 82.86) minus 5.12. Considering the 90 vol. % material as an example:

The weight percentage is 77.84 after TGA and this number was contributed by residue from both MMT and PVA. The weight percentage of MMT was then give as

$$w_{90} = [(77.84 - 5.12) / (82.86 - 5.12)] \times 100 \% = 93.54 \% \quad (4-6)$$

The calculated data from TGA was $w_{90} = 93.54 \%$. There is a slight difference from the data calculated from the vol. %, which is 95.65 %, which may be caused by experimental error.

4.3.5 Mechanical properties of MMT/PVA composites

Padawer and Beecher [17] give a function to estimate the Young's modulus of a composite which is enhanced by platelet reinforcement.

$$Y = \alpha \phi_R Y_R + (1 - \phi_R) Y_m \quad (4-7)$$

where α is the 'Modulus reduction factor', which is defined as a function of μ ,

$$\alpha = 1 - \frac{\tanh(\mu)}{\mu} \quad (4-8)$$

where $\tanh(\mu)$ is the function given as

$$\tanh(\mu) = \frac{e^{2\mu} - 1}{e^{2\mu} + 1} \quad (4-9)$$

where μ is indicated by the function below,

$$\mu = s \cdot \sqrt{\frac{G_m \cdot \phi_R}{Y_R \cdot (1 - \phi_R)}} \quad (4-10)$$

where s is the aspect ratio of clay platelets which can be deduced from the results of AFM and Φ_R is the volume fractions of reinforcement, which is calculated by the data derived from TGA using function,

$$\phi_R = \frac{\omega / \rho_R}{\omega / \rho_R + (1 - \omega) / \rho_m} \quad (4-11)$$

The density of polymer matrix is $1269 \text{ kg}\cdot\text{m}^{-3}$ and that of reinforcement clay is $3100 \text{ kg}\cdot\text{m}^{-3}$, respectively. Y_R and Y_m are the Young's modulus of MMT and PVA. Y_m is $0.17\text{-}0.36 \text{ GPa}$ [18] for which 0.27 GPa was picked as median. In terms of smectite clay platelet, the Young's modulus of platelet is in the range $178\text{-}265 \text{ GPa}$, given by Chen and co-workers [19]. To be specific, Young's modulus of MMT is indicated as 270 GPa by Manemvitch [20]. G_m is the shear modulus of polymer which can be calculated by,

$$G_m = \frac{Y_m}{2(1 + \nu)} \quad (4-12)$$

where ν is Poisson's ratio of polymer. For PVA, it is usually taken as $0.42\text{-}0.48$ [21] since PVA is close to incompressible. In calculation, the Poisson ratio was chosen as the median 0.45 .

Then introducing all of these values, the Young's modulus can be predicted as a function of clay content.

Tensile strength testing was undertaken at ambient conditions defined as temperature $21 \pm 2 \text{ }^\circ\text{C}$ and humidity $60 \pm 10 \text{ \%}$. It is reported by Patro and Wagner [22] that a higher humidity (60 \%) could promote the movement of PVA along the stress direction, resulting in a higher strain compared with 45 \% humidity. Moreover, researchers [22-24] report the ultimate strength of PVA film are 83 MPa [23] at 35 \% humidity, 65 MPa [22] at 45 \% humidity, 22.5 MPa at 50% humidity [24], 29 MPa at 70% humidity [22], which can give a basic idea how the strength responds to the changing of humidity.

A series of tensile tests based on the different volume fraction MMT and PVA composite was carried out to evaluate mechanical properties of nanocomposites. Thickness of each sample was measured 3 times by micrometre and given as the mean of three readings. There were 3 samples for each of the volume fractions of MMT ranging from $30\text{-}70 \text{ vol. \%}$. The samples were cut into stripe with the width 10

± 0.1 mm and length 50 ± 0.1 mm. An example was given as 50 vol. % (Highest stress among samples) MMT/PVA composite, shown in Figure 4-17.

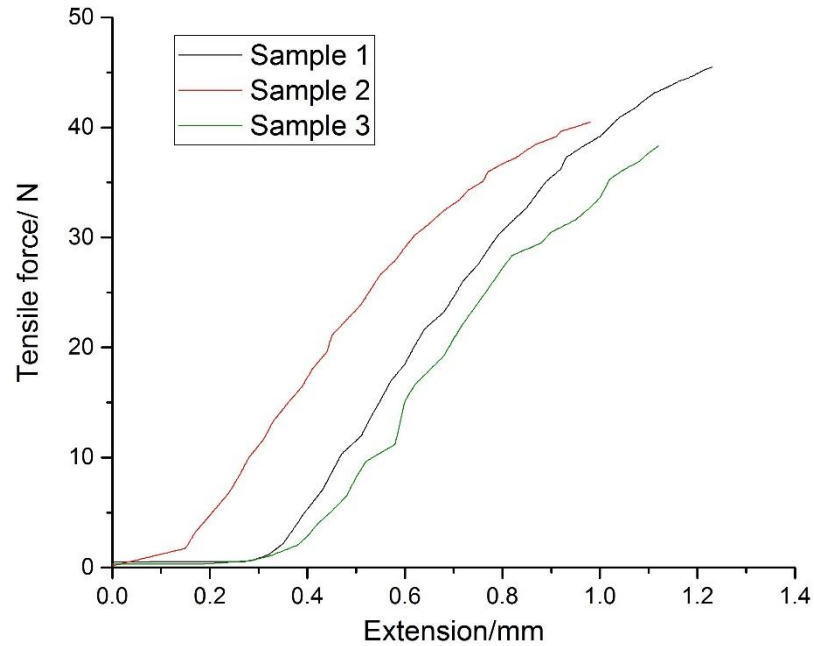


Figure 4-17. An example of tensile strength test of 50 vol. % MMT/PVA composite.

Table 4-6. The raw and calculated data for tensile testing of MMT/PVA composites.

Sample	vol. %	Thickness/ μm	Ultimate force / N	Ultimate Stress/ MPa
MMT*				
30		55.0 ± 0.5	38.81	70.56 ± 1.0
40		52.3 ± 0.5	28.48	54.46 ± 0.8
50		42.2 ± 0.5	41.44	98.20 ± 1.5
60		35.6 ± 0.5	6.76	18.99 ± 0.3
70		32.7 ± 0.5	5.35	16.36 ± 0.3

*Values were given as the mean of three samples

Comparing the results in Table 4-2 and Table 4-6, it can be indicated that the tensile strength of composites shows a significant increase in each of the volume fractions of MMT. After introducing centrifugation into the process, the tensile strength increased from 40.5 to 98.2 MPa (50 vol. % MMT/PVA composite). The Young's modulus of the composites was also investigated and the results were given in Table 4-7.

Table 4-7. Young's modulus of composites.

Sample vol. % MMT	Extension/ mm	Young's modulus/ GPa	*Prediction Young's modulus/ GPa
30	1.11	3.18	7.15
40	1.17	2.33	13.81
50	1.11	4.42	23.94
60	0.37	2.57	38.89
70	0.29	2.82	60.87

*Values were calculated from the Padawer-Beecher function

It can be seen from Table 4-7 that the values calculated from the tensile test result are far behind compared with the prediction value of Padawer Beecher law. The reason could be the test was carried out under a high relative humidity. The Young's modulus was defined as the ratio of stress to strain. It can be deduced as,

$$Y = \frac{\sigma}{\varepsilon} = \frac{FL}{A\Delta L} \quad (4-13)$$

where F is the tensile force, A is the area of cross section of sample, ΔL is the extension of the sample and L is the original length of the sample.

As described before, there is a trend that under a high humidity, the strain could be increased by the promoted movement of PVA along the stress direction, effectively a plasticization of PVA by water. In the meanwhile the stress could be decreased by the absorbed water vapour. In this case, the calculated Young's modulus is much smaller than the prediction, as shown in Table 4-7.

4.3.6 Weibull modulus

According to Weibull statistics, the relationship between average strength, $\bar{\sigma}$ of two batches, 1 and 2 of volumes V_1 and V_2 is given by:

$$\frac{\sigma_1}{\sigma_2} = \left(\frac{V_2}{V_1}\right)^{\frac{1}{m}} \quad (4-14)$$

where $\bar{\sigma}$ is the average strength of the sample, V is the volume of the sample and m

is the Weibull modulus. If all defects are the same size throughout the population, there is no variation in strength and the Weibull modulus approaches infinity so that $1/m \rightarrow 0$ and hence $(V_1/V_2)^{1/m} = 1$ so that there is no effect of volume of sample under test. A low Weibull modulus, on the other hand, means a wide distribution of defect sizes and in this case the difference of strengths caused by volume is much greater.

Different investigators have quoted different strengths for ordered nanocomposites but those differences are only partly due to different materials: some of the difference is due to different sample volumes. In reference 6, for example, the test-piece was less than 2 μm thick. It is therefore possible to correct for the effect of different sample volumes as chosen by different investigators by using equation 4-14 to bring all measurements back to the volume of the ASTM standard test-piece. However this requires a knowledge of Weibull modulus and these may differ: they are not quoted. Among different research groups [3, 6, 7] of MMT/PVA composites, they all announced that the composites have high strength and high toughness. A typical value for the Weibull modulus of a high performance fibre composite is around 20. [25] Therefore, the reconciliation of sample volume effects is based on equation 4-14 with a Weibull modulus of 20.

As recommended from ASTM 3039D for tensile testing of composites, the geometry of the specimen is given as width 15 mm, length 250 mm and thickness 1 mm. In this case, the modified strength can be calculated in the same volume, which is $3.75 \times 10^{-6} \text{ m}^3$. The results are given in table 4-8. It can immediately be seen that some of the very high values of strength quoted are brought low by this volume reconciliation and indeed the range of different strengths attributed to different investigators is now much narrower and probably more realistic.

Table 4-8 Modified Strength under the ASTM volume in the same weibull modulus

	Ref [3]	Ref [6]	Ref [7]	This project
Length/ mm	20	5	50	50
Width/ mm	3	1	3	10
Thickness/ μm	40*	1.48*	8*	22.5*
Strength/ MPa	165	150	219	98
Modified Strength/ MPa	114.6	76.14	146	73.6

* Means of the thickness

4.4 Clays and epoxy resin system

Epoxy resins are formed from oligomers which include more than one epoxy group. Generally, they can be cured with many kinds of curing agents and can be cured over a wide range of temperature. After curing, the product generally presents low volume shrinkage. Moreover, there is almost no volatile outgrowth in the process. With such excellent properties, epoxy resins are used in many industrial applications, such as coatings, adhesives and as the matrix of carbon or glass fibre reinforced composites as well.

Polyamines and polyacids are the major curing agents used in epoxy resins as they contain active hydrogen atoms in their structures. Liquid polyamines such as diethylene triamine and trimethylamine are the most widely-used agents [26]. Extra promoters (such as polythiol) are often added when the epoxy resin is to be cured at room temperature in order to achieve rapid curing. The selection of epoxy curing agent depends on the curing temperature. Polyamine is generally used at normal temperatures while for high temperatures, the curing agent is usually chosen to be a polyacid or anhydride [26-28].

4.4.1 XRD of clays and clays resin mixture

To verify the potential of the intercalation of epoxy resin for clays, XRD was used to

measure the interlayer spacing after epoxy resin was introduced. Figure 4-18 to 4-20 show the XRD peaks of clays and clay resin mixtures. For comparison, raw clays including Nanofil 116, BH natural MMT and laponite were chosen for XRD measurement.

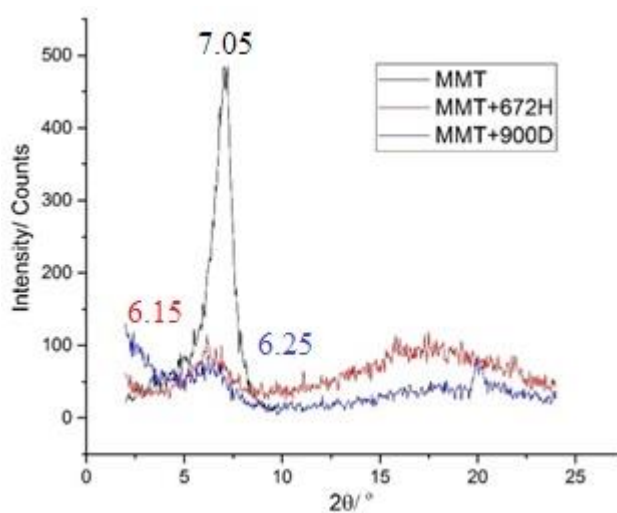


Figure 4-18. XRD traces for Nano116 MMT and MMT/resin mixture.

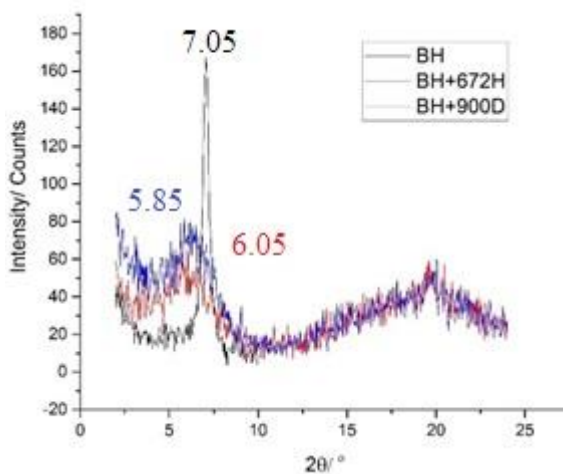


Figure 4-19. XRD traces for BH Natural and BH/resin mixture.

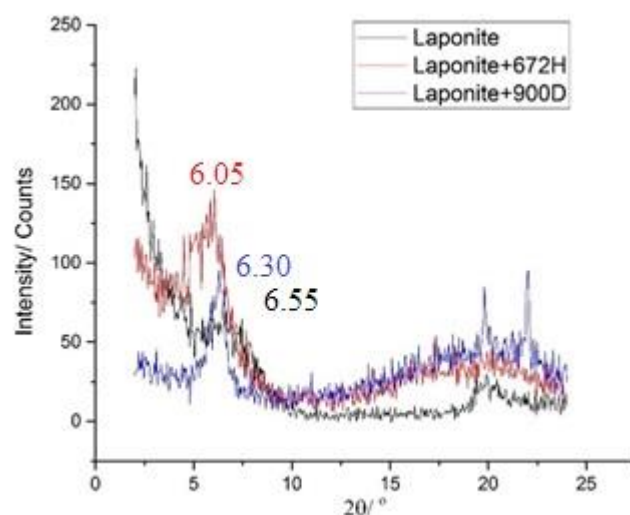


Figure 4-20. XRD traces for laponite and laponite/resin mixture.

The results of Figure 4-18 to 4-20 were calculated by Bragg's law and given in Table 4-9.

Table 4-9. Calculated data from XRD traces of clay and resin mixture.

Sample	$2\theta / ^\circ$	d_{001} spacing/ \AA	Increase in d_{001} / \AA
MMT	7.05	12.53	-
MMT + resin 672H	6.15	14.36	1.83
MMT + resin 900D	6.25	14.13	1.60
BH Natural	7.05	12.53	-
BH Natural + resin 672H	6.05	14.60	2.07
BH Natural + resin 900D	5.85	15.10	2.57
Laponite	6.55	13.48	-
Laponite + resin 672H	6.05	14.60	1.11
Laponite + resin 900D	6.3	14.02	0.53

All the XRD traces were analysed in Origin. Raw Nanofil 116 MMT, BH Natural MMT and laponite presented $d_{(001)}$ peaks at 7.05° , 7.05° and 6.55° respectively. All peaks showed a shift to a lower degree after introduced epoxy resin into clays. The shifted peaks indicate an increase in clay basal spacing. In other words, it proved the

possibility of resin intercalation before crosslinking. However, there were no significant differences in using different kinds of resin.

PPD was used as an ion exchange agent to generate an epoxyphilic MMT through amine-cation exchange with exchangeable cations in clays, like Na^+ or Fe^{3+} . XRD measurement was conducted to identify the changes in basal spacing of the PPD modified MMT.

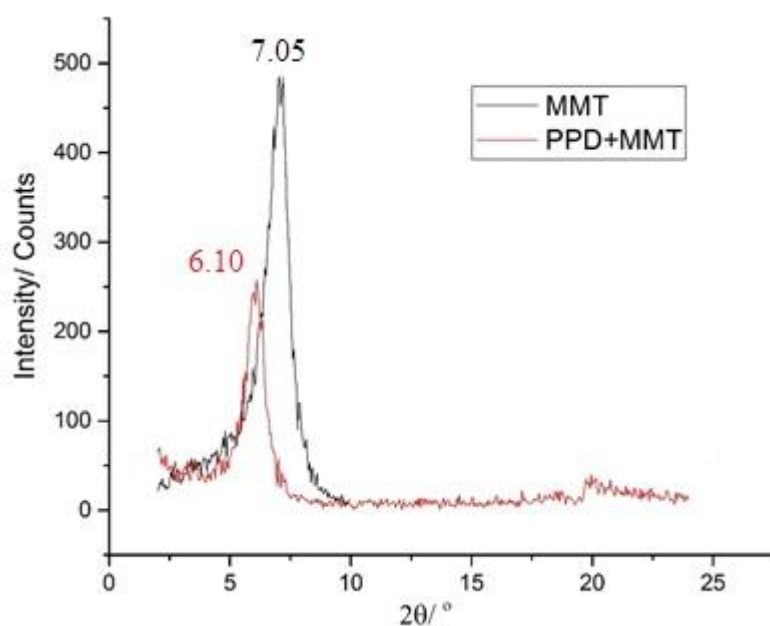


Figure 4-21. XRD traces of MMT and PPD modified MMT.

As shown in Figure 4-21, the peak of modified clay shifted from 7.05 ° to 6.10 °, which showed an increase of interlayer spacing from 12.53 Å to 14.48 Å after ions exchange.

4.4.2 SEM of self-assembled structure

Figure 4-22 showing variation clays and their cross sectional structure. As indicated in the Figure 4-22, it proved that hierarchical structures of clays were obtained by a drying process, which is agreed by the previous study in Section 4.1.2.

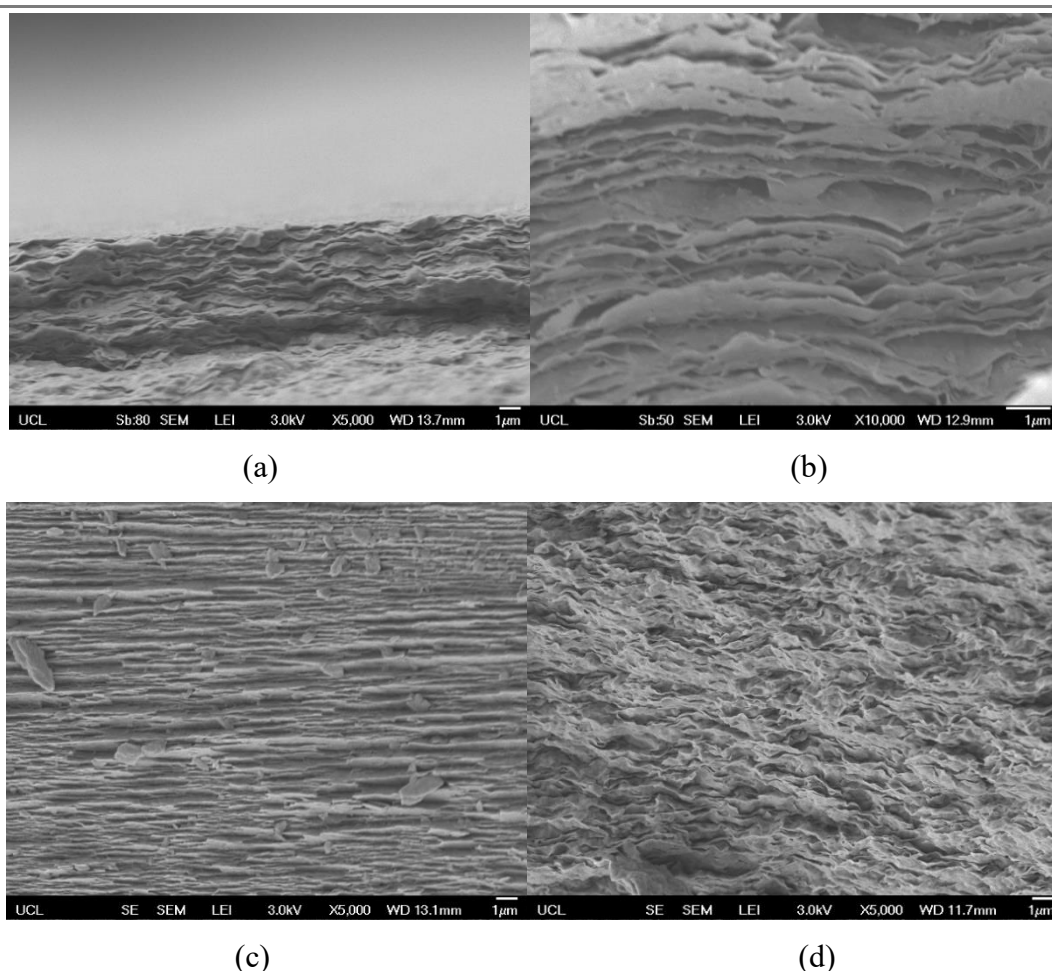


Figure 4-22. SEM of cross section of variation clays (a) Nano116 MMT, (b) BH Natural, (c) laponite, (d) PPD modified MMT.

MMT was explained in the previous study in terms of the structure and orientation function. Therefore, no further discussion of MMT is made in this section.

Laponite has a higher degree of ordered structure than MMT and the distance between plates is between 25-40 nm while in MMT it can be up to hundreds of nanometres.

The PPD modified MMT plates indicated a different microstructure compared with untreated Nanofil116 MMT clay. The cross section of PPD modified MMT still remained a layered structure. However, the curvature of layers increased which may be caused by promoted interactions between interlayers of the PPD modified MMT. This is possible due to the influence of π -interactions next to the alkylammonium groups in PPD.

The FTIR spectra of Nanofil 116 MMT and PPD modified clay are shown in Figure 4-23. The 3621 cm⁻¹ peak of raw MMT which is -OH stretching belongs to the hydrated structure of clay. A -NH₂ stretching peak is at 3421 cm⁻¹. Moreover, C-C stretching can be indicated at 1510 cm⁻¹ and 1311 cm⁻¹. The peaks at 1627 cm⁻¹ and 1264 cm⁻¹ represent -NH₂ scissoring and C-NH₂ stretching respectively [29]. The FTIR results showed that the ion exchange method was successful since the PPD has been linked to MMT through amine group protonation.

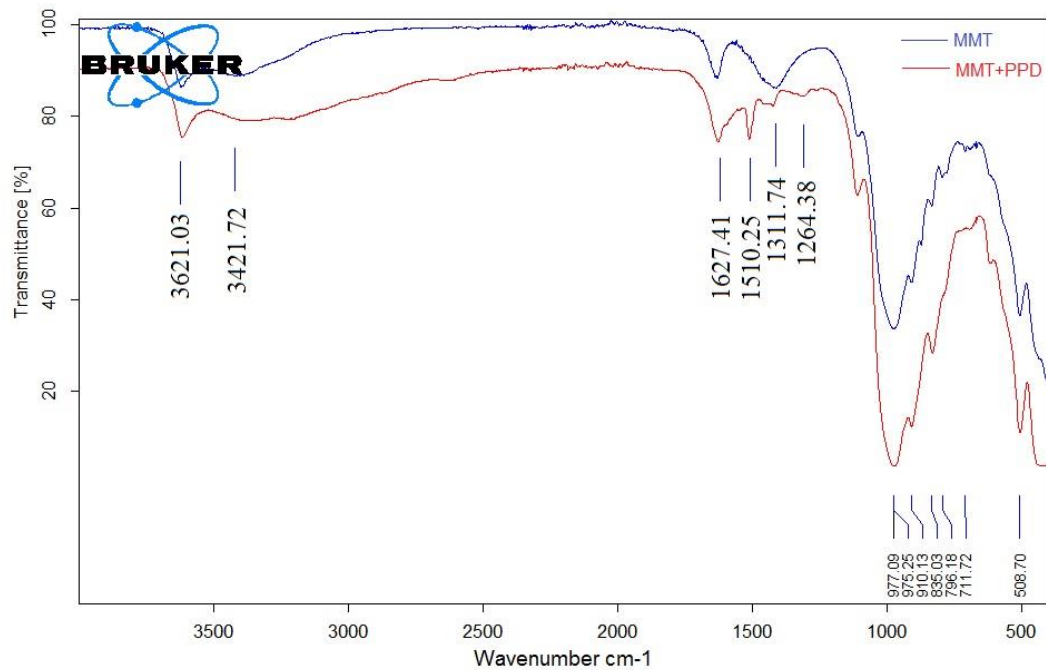


Figure 4-23. FTIR spectrums for MMT and PPD modified MMT.

4.4.3 Theoretical study of epoxy resin

The reaction occurring between epoxy resin and its hardener is an exothermal reaction which can release heat upon mixing. The reaction rate in the solid state can be written as

$$\frac{d\alpha}{dt} = Ae^{-E/RT} f(\alpha) \quad (4-15)$$

where α is the reaction rate, A is the pre-exponential factor of the Arrhenius equation, E is the activation energy, R is the universal gas constant which is 8.314 J·mol⁻¹·K⁻¹, T is the absolute temperature, and $f(\alpha)$ is the reaction kinetic model [30].

The Kissinger method [31] was used with a constant heating rate. When the maximum reaction rate happens, the Kissinger model could be applied in the system. It is written as:

$$\ln \frac{\beta_m}{T_m^2} = \ln \frac{AR}{E} f'(a_m) - \frac{E}{RT_m} \quad (4-16)$$

where the β_m is the heating rate, T_m is the temperature at the point where the maximum reaction rate happens. In the case of the first order reaction, $f'(\alpha) = 1$, then the equation can be indicated as,

$$\ln \frac{\beta_m}{T_m^2} = \ln \frac{AR}{E} - \frac{E}{RT_m} \quad (4-17)$$

Based on previous research [32-35], higher temperatures may increase the rate of epoxy resin cure reaction within the working temperature of epoxy resin. In contrast, lower temperatures could postpone the reaction time. However, cure at lower temperature with a slower rate could affect the physical properties of the resulting resins. In this case, FTIR was carried out to analyse the influence of low-temperature storage of the curing system.

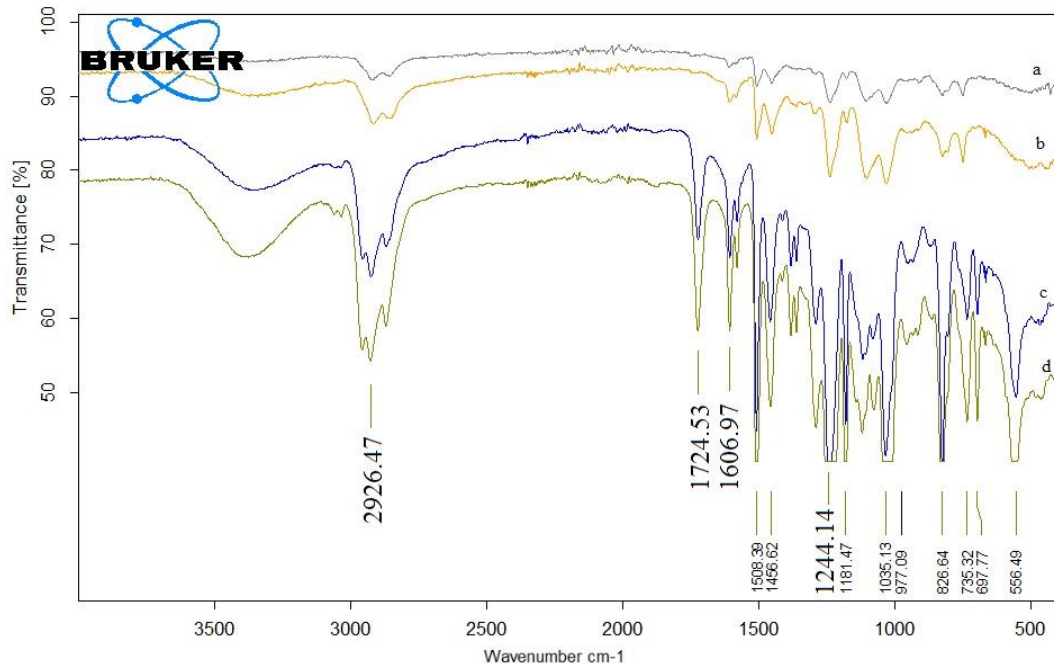


Figure 4-24. FTIR spectra for two resins: RX672H and RX900D cured with different procedures. (a) RX900D cured after keeping at a low temperature for 72 hr, (b) RX900D cured directly at room temperature, (c) RX672H cured directly at the room temperature, (d) RX672H cured after keeping at a low temperature for 72 hr.

*Room temperature was given as $20 \pm 5^\circ\text{C}$.

As it can be seen from Figure 4-24, the absorbance peak at 3400 cm^{-1} may be the O-H stretching. The peak which is about 2926 cm^{-1} illustrates a C-H stretching. The peak at 1724 cm^{-1} and 1606 cm^{-1} indicated the Ar-C=C-H stretching of RX672H resin. A strong peak at 1244 cm^{-1} could be indicated Ar-O- stretching. In terms of RX900D, and the absence of, or weak peaks at 3055 cm^{-1} and 915 cm^{-1} may be caused by the opening of epoxy rings.

It is obvious that there was no significant difference between direct curing at room temperature and curing after a low-temperature storage in refrigerator. In other words, both epoxy resins would probably not be affected by the cooling procedure during resin curing.

4.4.4 Analysis of MMT/resin composite

The potential for intercalation of clay and resin mixture has been proved in Section 4.4.1. Nanofil116 and BH natural are similar MMT clays. Moreover, laponite is an artificial clay based on the MMT structure. In this case, Nanofil116 MMT preformed film was chosen to prepare clay/resin composites by a vacuum impregnation process.

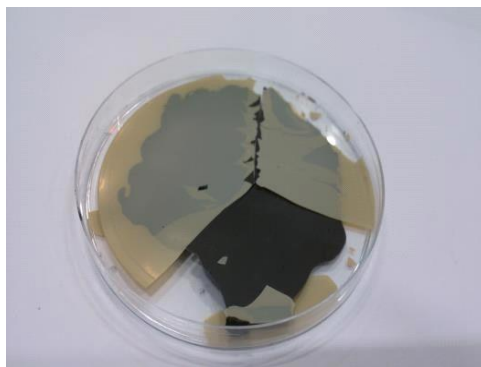


Figure 4-25. Image of MMT/resin composite sample.

The Figure 4-25 shows weak connections between resin and clay interfaces. In this kind of situation, XRD and FTIR were carried out on both side of the composite to investigate whether epoxy resin penetrated the interlayers of MMT or not.

Calculated basal spacing is given in Table 4-10. It indicates that the basal spacing of

all MMT/resin composites showed an increase. The temperature showed no effect on the change of interlayer spacing, even though, a lower temperature means a lower reaction rate, leading to a longer time of curing according to the kinetics of epoxy resins in Equation 4-16.

The increase of basal spacing in all the PPD treated MMT was larger than any of the untreated clays due to the epoxyphilic character after the ion exchange process.

Table 4-10. XRD results of two theta and changes in basal spacing.

Sample	$2\theta / ^\circ$	d_{001} spacing / Å	Increase in d_{001} / Å
MMT	7.05	12.528	-
MMT + 672H+LT	5.95	14.842	2.314
MMT + 900D+LT	6.15	14.359	1.831
MMT + 672H+RT	6.15	14.359	1.831
MMT + 900D+RT	6.25	14.130	1.602
PPD- MMT + 672H+LT	5.25	16.819	4.291
PPD- MMT + 900D+LT	5.65	15.629	3.101
PPD- MMT + 672H+RT	5.25	16.819	4.291
PPD- MMT + 900D+RT	5.25	16.819	4.291

*RT-sample cured at room temperature;

**LT-sample cured after a 72 hr refrigerator storage.

Based on Section 4.4.3, the peaks such as C-H stretching and Ar-O- stretching from epoxy resin should be found in the FTIR spectrum of the composites if the resin infiltrated into clay.

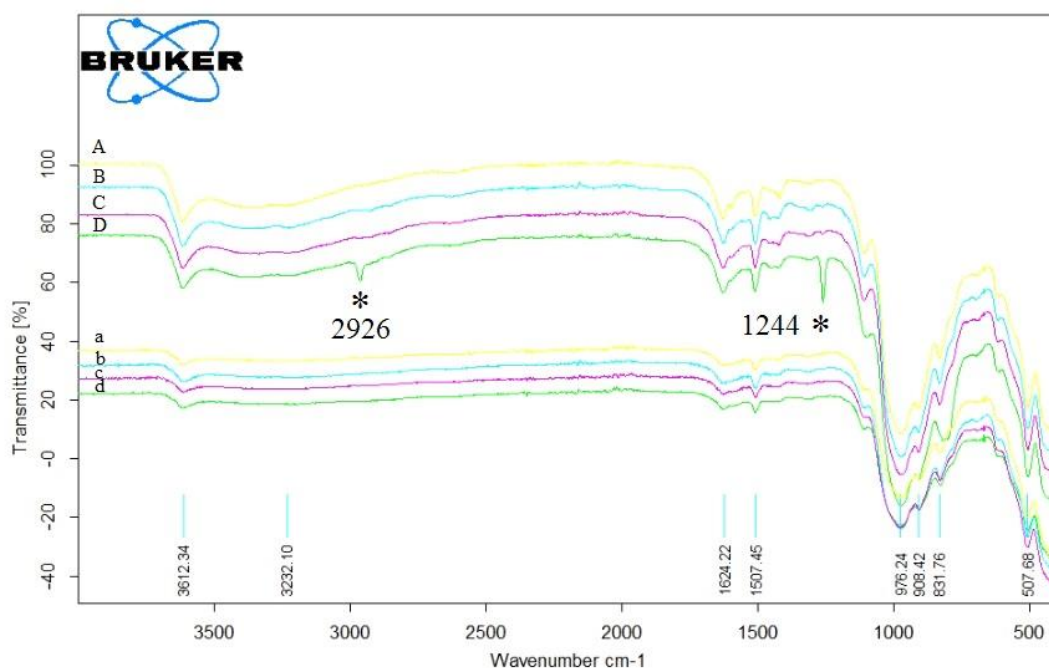


Figure 4-26. FTIR spectra for the top surface of clay discs (A) PPD-MMT 672H-RT*, (B) PPD-MMT 672H-LT*, (C) PPD-MMT-900D-RT, (D) PPD-MMT-900D-LT, the bottom surface of clay discs (a) PPD-MMT-672H-RT, (b) PPD-MMT-672H-LT, (c) PPD-MMT-900D-RT, (d) PPD-MMT-900D-LT.

*samples were given as PPD modified MMT mix with 672H resin cured in room temperature;

**samples were given as PPD modified MMT mix with 672H resin cured in room temperature after a 72 hr storage in refrigerator.

In terms of the top surface FTIR, as seen in Figure 4-26 (D) specific peaks (2926 cm^{-1} and 1244 cm^{-1}) of epoxy resins were found in the corresponding regions, confirming the infiltration of epoxy resins. In contrast, as to the bottom, no corresponding peaks were detected, it could be regarded that there was no penetration of epoxy resins to the base of the clay films.

The effect of cryogenic treatment was also investigated by FTIR. In theory, a lower temperature would allow resin to cure in a longer time, which may have a positive effect on penetration because it allows a longer time for liquid resin to flow into fine pores. Compared to curves C and D in Figure 4-26, it can be concluded that the resin 900D penetrated in MMT probably due to the longer penetration time at low temperature in the refrigerator.

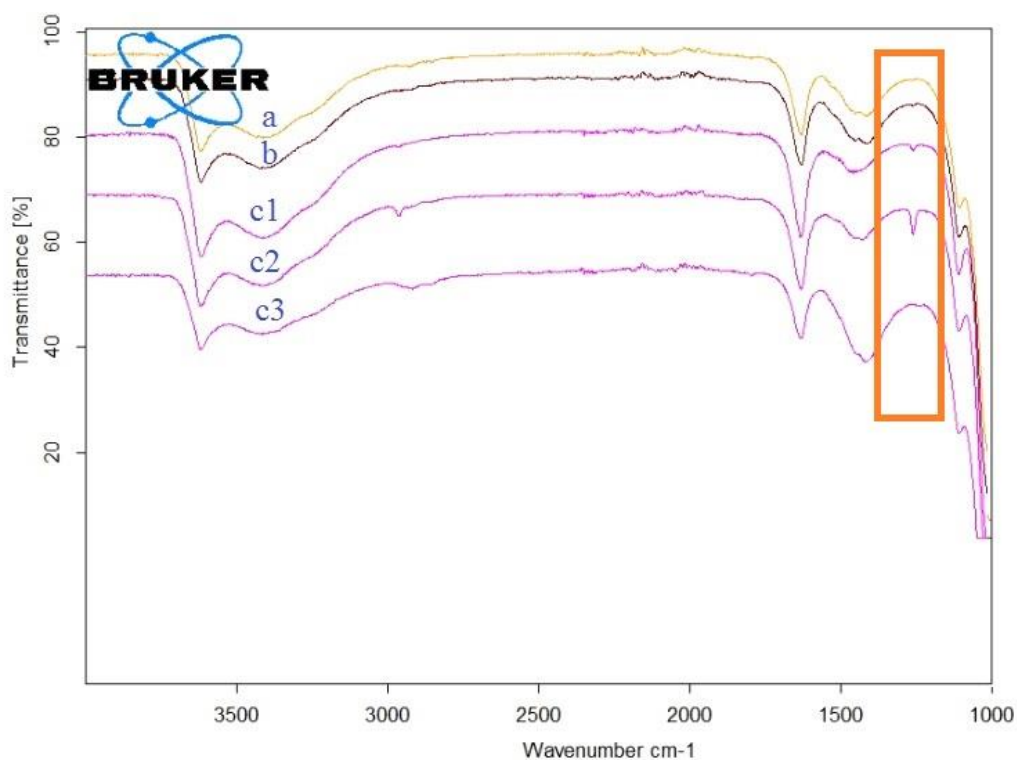
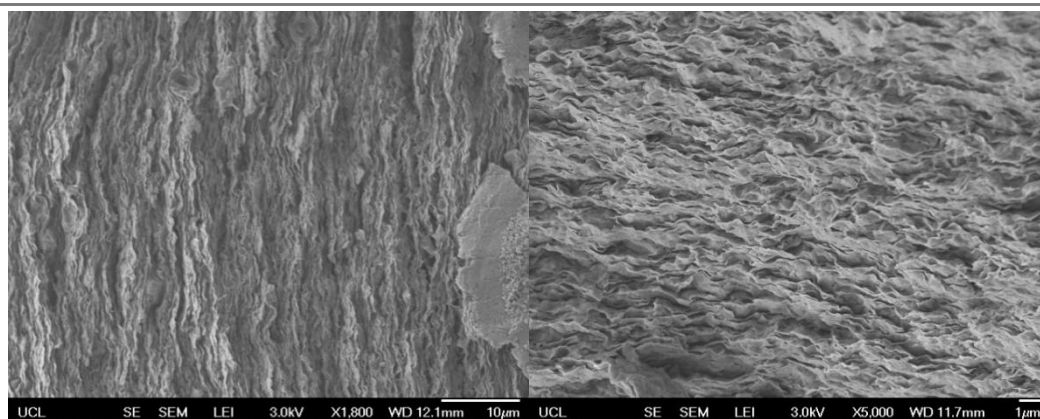


Figure 4-27. FTIR spectra for the top surface of MMT (a) MMT-672H-RT, (b) MMT-672H-LT, (c1) MMT-900D-RT, (c2) MMT-900D-LT, (c3) MMT-900D-LT120.*

*sample cured at room temperature after a 120 hr storage in refrigerator.

For an extension time sample LT120, it indicated that the extension time did not promote the penetration of epoxy resin.

Base on the analysis of XRD and FTIR, the sample with most potential for infiltration of clay samples are MMT/900D resin and PPD modified MMT/900D sample treated by cryogenic storage.



(a)

(b)

Figure 4-28. SEM of MMT/resin composite (a) MMT-900D after cryogenic treatment, (b) PPD modified MMT-900D after cryogenic treatment.

SEM was undertaken to analyse the cross sections of MMT/900D and PPD modified MMT/900D samples. Epoxy resin was barely seen in the spaces between clay platelets of both samples. Compared with the solution casting method, vacuum impregnation process has a quite short penetration time for polymers.

Even though a 120 hours refrigerator storage process was followed by vacuum impregnation, the situation seems no better. The reason for this phenomenon was due to the high viscosity of resin. After putting resin into refrigerator, the mixture of resin turned into a viscous gel in several hours. The viscosity could become the barrier for penetration. Furthermore, a low permeable layered system was built by the high aspect ratio and ordered structure of MMT. To be specific, a high aspect ratio can increase the path of fluid resulting in an undesirable diffusion system. Finally, because of the presence of phenol or bisphenol structure, the steric hindrance of resin is quite large which could inhibit the penetration process. Thus once again it is seen that the ordered structure, which is indicated as a nacre-like microstructure for mechanical properties, provides an obstruction to resin infiltration.

Therefore, poor mechanical properties were predicted because very little resin penetrated into the clay. The interaction between layers would be weak. The tensile strength of MMT/900D was 28.9 MPa and PPD-MMT/900D was 22.6 MPa while the data from supplier of resin shows, RX900D cured resin gives tensile strength 85 MPa. It could be suggested that epoxy resin was not suitable for Nano116 clay to

form a strong nanocomposite. However, it is possible that a low viscosity or a long working life resin could penetrate among kaolinite plates, which are much coarser, to create a traditional composite instead of trying to penetrate resin into galleries of MMT to form a nanocomposite. In order to make MMT nanocomposite by vacuum impregnation process, low M_w monomer was suggested. The monomer should be small and flat (contain aromatic rings), for instance, methyl methacrylate.

4.5 MMA polymerisation mechanism

Poly (methyl methacrylate) or PMMA is an amorphous polymer developed in the form of transparent sheet in 1932 by Rohm and Bauer [36]. Generally, atactic PMMA can be identified as a plastic with 92 % transparency, high impact strength and low density [37, 38]. It is polymerised from methyl methacrylate (MMA), which is an ester of methacrylic acid. Polymerisation starts at the carbon double bond of MMA to form a linked chain with other monomers. The glass transition temperature of atactic PMMA is 105 °C [37].

In terms of mechanical properties, PMMA has a tensile strength of 72 MPa, tensile modulus 3.10 GPa. After failure by tensile loads, it shows a 5 % elongation [38]. PMMA also has good processing properties as well as thermoforming [39]. Therefore, it is widely used in both industry and biomedical applications.

Various polymerisation mechanisms could be used for MMA conversion to PMMA. Among these mechanisms, free radical polymerisation is the most widely used technique [39]. The free radical process can take place in bulk or solution where it is homogeneous, or even in suspension and emulsion where it is heterogeneous [39]. Compared with other methods, free radical polymerisation can occur under a relative simple condition, so it is commercially used in industry on a large scale [40]. During the polymerisation of MMA, there should be a low oxygen partial presence since oxygen may act as a radical inhibitor, which can terminate the free radical polymerisation [36, 41].

Free radical polymerisation can be promoted by thermally labile compounds, such as

benzoyl peroxide (BPO) and 2,2'-azobisisobutyronitrile (AIBN). During heating, the labile compound can be decomposed and form free radicals which can react with the molecules of MMA, shown in Figure 4-29. The reaction could open the pi-bond of MMA and form a reactive centre [39]. When other molecules contact the reactive centre, the reaction occurs resulting in propagating of the PMMA chain. MMA monomer has a low viscosity which makes it a desirable candidate to mimic nacre via impregnation process.

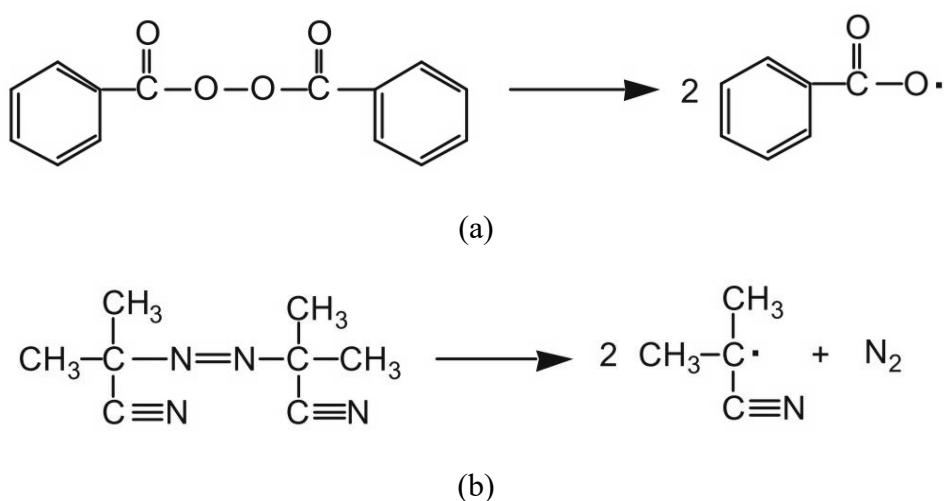


Figure 4-29. The initiators decomposition to form free radicals (a) BPO, (b) AIBN.

After the initiator has decomposed, the original concentration of initiator decreases. The time is represented by the initiator half-life when the concentration of initiator becomes half of its original.

The equation for half-life of initiator can be deduced as below:

In the first order reaction, the rate of reaction r can be given as,

$$\frac{-dc}{dt} = r = kc \quad (4-18)$$

where c is the concentration of reactant, t is the reaction time and k is the reaction rate coefficient.

$$C_{(t)} = C_{(0)} e^{-kt} \quad (4-19)$$

where $C_{(0)}$ is the original concentration of reactant. When $C_{(t)} = 0.5 C_{(0)}$, the time t is

$$t = \frac{\ln 2}{k} \quad (4-20)$$

The reaction rate coefficient is dependent on temperature. The BPO and AIBN supplier Sigma Aldrich have provided the reaction rate coefficient k of BPO as $2.0 \times 10^{-6} \text{ s}^{-1}$ at 60 °C, $2.3 \times 10^{-5} \text{ s}^{-1}$ at 78 °C and $5.0 \times 10^{-4} \text{ s}^{-1}$ at 100 °C. The reaction rate coefficient k of AIBN is given as $2.2 \times 10^{-6} \text{ s}^{-1}$ at 50 °C, $3.2 \times 10^{-5} \text{ s}^{-1}$ at 70 °C and $1.5 \times 10^{-3} \text{ s}^{-1}$ at 100 °C. Thus the half-life of the initiator with a given temperature can be calculated by equation (4-20).

A series of experiments was carried out to prove the potential of MMA using thermally initiated polymerisation. 1 wt. % and 4 wt. % BPO were added to stabilised MMA which contains no more than 30 ppm 4-methoxyphenol (MEHQ) as inhibitor. The procedures were shown in Section 3.4 while the results are given in Table 4-11. The weight loss of MMA is calculated from the weight before heating and after heating (excluding the mass of clay/alumina particles). If the MMA fully polymerised, there would be no weight difference before and after polymerisation of MMA. In other words, the weight loss then was a symbol of unpolymerised MMA.

Table 4-11. Thermal polymerisation of stabilised MMA with 1 wt. % and 4 wt. % BPO.

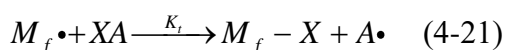
Sample	Before heating/ g	After heating/ g	Weight loss wt. %
1 BPO MMA	1.23	0.69	43.9
1 BPO MMA	1.27	0.70	44.9
1 BPO MMA	1.08	0.34	68.5
4 BPO MMA	1.31	0.88	32.8
4 BPO MMA	1.01	0.77	23.8
4 BPO MMA	1.37	1.14	16.8

*Number 1 means 1 wt. % BPO and 4 means 4 wt. % BPO added in MMA.

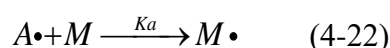
It can be concluded from the weight loss in Table 4-11, the thermal polymerisation can be promoted by increasing the concentration of initiator since the weight loss of 4 wt. % BPO samples decreased. The weight loss of these samples (1 wt. % BPO/ MMA mixture) is all higher than 40 wt. % due to the presence of MEHQ, which is a retarder of MMA.

To understand the mechanism of polymerisation inhibition, chain transfer should be

introduced first. Chain transfer can be regarded as the termination of the growing polymer since it can transfer a hydrogen or atoms to the growing chain to terminate the free radical of the polymer [39]. However, it can be treated as an initiation of another polymer because it generates a new free radical after donating its hydrogen or other atom to the previous radical. This radical exchange reaction is called chain transfer reaction [39] which is shown below,



where the XA is the chain transfer reactant, X is the transferred atom or species and k_t is the transfer rate constant. The new free radical can initiate the free polymerisation, the new free radical reaction being described as,



where k_a is the rate of the new free radical polymerisation. This reaction can lower the molecular weight of the previous polymer resulting from terminating the carbon chain propagation.

If k_a is roughly the same as the previous propagation rate k_p , in the meanwhile, $k_p \gg k_t$, it can be considered as a normal chain transfer but with a lower M_w polymer obtained. If $k_a \approx k_p \ll k_t$, the M_w of polymer resultant would be decreased dramatically and the polymer turns to be telomers [40]. As the new rate and original rate are roughly the same, the overall rate of polymerisation is constant [40].

If the new free radical polymerisation rate k_a is slower than the previous rate k_p , it shows a decrease both in molecular weight of polymer and rate of polymerisation. When $k_p \gg k_t$, this situation is known as retardation. If $k_p \ll k_t$, then it shows a significant decrease both in molecular weight of polymer and the rate of polymerisation, this effect is called degradative chain transfer [38, 39, 41]. In this case, the chain transfer reactant is defined as an inhibitor.

An inhibitor can react with free radicals to form a kind of radical which can only react with itself or react with other radicals, generating barely reactive products. In terms of MEHQ, the phenol group can act as a hydrogen donator which is shown in Figure 4-30. Moreover, the phenol group could cooperate with oxygen to inhibit chain propagation.

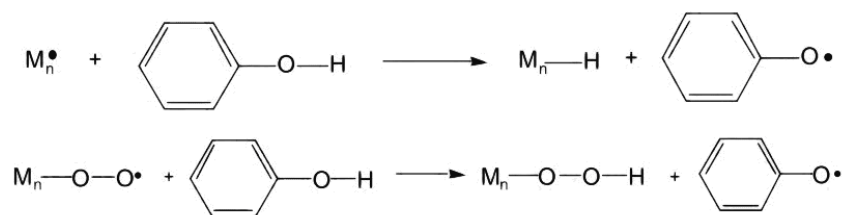


Figure 4-30. Mechanism of inhibition by phenol. [38]

In order to analyse the potential of MMA in-situ polymerisation after infiltration or vacuum impregnation, three kinds of powder were added into a 4 wt. % BPO/MMA mixture. Alumina sample was used here to prove the feasibility of the ice-templated method by Lawrence National laboratory which made use of alumina in conjunction with PMMA [43] and because aluminium in the clay structure has been held responsible for inhibition of polymerisation of acrylic polymers. The results are shown in Table 4-12, 4-13, 4-14.

Table 4-12. MMA with 4 wt. % BPO mixed with Al₂O₃.

Weight ratio (MMA: Al ₂ O ₃)	Before heating/ g	After heating/ g	Weight loss wt. %
1:0.5	1	1	0
1:1	1	0.98	2
1:1.5	1	0.77	23

Table 4-13. MMA with 4 wt. % BPO mixed with MMT.

Weight ratio (MMA: MMT)	Before heating/ g	After heating/ g	Weight loss wt. %
1:0.5	1	0.73	27
1:1	1	0.93	7
1:1.5	1	0.88	12

Table 4-14. MMA with 4 wt. % BPO mixed with laponite.

Weight ratio (MMA:Laponite)	Before heating/ g	After heating/ g	Weight loss wt. %
1:0.5	1.22	0.97	20.49
1:1	1.23	1.05	14.63
1:1.5	1.22	0.79	35.25

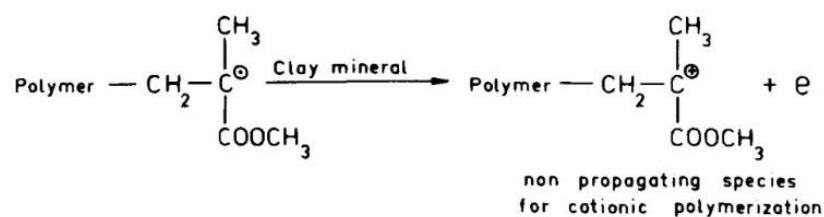
The weight losses of these samples are not higher than the 4 wt. % BPO + MMA and could be caused by the nitrogen flow before polymerisation. It is worth noting that after polymerisation, the laponite sample and alumina sample formed a white solid while the MMT sample was found to be a yellow rubbery polymer-clay mixture that gave a strong MMA smell after opening the aluminium reactor.

This indicates that the MMT inhibits the polymerisation of MMA since a low molecular weight polymer was obtained and unpolymerised MMA was evident from the strong smell. Other researchers [44-46] have suggested that the aluminium which is located at the edge of the silicate layers plays an important role in the polymerisation of MMA. When methyl methacrylate monomers are heated with clay minerals, the aluminium at clay edges can adsorb the monomer. Then, the unexpected orientation of the adsorbed monomer inhibits the electron-transfer reactions. Moreover, methyl methacrylate is not susceptible to cationic polymerisation [45]. The clay minerals contain Lewis acids, defined as electron pair acceptors, for instance, Fe^{3+} in MMT shown in Equation 4-23.



Two mechanisms by Lewis acids could inhibit free radical reactions shown in Figure 4-31. A prior adsorption of the free radical by Lewis acids could terminate the polymer chain growing by combination or disproportionation.

1. Electron transfer with formation of non propagating intermediate.



2. Increased rate of termination.

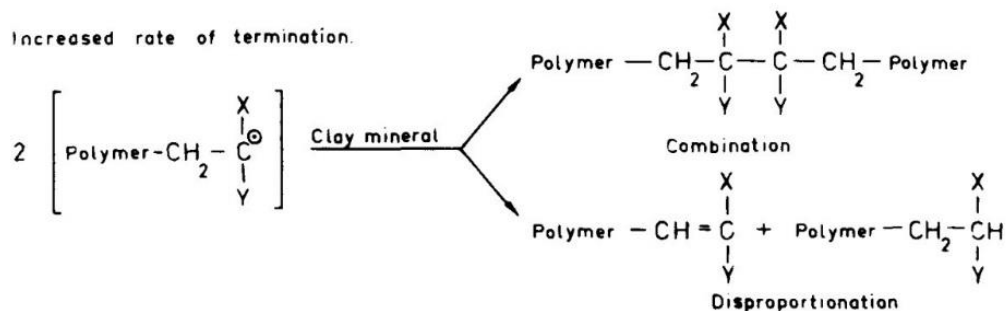


Figure 4-31. Mechanism for inhibition of free radical reaction by clay mineral. [46]

Since MMT acts as an inhibitor during chain growth, it was not considered further in thermally initiated polymerisation of MMA experiments. In terms of laponite, which does not show the inhibition behaviour, may be caused by the absence of aluminium of its structure. However, alumina did not inhibit the polymerisation as well. This can be explained as the bonding formed in alumina is much stronger than that in the silicates layers, giving a less possibility of free aluminium forming at edges which can inhibit the polymerisation of MMA.

References

- [1] Kurose T, Yudin VE, Otaigbe JU, Svetlichnyi VM. Compatibilized polyimide (R-BAPS)/BAPS-modified clay nanocomposites with improved dispersion and properties. *Polymer*. 2007 Nov 16;48(24):7130-8.
- [2] Walley P, Zhang Y, Evans JR. Self-assembly of montmorillonite platelets during drying. *Bioinspiration & Biomimetics*. 2012 Jul 27;7(4):046004.
- [3] Walther A, Bjurhager I, Malho JM, Pere J, Ruokolainen J, Berglund LA, Ikkala O. Large-area, lightweight and thick biomimetic composites with superior material properties via fast, economic, and green pathways. *Nano Letters*. 2010 Mar 10;10(8):2742-8.
- [4] Yao HB, Tan ZH, Fang HY, Yu SH. Artificial nacr-like bionanocomposite films from the self-assembly of chitosan-montmorillonite hybrid building blocks. *Angewandte Chemie International Edition*. 2010 Dec 27;49(52):10127-31.
- [5] Barthelat F. Nacre from mollusk shells: a model for high-performance structural materials. *Bioinspiration & Biomimetics*. 2010 Aug 20;5(3):035001.
- [6] Podsiadlo P, Kaushik AK, Arruda EM, Waas AM, Shim BS, Xu J, Nandivada H, Pumphlin BG, Lahann J, Ramamoorthy A, Kotov NA. Ultrastrong and stiff layered polymer nanocomposites. *Science*. 2007 Oct 5;318(5847):80-3.
- [7] Wang J, Cheng Q, Lin L, Chen L, Jiang L. Understanding the relationship of performance with nanofiller content in the biomimetic layered nanocomposites. *Nanoscale*. 2013;5(14):6356-62.
- [8] Smith J, Medar P, MR IA. Finite element analysis and fatigue life estimation of plate with different stress levels. *International Journal of Advanced Research and Innovation*. 2014;2(3):613-7.
- [9] Enventure. Stress concentration factor, an important parameter for the safety of any component. 9 July 2015. [Accessed 8 August 2015]; Available from: <http://www.enventure.com/blog/stress-concentration-factor-an-important-parameter-for-the-safety-of-any-component/>.
- [10] Das P, Malho JM, Rahimi K, Schacher FH, Wang B, Demco DE, Walther A. Nacre-mimetics with synthetic nanoclays up to ultrahigh aspect ratios. *Nature Communications*. 2015 Jan 20;6.
- [11] Chen B, Evans JR, Greenwell HC, Boulet P, Coveney PV, Bowden AA, Whiting A. A critical appraisal of polymer–clay nanocomposites. *Chemical Society Reviews*.

2008;37(3):568-94.

- [12] Bourbigot S, Gilman JW, Wilkie CA. Kinetic analysis of the thermal degradation of polystyrene–montmorillonite nanocomposite. *Polymer Degradation and Stability*. 2004 Jun 30;84(3):483-92.
- [13] Ray SS, Okamoto M. Polymer/layered silicate nanocomposites: a review from preparation to processing. *Progress in Polymer Science*. 2003 Nov 30;28(11):1539-641.
- [14] Peppas NA, Hansen PJ. Crystallization kinetics of poly (vinyl alcohol). *Journal of Applied Polymer Science*. 1982 Dec 1;27(12):4787-97.
- [15] Cerezo FT, Preston CM, Shanks RA. Morphology, Thermal Stability, and Mechanical Behavior of [Poly (propylene)-grafted Maleic Anhydride]-Layered Expanded Graphite Oxide Composites. *Macromolecular Materials and Engineering*. 2007 Feb 2;292(2):155-68.
- [16] Su J, Wang Q, Su R, Wang K, Zhang Q, Fu Q. Enhanced compatibilization and orientation of polyvinyl alcohol/gelatin composite fibers using carbon nanotubes. *Journal of Applied Polymer Science*. 2008 Mar 15;107(6):4070-5.
- [17] Padawer GE, Beecher N. On the strength and stiffness of planar reinforced plastic resins. *Polymer Engineering & Science*. 1970 May 1;10(3):185-92.
- [18] Yamaura K, Tada M, Tanigami T, Matsuzawa S. Mechanical properties of films of poly (vinyl alcohol) derived from vinyl trifluoroacetate. *Journal of Applied Polymer Science*. 1986 Feb 5;31(2):493-500.
- [19] Manevitch OL, Rutledge GC. Elastic properties of a single lamella of montmorillonite by molecular dynamics simulation. *The Journal of Physical Chemistry B*. 2004 Jan 29;108(4):1428-35.
- [20] Chen B, Evans JR. Elastic moduli of clay platelets. *Scripta materialia*. 2006 May 31;54(9):1581-5.
- [21] Fromageau J, Brusseau E, Vray D, Gimenez G, Delachartre P. Characterization of PVA cryogel for intravascular ultrasound elasticity imaging. *IEEE transactions on ultrasonics, ferroelectrics, and frequency control*. 2003 Oct;50(10):1318-24.
- [22] Patro TU, Wagner HD. Layer-by-layer assembled PVA/Laponite multilayer free-standing films and their mechanical and thermal properties. *Nanotechnology*. 2011 Oct 21;22(45):455706.
- [23] Zhang X, Liu T, Sreekumar TV, Kumar S, Moore VC, Hauge RH, Smalley RE. Poly (vinyl alcohol)/SWNT composite film. *Nano Letters*. 2003 Sep 10;3(9):1285-8.

-
- [24] Strawhecker KE, Manias E. Structure and properties of poly (vinyl alcohol)/Na⁺ montmorillonite nanocomposites. *Chemistry of Materials*. 2000 Oct 16;12(10):2943-9.
- [25] Naito K, Yang J M, Kagawa Y. Tensile properties of high strength polyacrylonitrile (PAN)-based and high modulus pitch-based hybrid carbon fibers-reinforced epoxy matrix composite. *Journal of Materials Science*, 2012, 47(6):2743-2751.
- [26] Hou GX, Chen XA, Sang XM. Morphologies and Mechanical Properties of Epoxy Resin/Polymethyl Methacrylate Interpenetrating Network Modified with Kaolin. In *Advanced Materials Research 2011* (Vol. 337, pp. 184-187). Trans Tech Publications.
- [27] Wang MS, Pinnavaia TJ. Clay-polymer nanocomposites formed from acidic derivatives of montmorillonite and an epoxy resin. *Chemistry of Materials*. 1994 Apr;6(4):468-74.
- [28] Jiankun L, Yucai K, Zongneng Q, Xiao-Su Y. Study on intercalation and exfoliation behavior of organoclays in epoxy resin. *Journal of Polymer Science Part B: Polymer Physics*. 2001 Jan 1;39(1):115-20.
- [29] Spectral database for organic compounds. [Accessed 5 August 2016]; Available from: http://sdb.sdb.aist.go.jp/sdb/cgi-bin/cre_index.cgi
- [30] Criado JM, Perez-Maqueda LA. Sample controlled thermal analysis and kinetics. *Journal of Thermal Analysis and Calorimetry*. 2005 Mar 1;80(1):27-33.
- [31] Kissinger HE. Reaction kinetics in differential thermal analysis. *Analytical Chemistry*. 1957 Nov;29(11):1702-6.
- [32] Roşu D, Caşcaval CN, Mustată F, Ciobanu C. Cure kinetics of epoxy resins studied by non-isothermal DSC data. *Thermochimica Acta*. 2002 Feb 7;383(1):119-27.
- [33] Roşu D, Mititelu A, Caşcaval CN. Cure kinetics of a liquid-crystalline epoxy resin studied by non-isothermal data. *Polymer Testing*. 2004 Apr 30;23(2):209-15.
- [34] Catalani A, Bonicelli MG. Kinetics of the curing reaction of a diglycidyl ether of bisphenol A with a modified polyamine. *Thermochimica Acta*. 2005 Nov 1;438(1):126-9.
- [35] Thomas R, Durix S, Sinturel C, Omonov T, Goossens S, Groeninckx G, Moldenaers P, Thomas S. Cure kinetics, morphology and miscibility of modified DGEBA-based epoxy resin-effects of a liquid rubber inclusion. *Polymer*. 2007 Mar

8;48(6):1695-710.

- [36] Stickler M, Rhein T. Polymethacrylates, Ullmann's Encyclopedia of Industrial Chemistry. 5th ed. New York:1992. A21, p. 473.
- [37] Brydson JA. Plastics Materials, 7th edn; Butterworth-Heinemann: Oxford, 1999; 398-424.
- [38] Ali U, Karim KJ, Buang NA. A review of the properties and applications of poly (methyl methacrylate)(PMMA). Polymer Reviews. 2015 Oct 2;55(4):678-705.
- [39] Rasmussen WL. Novel carbazole based methacrylates, acrylates, and dimethacrylates to produce high refractive index polymers. Ph.D. Thesis, Virginia Polytechnic Institute and State University, Blacksburg, VA, 2001. p. 60.
- [40] Odian G. Principles of Polymerisation, 4th ed; John Wiley & Sons: New Jersey, p. 198-286.
- [41] Kine BB; Novak, R.W., "Acrylic and Methacrylic Ester Polymers" in Encyclopedia of Polymer Science and Engineering, Wiley: New York, 1985. p. 262.
- [42] Flory PJ. Principles of Polymer Chemistry. Cornell University Press: Ithaca, 1953, p. 161-174.
- [43] Munch E, Launey ME, Alsem DH, Saiz E, Tomsia AP, Ritchie RO. Tough, bio-inspired hybrid materials. Science. 2008 Dec 5;322(5907):1516-20.
- [44] Solomon DH, Swift JD. Reactions catalyzed by minerals. Part II. Chain termination in free-radical polymerizations. Journal of Applied Polymer Science. 1967 Dec 1;11(12):2567-75.
- [45] Solomon DH. Clay minerals as electron acceptors and/or electron donors in organic reactions. Clays and Clay Minerals. 1968 Jan 1;16(31):31-39.
- [46] Solomon DH, Loft BC. Reactions catalyzed by minerals. Part III. The mechanism of spontaneous interlamellar polymerizations in aluminosilicates. Journal of Applied Polymer Science. 1968 May 1;12(5):1253-62.

Chapter 5

Laponite Based Clay/Polymer Nanocomposites

In this part of the work, laponite/polymer composites were prepared by two main methods: the self-drying method undertaken with laponite suspension and PVA solution, and in-situ photo polymerisation which was performed after introducing the monomer into self-assembled laponite film.

5.1 Analysis of laponite/PVA nanocomposite from solution casting

5.1.1 X-ray diffraction of laponite and its composite.

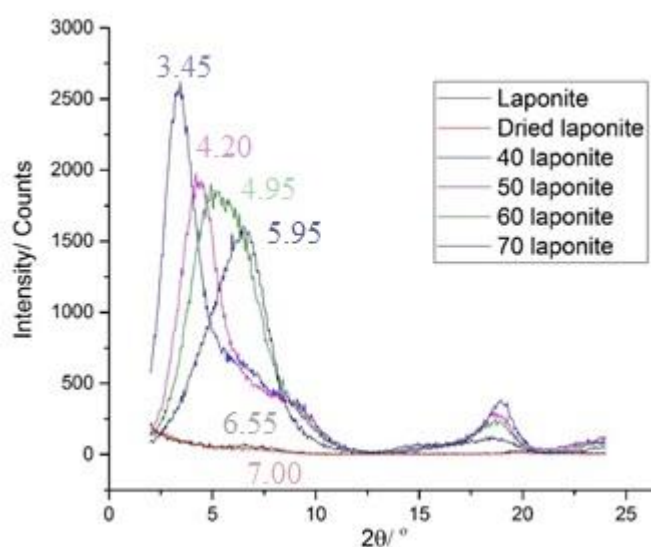


Figure 5-1. XRD traces for PVA composites and for as-received laponite. The samples are identified by wt. % of laponite.

Table 5-1. Results from XRD traces for PVA-laponite composites from Figure 5-1.

Clay sample/ wt. % laponite	$2\theta/^\circ$	Basal spacing/ \AA	Change spacing/ \AA
Laponite	6.55	13.48	-
Dried laponite	7.00	12.62	- 0.86
40	3.45	25.59	+ 12.11
50	4.20	21.02	+ 7.54
60	4.95	17.84	+ 4.36
70	5.95	14.84	+ 1.36

The initial basal spacing of laponite is 13.48 Å in agreement with Herrera [1]. It can be concluded that in all samples irrespective of volume fraction, PVA intercalated into laponite since the XRD results show increases in basal spacing. The basal spacing of 40 wt. % laponite/PVA composite (25.59 Å) is almost double than the original laponite (13.48 Å).

5.1.2 Fracture surface of laponite/PVA composites.

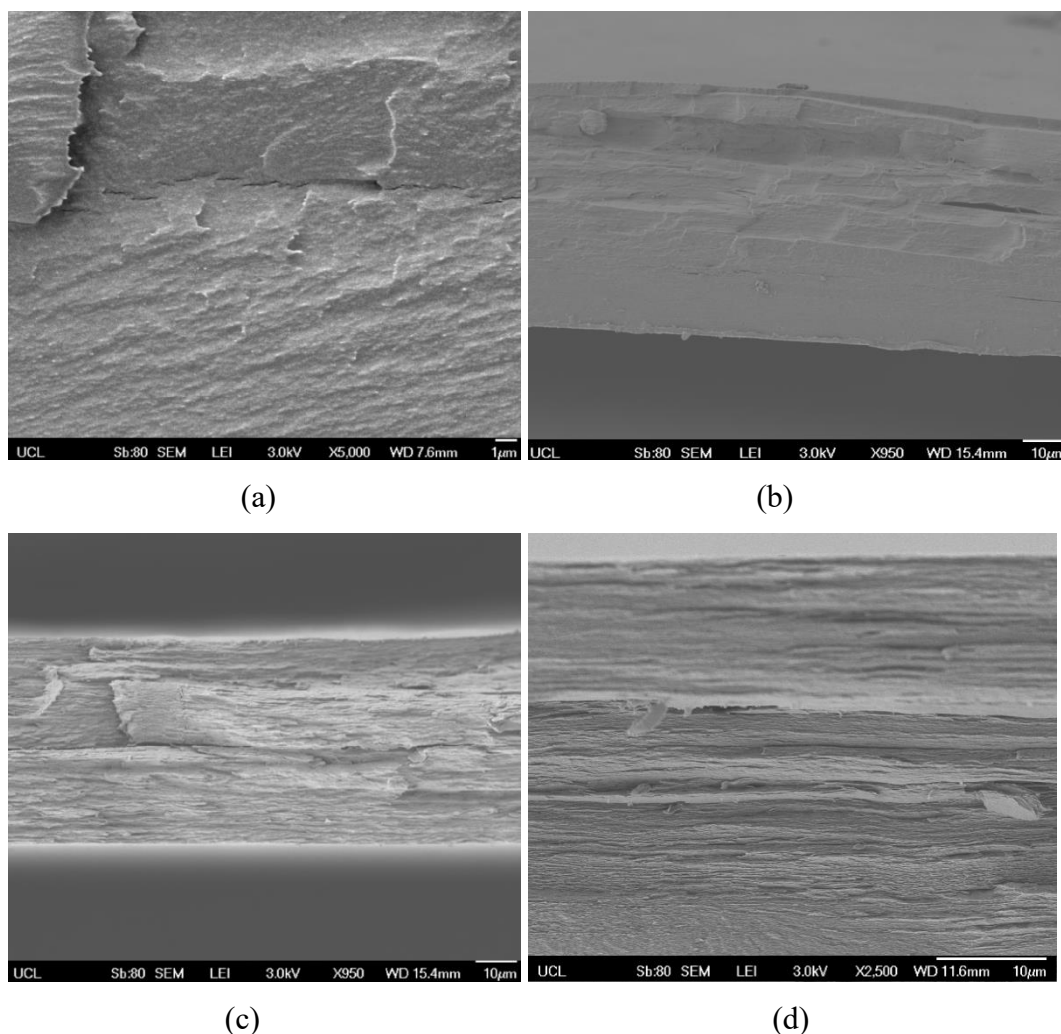


Figure 5-2. SEM of fracture surface of (a) 40wt. % laponite/PVA composites, (b) 50 wt. % laponite/PVA composites, (c) 60wt. % laponite/PVA composites, (d) 70 wt. % laponite/PVA composites.

The fracture surface of 40 wt. % laponite/PVA composite is fully covered by polymer, even under 5000× magnification, the layered structure was not observable

in the SEM. However, 60 wt. % and 70 wt. % laponite/PVA appear as intensive layered structure as can be seen from Figure 5-2.

Since the layered structure cannot be seen clearly in 40 wt. % and 50 wt. % laponite composites, 60wt. % laponite/PVA composite was chosen as an example to analyse the microstructure of ordered clay/polymer composites which is shown in Figure 5-3.

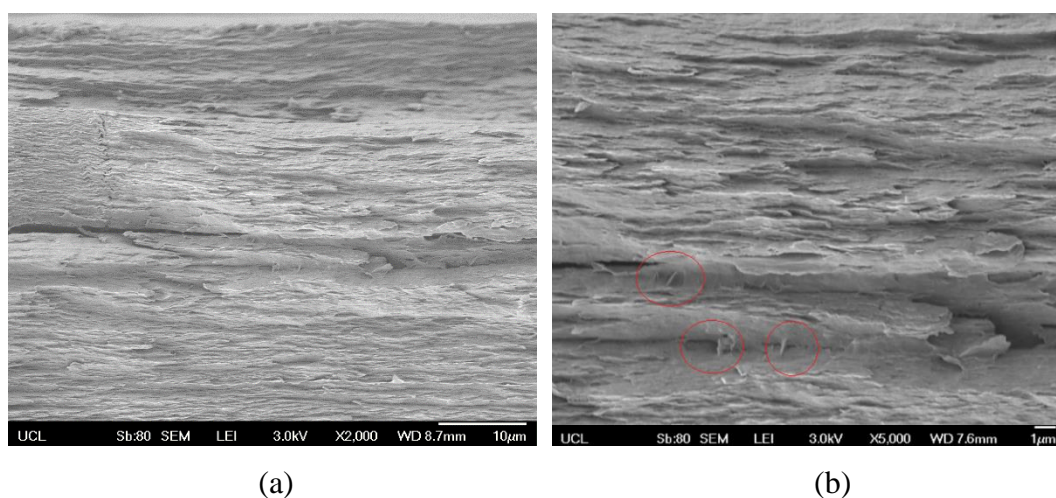


Figure 5-3. SEM of fracture surface of 60 wt. % laponite/PVA composite.

The layered structure was obtained by the solution casting method with interlayer polymer intercalated. The bridges between clay layers that can be seen from Figure 5-3 could be PVA which can act as glue in composites during interlayer sliding. The toughening mechanism accomplished by the plastic deformation can avoid stress concentrations and to some extent, it can inhibit the propagation of cracks.

5.1.3 UV-visible transmittance of laponite/PVA nanocomposite

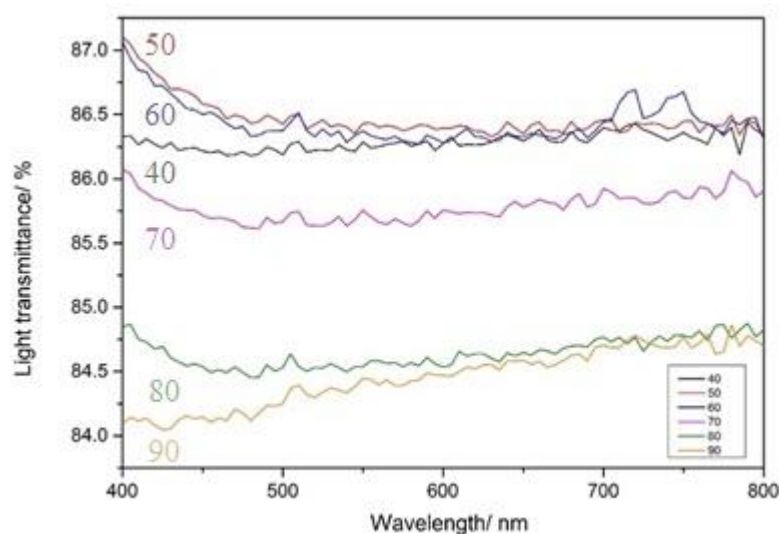


Figure 5-4. UV-visible transmittance of laponite/PVA nanocomposite. The samples were given as wt. % of laponite.

It is worth noting that laponite itself has interesting optical properties. Shikinada and co-workers [2] made 57 wt. % laponite nanocomposite with a 90 % transmittance in the 400-800 nm region. All of the laponite/PVA samples reported here had a transmittance above 80 %. According to the graph, Figure 5-4, high weight fraction composites have a higher absorbance coefficient in the visible wavelength region: 400-800 nm. As reported by Zhu [3], the intrinsic absorbance of separate clay sheets at 244 nm tends to extend to 600 nm due to the increasing content of Fe ions. With higher clay content, this effect would be more obvious. During the process of synthesising laponite, the exchangeable ions in MMT (Fe^{3+}) are replaced by Li^+ or Na^+ , resulting in the comparable transparency of laponite. Figure 5-5 shows the difference between preformed MMT and laponite film.

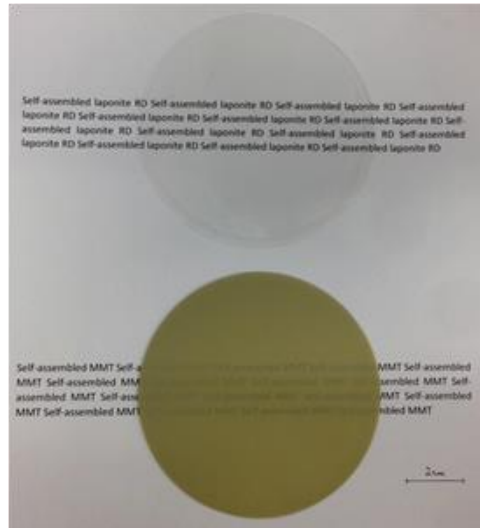


Figure 5-5. Compared MMT and laponite clay film (a) transparent laponite, (b) dark yellow MMT.

The example in Figure 5-6 was set to indicate the Beer-Lambert law. When a beam of light, perpendicular to the surface of the sample and defined as z axis, enters a material, as shown in Figure 5-6, the radiant flux of light is reduced by each part of the sample. The thickness of small parts is given as dz and all the infinitesimals are perpendicular the direction of light.

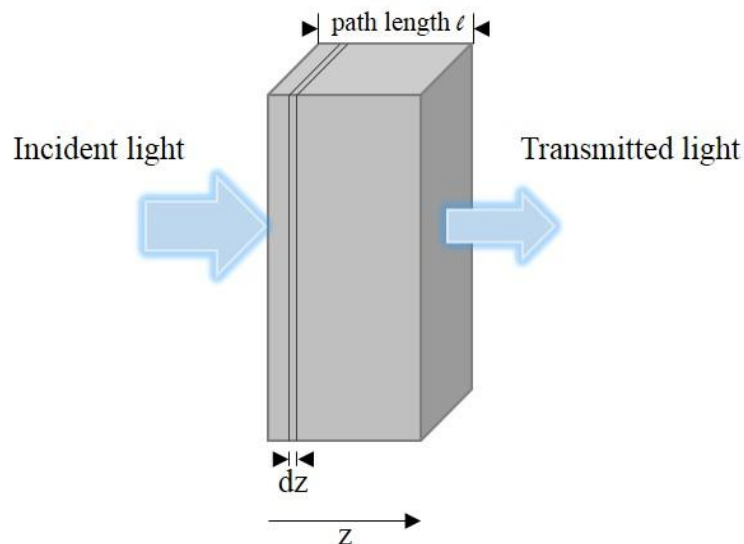


Figure 5-6. The illustration of Beer-Lambert law.

Due to the scattering and absorption of photons, the radiant flux is reduced gradually when passed through the sample. The function below is given to describe the

phenomenon, where μ is the attenuation coefficient, and $\Phi_e(z)$ is the radiant power of light.

$$\frac{d\Phi_e}{dz}(z) = -\mu(z)\Phi_e(z) \quad (5-1)$$

After multiplying the integrating factor $e^{\int_0^z \mu(z')dz'}$, (5-1) can be written as (5-2)

$$\frac{d\Phi_e}{dz}(z)e^{\int_0^z \mu(z')dz'} + \mu(z)\Phi_e(z)e^{\int_0^z \mu(z')dz'} = 0 \quad (5-2)$$

Because of the product rule, shown in (5-3)

$$\frac{d}{dx}(\mu \cdot \gamma) = \mu \cdot \frac{d\gamma}{dx} + \gamma \cdot \frac{d\mu}{dx} \quad (5-3)$$

equation (5-2) can be derived as

$$\frac{d}{dz}(\Phi_e(z)e^{\int_0^z \mu(z')dz'}) = 0 \quad (5-4)$$

Introducing the thickness of the sample or path length l , the power of incident light is given as $\Phi_e^i = \Phi_e(0)$, and the transmitted one is $\Phi_e^t = \Phi_e(l)$, and equation (5-4) can be written as

$$\Phi_e^t = \Phi_e^i e^{\int_0^l \mu(z)dz} \quad (5-5)$$

In terms of the definition of transmittance, it is the ratio of the power of transmitted light to the power of incident light. Then it can be concluded that

$$T = \frac{\Phi_e^t}{\Phi_e^i} e^{\int_0^l \mu(z)dz} \quad (5-6)$$

Absorbance is defined as the common logarithm of the ratio of power of incident light to the power when the light passes through the sample, so

$$A = \log_{10}\left(\frac{\Phi_e^i}{\Phi_e^t}\right) = -\log_{10} T \quad (5-7)$$

The attenuation cross section σ is given as below, where μ is the attenuation coefficient and n is the number density.

$$\sigma = \frac{\mu}{n} \quad (5-8)$$

The molar attenuation coefficient is written as (5-9), and amount concentration is indicated in (5-10). Where N_A , the Avogadro constant, equals $6.022 \times 10^{23} \text{ mol}^{-1}$.

$$\varepsilon_i = \frac{N_A}{\ln 10} \sigma_i \quad (5-9)$$

$$c_i = \frac{n_i}{N_A} \quad (5-10)$$

Introducing (5-8), (5-9) and (5-10) to (5-6), therefore transmittance can be defined as (5-11)

$$T = 10^{-\sum_{i=1}^N \epsilon_i \int_0^l c_i(z) dz} \quad (5-11)$$

Finally, using (5-11) to (5-7), it is possible to get (5-12), which is the Beer-Lambert law.

$$A = \sum_{i=1}^N \epsilon_i c_i l \quad (5-12)$$

There is a linear relationship between absorbance and concentration. Using (5-7), we can deduce that:

$$A = 2 - \log_{10} \%T \quad (5-13)$$

which can be drawn as a figure (Figure 5-7) showing the relationship between transmittance and absorbance.

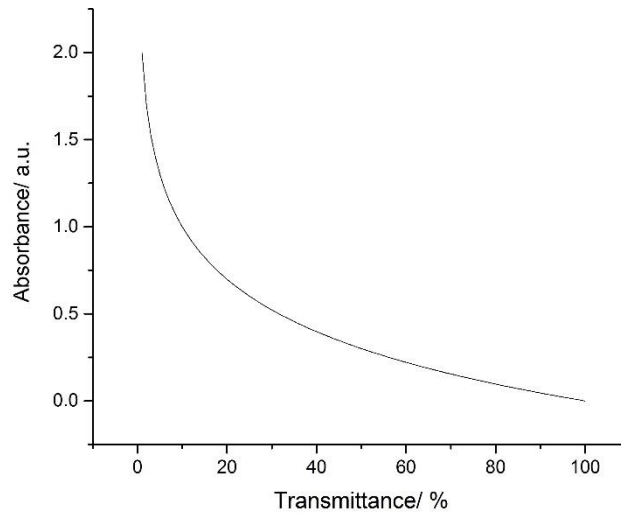


Figure 5-7. The relationship between transmittance and absorbance. T ranges from 1-100 %.

Absorbance can be deduced from the transmittance data using equation (5-13). Therefore an absorbance to thickness graph can be drawn as Figure 5-8. The thickness of laponite/PVA composites were measured by micrometer. Each sample

was given 3 readings and the mean was the final thickness of the film. The thickness of composites is in the range of 10-30 μm while PVA film is around 50 μm .

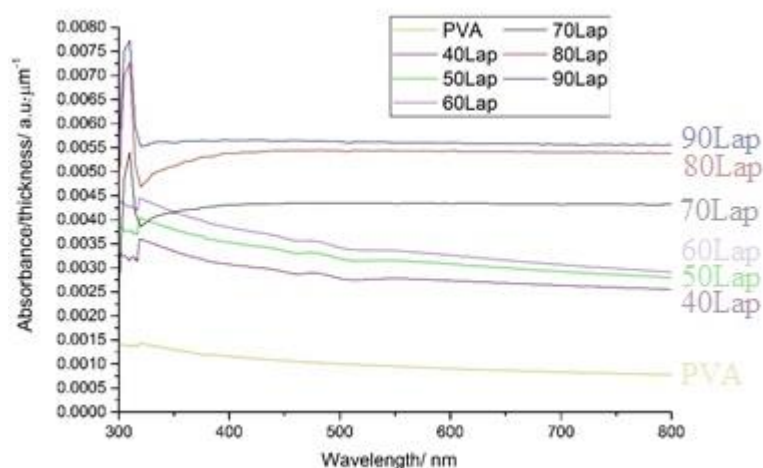
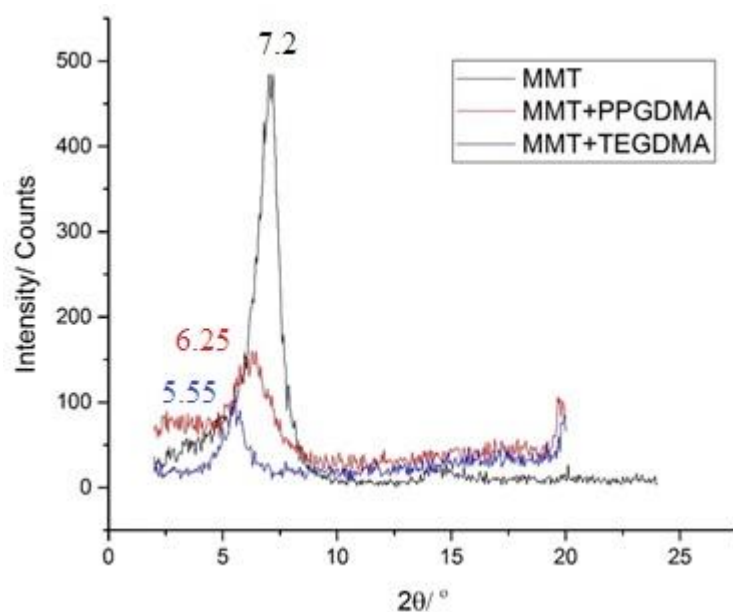


Figure 5-8. Graph showing absorbance to thickness of laponite composite within 400-800 nm. The samples were defined as wt. %.

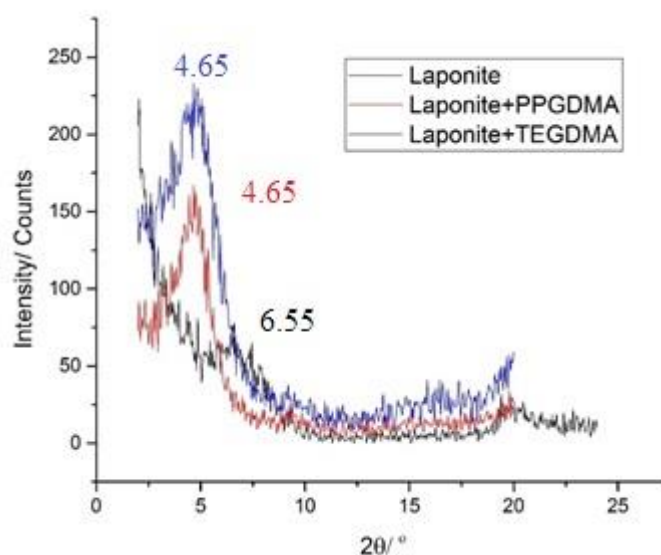
As reported by Zhu [3], the absorbance to thickness of MMT is in the range of 0.01-0.10 with the clay content 10-100 wt. % within 400-800 nm. In other words, the absorbance coefficient of MMT is much higher than that of laponite. The graph of absorbance to thickness of MMT/PVA composite was given in Appendix 2.

5.2 Study the photo polymerisation in the presence of clay

Ahead of polymerising monomer with the preformed self-assembled clay, it is important to make sure the polymer can intercalate into the interlayer of clays. Therefore, XRD was carried out to measure the basal spacing of the mixture. The mixture was cured in a brass holder and flattened for the XRD measurement.



(a)



(b)

Figure 5-9. XRD traces of clay/polymer mixture (a) Nano116 MMT mixed with PPGDMA and TEGDMA (b) laponite mixed with PPGDMA and TEGDMA.

Figures 5-9 (a) and (b) showing the XRD data of the polymerised samples should be compared to the clay powder as received. The peaks at 7.20° and 6.55° represent the $d_{(001)}$ plane for Nano116 MMT and laponite, respectively. The traces of the polymerised samples showed a shift in peak to a lower degree, which illustrated that the basal spacing increased by the intercalation of polymer. The results of the changing spacing are presented in Table 5-2.

Table 5-2. Calculated results from XRD traces from Figure 5-9

Clay sample	2 θ / °	Basal spacing/ Å	Change in spacing/ Å
MMT	7.2	12.26	-
MMT+PPGDMA	6.25	14.13	+1.87
MMT+TEGDMA	5.55	15.91	+3.65
Laponite	6.55	13.48	-
Laponite+PPGDMA	4.65	18.99	+5.51
Laponite+TEGDMA	4.65	18.99	+5.51

The conclusion of the results in Table 5-2 indicated that the intercalation of TEGDMA and PPGDMA in Nano16 MMT and laponite is possible resulting from the increase of the basal spacing of clay.

5.2.1 FTIR quantification of degree of conversion and rate of reaction

FTIR was carried out to study the behaviours of the clay in free radical polymerisation. Clay and monomer mixture were polymerised on an ATR FTIR spectrometer and ‘Timebase’ software was used. All of the spectra were plotted together to compare the changes as time goes on.

The monomer conversions are generally evaluated by measuring the amount of unreacted monomer after polymerisation [4]. A method was undertaken in the experiment following the same quantifying method as Young and co-workers did [5]. The degree of conversion and rate of reaction were measured by the differences of peak height at 1318 cm⁻¹ compared to a baseline. The baseline (1337 cm⁻¹) was chosen as the point where all the spectra coincided. It should be noted that the peak at 1318 cm⁻¹ is representative of the C-O stretch in the monomer structure. The reason why it is focused on is because this C-O functional group is the symbol of MMA monomer: after the monomer is converted into a polymer structure, this peak will decrease since there is less monomer than in pre-polymerisation state. The peaks assigned at 1635 cm⁻¹ is the C=C group which takes part in the polymerisation and turned into a C-C bond afterwards. However, the peak at 1635 cm⁻¹ may correspond

the O-H group as well. Thus, interlayer water in the clay especially in the laponite [6] could cause an error which may influence the results. In this case, 1635 cm^{-1} was not used in comparison. Young [5] suggested that the change in concentration is proportional to magnitude of absorbance change, which can also be deduced from equation (5-12). It is clear that the change in peak from Table 5-2 is caused by the polymerisation of monomer. Table 5-3 is given to identify the change in peak during polymerisation.

Table 5-3. FTIR assignment with comments corresponded to polymerisation.

Wavenumber / cm^{-1}	Assignment	Comments
1715	C=O stretch	For PPGDMA systems, this peak shifts to 1722 when the sample polymerises.
1636	O-H stretch or C=C stretch	O-H due to water present in the clay and C=C due to presence in monomer. Peak decreases in height when monomer changes to polymer.
1452	C-H scissor	Increase in peak height when monomer polymerises.
1318	C-O stretch	Decreases in height when monomer polymerises.
1295	C-O stretch	Decreases in height when monomer polymerises.
1250	C-C stretch	Increase in peak height when monomer polymerises.
1166	C-O stretch	Decreases in height when monomer polymerises.
1120	C-O-C asymmetric stretch	Increase in peak height when monomer polymerises.

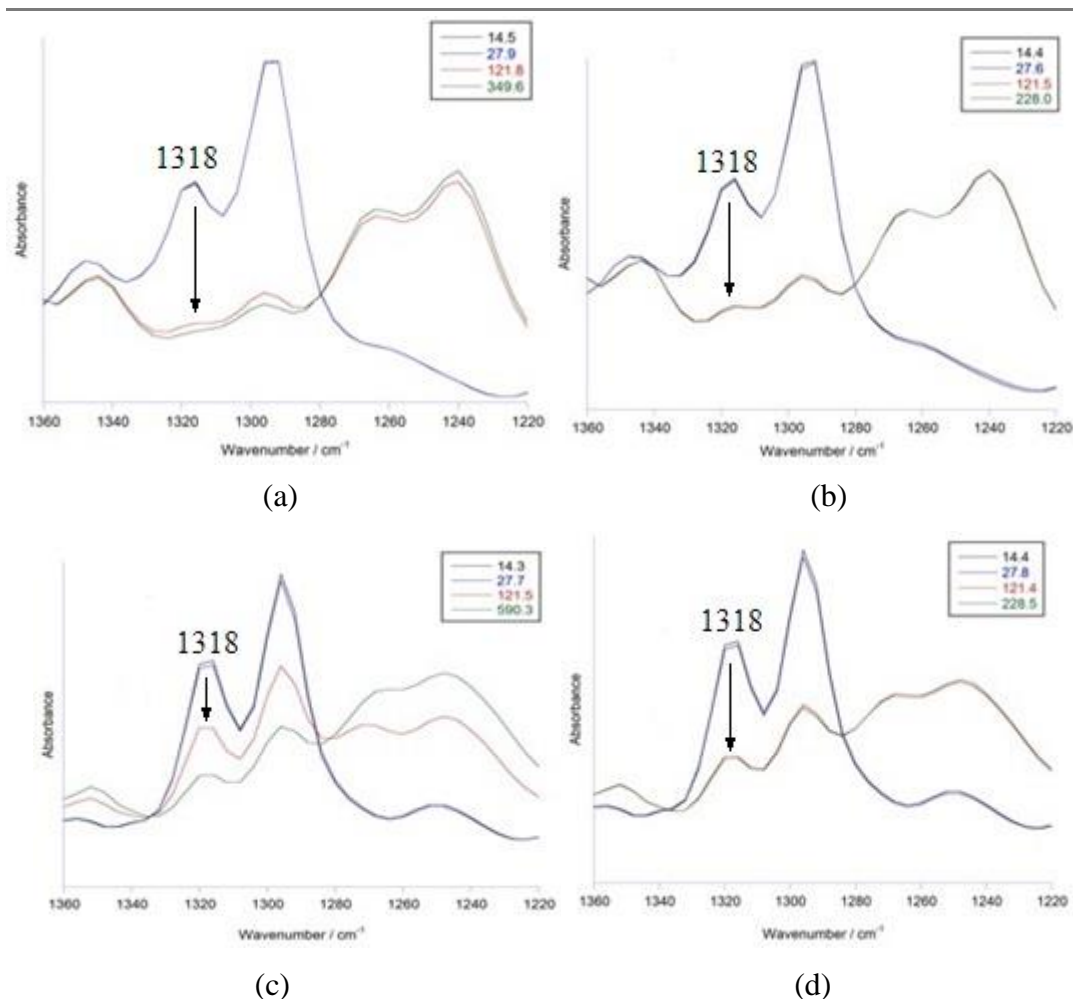


Figure 5-10. FTIR spectra of clay-monomer absorbance focusing on the peak at 1318 cm^{-1} . (a) PPGDMA with Nano116 MMT at 14.4, 27.9, 121.8 and 349.6 s, (b) PPGDMA with laponite at 14.4, 27.6, 121.5 and 228.0 s, (c) TEGDMA with MMT at 14.3, 27.7, 121.5 and 590.3 s, (d) TEGDMA with laponite at 14.4, 27.8, 121.4 and 228.5 s.

Figure 5-10 (a-d) show IR spectra of the clay-monomer absorbance (focused on 1318 cm^{-1}) versus time. Four spectra were plotted together as a function of time. The maximum rate of double bond conversion was calculated using the steepest gradient (dx/dt) of conversion versus time. The calculated results are shown in Table 5-4.

Table 5-4. The degree of conversion of monomer and maximum rate of reaction.

Sample	Monomer Conversion \pm SD (%)	Maximum Rate of Reaction (% s ⁻¹)
PPGDMA without clay	92.1 \pm 0.4	1.6
PPGDMA + MMT	93.8 \pm 0.7	1.8
PPGDMA + laponite	86.2 \pm 0.2	2.8
TEGDMA without clay	60.5 \pm 0.2	1.6
TEGDMA + MMT	72.7 \pm 0.5	0.8
TEGDMA + laponite	67.8 \pm 0.9	3.0

It can be concluded from Table 5-3 that PPGDMA itself has a quite high monomer conversion (92.1 %) The addition of Nano116 MMT increased the degree of conversion (92.1 to 93.8 %). On the other hand, in the presence of laponite, the degree of conversion rate reduced about 6 % compared to PPGDMA only.

The degree of conversion of TEGDMA/clay is higher than TEGDMA without clay. The TEGDMA is composed of a flexible chain, this could promote the double bond rotating to react with another methacrylate group which can increase the rate of polymerisation [6]. During polymerisation, the diffusion rates of the molecules and the rate of polymer chain growth decreases due to the increase of polymer viscosity, resulting in a reduced conversion [7].

According to the ratio of degree conversion to time, laponite accelerated the rate of polymerisation both in TEGDMA and PPGDMA.

5.2.2 Fabrication of ordered structures by preformed laponite film

Attempts were carried out to introduce the monomers (TEGDMA and PPGDMA) into the ordered laponite structures. A soaking process was undertaken as the monomer could be absorbed by the clay via capillary action. The preformed laponite films were immersed in the monomer, allowed to soak in the monomer for a given time then cured. It was found that the polymer was gathering at the surface of the

preformed clay film after polymerisation. The polymer could be easily peeled off from the surface. Extended time did not improve matters (86.4 ks - 259.2 ks).

Neither soaking process nor vacuum impregnation could help the monomer get into the layered clay film. It was clearly shown that the monomers were able to intercalate in the interlayer of clay as explained in section 5.1.1. However, introducing them into a preformed film which has the desired microstructure to mimic nacre, proved very difficult. This problem is at the core of the challenge of making nacre-like nanocomposites. Carbon and glass fiber reinforced plastics can be made by arranging the fibers into the weave that is required and then infiltrating the resin and curing it. Unfortunately, at the nanoscale infiltration is obstructed.

Therefore, it can be concluded that the monomer polymerised when it was in contact with the surface of the laponite layer. In this situation, the polymer could form an impenetrable layer, which prevented subsequent intercalation of the monomer into the interlayer of clay.

References

- [1] Herrera NN, Letoffe JM, Putaux JL, David L, Bourgeat-Lami E. Aqueous dispersions of silane-functionalized laponite clay platelets. A first step toward the elaboration of water-based polymer/clay nanocomposites. *Langmuir*. 2004 Mar 2;20(5):1564-71.
- [2] Shikinaka K, Aizawa K, Fujii N, Osada Y, Tokita M, Watanabe J, Shigehara K. Flexible, transparent nanocomposite film with a large clay component and ordered structure obtained by a simple solution-casting method. *Langmuir*. 2010 Jun 29;26(15):12493-5.
- [3] Zhu W, Lu CH, Chang FC, Kuo SW. Supramolecular ionic strength-modulating microstructures and properties of nacre-like biomimetic nanocomposites containing high loading clay. *RSC Advances*. 2012;2(15):6295-305.
- [4] Nakaza T, Kobayashi A, Hirano T, Kitagawa S, Ohtani H. Determination of monomer conversion in methacrylate-based polymer monoliths fixed in a capillary column by pyrolysis–gas chromatography. *Analytical Sciences*. 2012;28(9):917-20.
- [5] Young AM, Rafeeka SA, Howlett JA. FTIR investigation of monomer polymerisation and polyacid neutralisation kinetics and mechanisms in various aesthetic dental restorative materials. *Biomaterials*. 2004 Feb 29;25(5):823-33.
- [6] Patro TU, Wagner HD. Layer-by-layer assembled PVA/Laponite multilayer free-standing films and their mechanical and thermal properties. *Nanotechnology*. 2011 Oct 21;22(45):455706.
- [7] Schmidseider, J. In *Matrix and Resin Systems*; Rateitschak, K. H., Wolf, H., Eds.; Aesthetic Dentistry; Thieme: Germany, 2000; p. 87.

Chapter 6

Kaolinite Based Polymer Composite

This part of work was done with the cooperation with Hao Su, and Kate Sanders who were under my supervision and guidance.

6.1 Kaolinite and resin system.

6.1.1 Sedimentation experiment to adjust the optimal pH for kaolinite suspensions

A batch of vials was used to hold the samples of kaolinite suspension with different pH values. At each time step, the sediment height was recorded and a graph was plotted showing sediment height versus time (Figure 6-1).

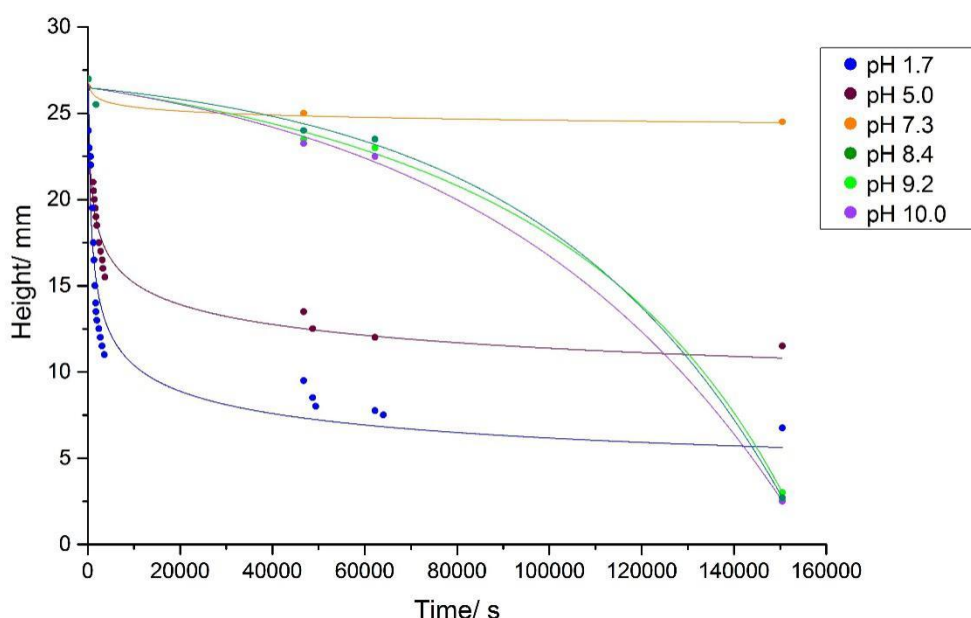


Figure 6-1. Sedimentation graph of kaolinite suspension with different pH values plotted by sediment height versus time. The error was too small to be shown in the figure compared with the height scale.

It can be concluded that pH 7.3 which is the pH of the original kaolinite suspended in distilled water was the optimal condition for the preparation of suspensions for making preformed sheets of kaolinite suspensions by self-assembly under vacuum filtration. Since the repulsion force of clay particles depends on the pH value, a higher pH value that moves the zeta potential away from the isoelectric point of the

surface can increase the energy barrier for agglomeration [1] leading to a more stable suspension. Generally, the pH should be 8-9 to form a stable suspension for kaolinite, sometimes it can be up to 10. However, in this experiment, pH 7.3 provided the more stable suspension. In this case, kaolinite suspensions for the preforming process can be kept at its original pH or at pH=10. The pH influence is compared in next section.

6.1.2 SEM of kaolinite sheets obtained by the self-assembly processes

SEM was carried out to investigate the structure of self-assembled kaolinite sheets. At the same time, the pH value was also taken into consideration, pH 7.3 and pH 10.0 suspensions were then used to perform self-assembled kaolinite for SEM. The cross section was divided into 2 parts, the top region which is close to the air and lower region which is close to the base of the petri-dish.

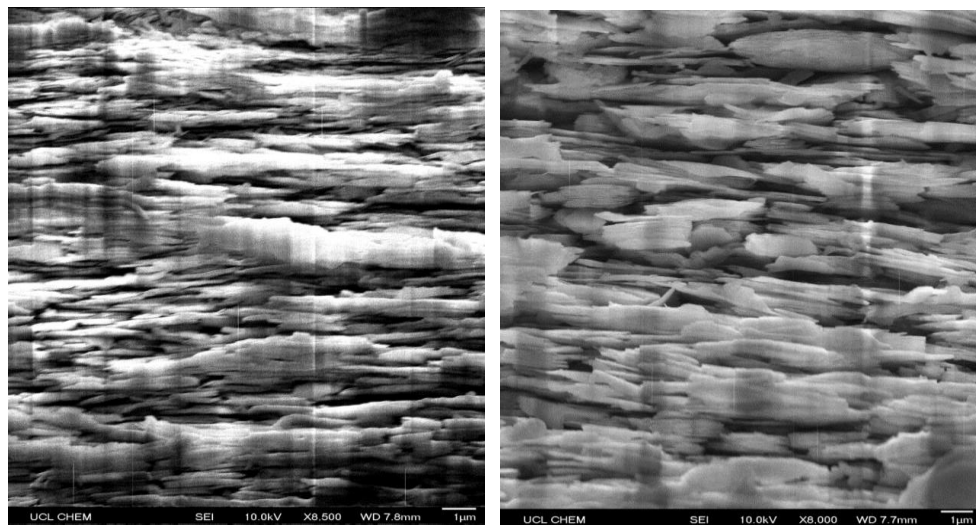


Figure 6-2. SEM of lower region of the kaolinite cross section at (left) pH=7.3 (right) pH =10.0.

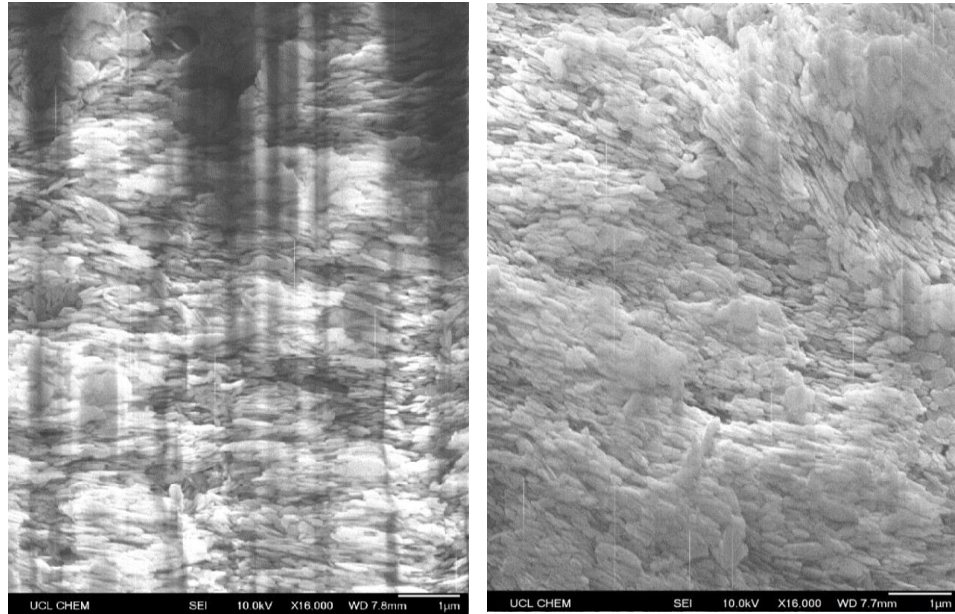


Figure 6-3. SEM of upper region of the kaolinite cross section at (left) pH=7.3 (right) pH=10.0.

As can be seen from Figures 6-2 and 6-3, a layered structure was found at both pH values of the lower region. Based on Walley's work [2], ordered structures are obtained by starting with a low concentration, generally 1-5 wt. %. At the initial stage where the concentration is comparatively low, rotation was possible for the clay platelets while subsequent drying locks them in position. Compared with MMT, kaolinite platelets have a larger size. The rotation would be more difficult with increased concentration. As concentration increases, the structure indeed becomes more irregular. The layers near the top side retain a lamellar structure with pH 7.3 while with pH 10.0, an inferior, less ordered structure was obtained from the self-assembly process.

6.1.3 Kaolinite film fabrication by vacuum filtration

According to Darcy's law [3], the time for turning clay particles into a packed sheet by filtration depends on the flux of water (J), defined as,

$$J = \frac{f}{V_c} \frac{dx}{dt} = -\frac{k}{\eta} \frac{\Delta p}{x} \quad (6-1)$$

where f is the packing fraction of kaolinite, V_c is the volume fraction in suspension, x is the thickness of kaolinite filter cake and the rate at which thickness increases is

$\frac{dx}{dt}$, Δp is the pressure difference across the growing layer, k is the average permeability of the filter cake and η is the dynamic viscosity of the liquid. Thus, by equating these, it can be deduced that,

$$\frac{dx}{dt} x = -\frac{k}{\eta} \frac{\Delta p}{f} V_c \quad (6-2)$$

Then integrating gives,

$$x^2 = -\frac{k}{\eta} \frac{\Delta p}{f} V_c t + c \quad (6-3)$$

Therefore, it indicates that the increase in thickness of a kaolinite filter cake is proportional to the square root of time.

$$x \propto \sqrt{t}$$

As the degree of ordered kaolinite depends on the rate of filtration, the pressure should be adjusted during the development of the filter cake to try to obtain a uniform rate of build-up. This is because at a high filtration rate, near the beginning, particles settle in a high local flow regime and fail to pack efficiently. When the rate of build-up of filter cake is slow, the particles are able to settle in an ordered manner. To prove this hypothesis, a simple experiment was set up by two suspensions with the same amount kaolinite, followed by the different filtration rate, 51 kPa vacuum pump assistant filtration over 3 hr compared to 0 kPa over 5 hr. Then SEM was carried out to investigate the structure of kaolinite filter cake, shown in Figure 6-4.

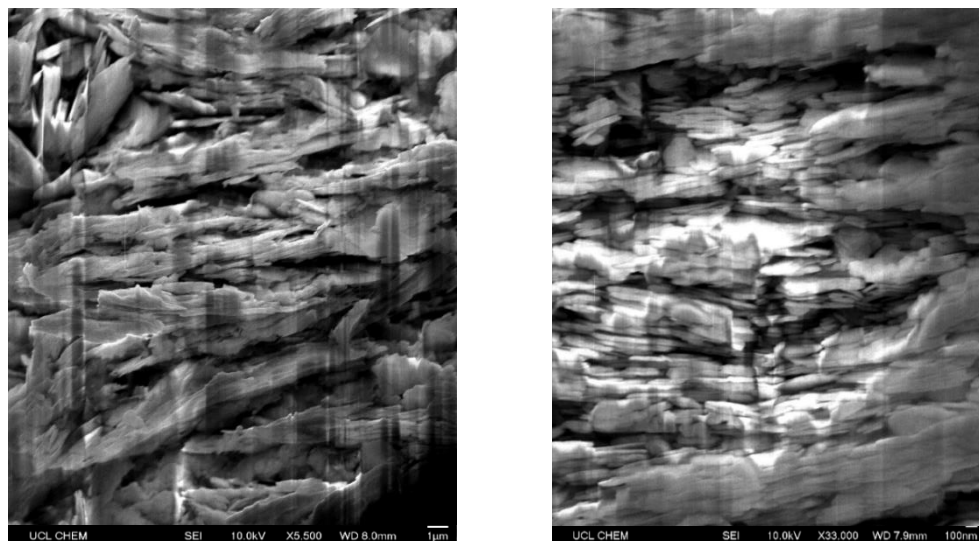


Figure 6-4. SEM images showing cross sections of kaolinite sheets filtered over 3 h (left) and 5 h (right).

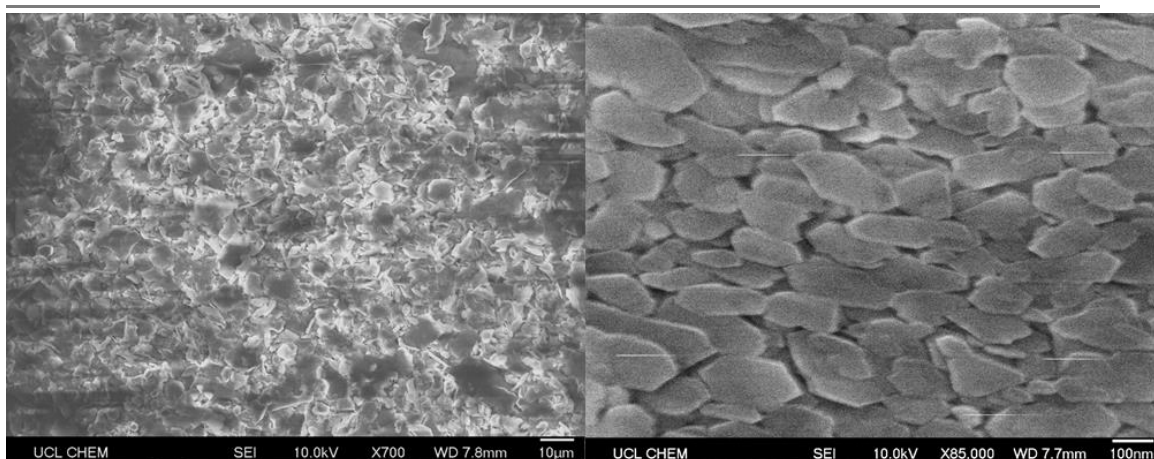


Figure 6-5. SEM images showing the bottom (left) and top (right) of a kaolinite film filtrated in 5 h.

As can be seen from Figure 6-4, the kaolinite filter cake with a slow filtration rate had dense packed layers. The orientation of layers has a preferential degree which is nearly parallel to each platelet. The filter cake with the slower filtration rate had a thickness about 550 μm compared 590 μm for the 3 hr filtration. Thinner sample means a dense packed structure since the weight and the area of filter cake are the same.

The different sides of the 5 hr sample were chosen to analyse the size of kaolinite platelets. The size of the lower side platelets is much larger (can be up to 5 μm) than that of top side (50-200 nm), as Figure 6-5 shows. It is believed that in the initial stages of filtration, sedimentation of larger particles occurred in the meanwhile. Thus, large platelets precipitated at the bottom side in a short time leading to a loose packed structure.

6.1.4 Packing efficiency of kaolinite filter cake

A batch of kaolinite filter cake was measured in order to obtain an estimate of the occupied volume fraction. The mass of each filter cake was kept the same as 20.0 g, weighed out by an analytical balance with readability of 0.0001 g. The balance is accurate to 0.00015, given by the manufacturer. The thicknesses were measured by a screw micrometre. The mean reading was obtained from three different parts of the

film. The width and length of frame was measured by a ruler. Taking the error of length reading into account, the standard deviation was taken as 0.5 mm.

Table 6-1. Thickness of kaolinite filter cake with different filtration rate.

Sample	Thickness/ μm	
	3 h filtration	5 h filtration
1	520	600
2	600	550
3	650	520
4	580	560
5	530	560
6	640	500
7	610	550
8	620	570
Mean	594	551
Standard deviation	± 44.7	± 28.5
Standard error of the mean	± 15.8	± 10.00
95% confidence interval	± 31.0	± 19.7

Thus, the apparent density of kaolinite filter cake is given as,

$$\rho_a = \frac{m}{V} \quad (6-4)$$

for the 3 hr infiltration filter cake, the apparent density

$$\rho_a = \frac{m}{V} = \frac{20 \times 10^{-3}}{150 \times 10^{-3} \times 200 \times 10^{-3} \times 594 \times 10^{-6}} = 1.12 \times 10^3 \text{ kg} \cdot \text{m}^{-3}$$

while for the 5 hr sample,

$$\rho_a = \frac{m}{V} = \frac{20 \times 10^{-3}}{150 \times 10^{-3} \times 200 \times 10^{-3} \times 551 \times 10^{-6}} = 1.21 \times 10^3 \text{ kg} \cdot \text{m}^{-3}$$

The packing efficiency was defined as

$$\% \text{ eff} = \frac{\rho_a}{\rho_k} \times 100\% \quad (6-5)$$

The packing efficiency for 3 hr and 5 hr sample was given as 45.53 % and 49.18 %, respectively.

$$\% eff_3 = \frac{\rho_a}{\rho_k} \times 100\% = \frac{1.12 \times 10^3}{2.46 \times 10^3} = 45.53\%$$

$$\% eff_5 = \frac{\rho_a}{\rho_k} \times 100\% = \frac{1.21 \times 10^3}{2.46 \times 10^3} = 49.18\%$$

As Hughes [3] suggested, the error of packing efficiency was calculated by the propagation of errors in each parameter. In this case the appropriate expression is:

$$\frac{\alpha_{ef}}{\% eff} = \sqrt{\left(\frac{\alpha_{Mass}}{m}\right)^2 + \left(\frac{\alpha_{Width}}{W}\right)^2 + \left(\frac{\alpha_{Length}}{L}\right)^2 + \left(\frac{\alpha_{Thickness}}{T}\right)^2} \quad (6-6)$$

The porosity was indicated as,

$$P = 1 - \% eff \quad (6-7)$$

The calculated porosity for 3 hr and 5 hr is given as 54.5 ± 1.2 %, 50.8 ± 0.9 %, respectively. Since open porosity exists in the kaolinite filter cake, it is feasible to infiltrate resin or monomer into the kaolinite plates.

6.1.4 Orientation function of kaolinite filter cake

The method used for quantifying the degree of orientation was the same as that described in section 4.3.3. The graph of orientation function is given in Appendix 3.

6.1.5 The possibility of infiltration of epoxy resin

Based on the study of MMT/resin system, it is known that the difficulties for resin infiltration depend on the structure of clay and viscosity of resin. Compared with MMT, kaolinite itself has larger plates and a coarse structure which should make it easier for resin infiltration.

A simple experiment was set up to verify the feasibility of resin infiltration. After mixing resin and hardener, a drop of Hxtal NYL-1 was placed separately on upper

and lower sides of kaolinite filter cake and then left at ambient conditions. RX900D resin, which was used in MMT/resin vacuum impregnation has a curing time 72 hr at 25 °C, while the curing time for Hxtal NYL-1 is about 7 days at the same temperature. In other words, Hxtal NYL-1 allows for a longer time for resin self-infiltration.

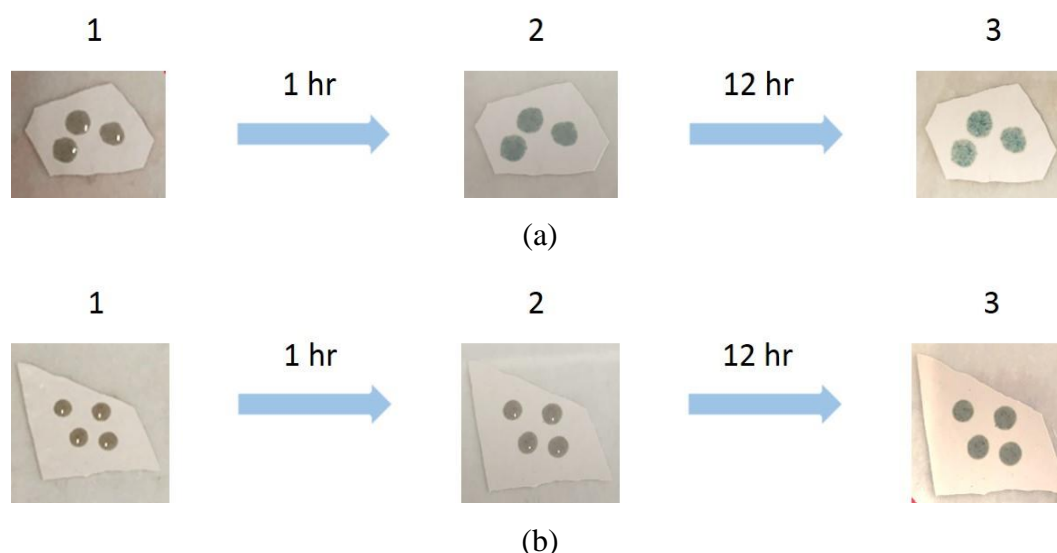


Figure 6-6. Infiltration experiment of kaolinite filter cake for 1 hr and 12 hr, (a) bottom side (b) top side of kaolinite.

As it can be seen from Figure 6-6, after 1 hr infiltration, the resin placed on the bottom side penetrated into the kaolinite. However, drops on the top side remained on the surface. As filtration time was extended into 12 hr, it seemed that all the drops infiltrated into clay. This experiment gave a preliminary idea that resin could penetrate in kaolinite at atmospheric pressure. Thus a possible pathway that the resin could penetrate into kaolinite by vacuum impregnation was explored.

6.1.6 Evidence of resin infiltration.

Kaolinite [4], which has the composition $\text{Al}_2\text{Si}_2\text{O}_5(\text{OH})_4$, is free from carbon inside the clay. In this case, the vacuum impregnation sample was subjected to EDS for the element mapping to see whether the vacuum impregnation works.

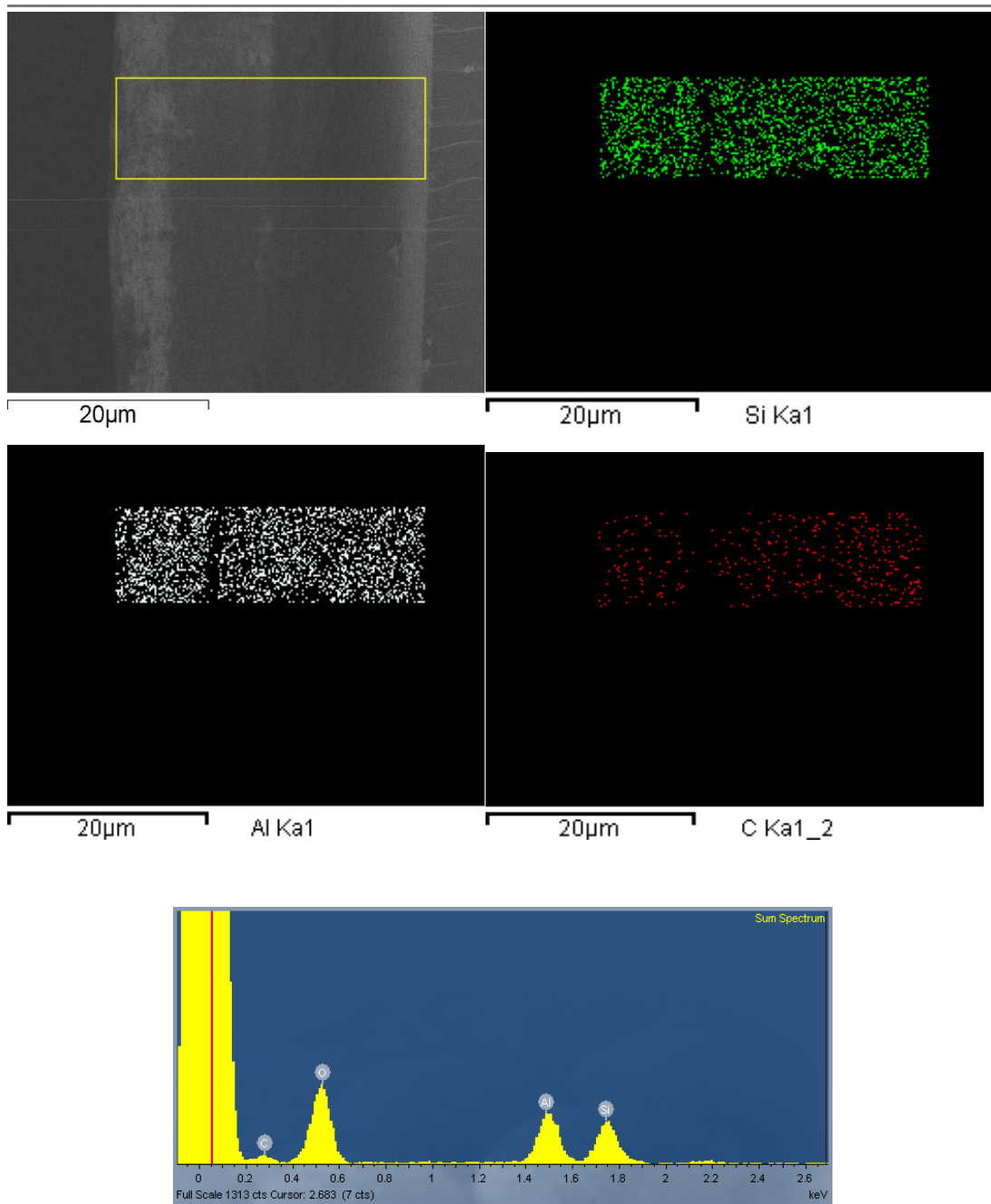


Figure 6-7. EDS mapping for vacuum impregnation sample.

From Figure 6-7, it can be indicated that drops penetrated into kaolinite successfully due to the carbon element detected. It proves that the resin can be introduced in kaolinite by vacuum impregnation.

However, the SEM figure showed there are some pores in the kaolinite plates which were not filled up by resin as Figure 6-8 shows.

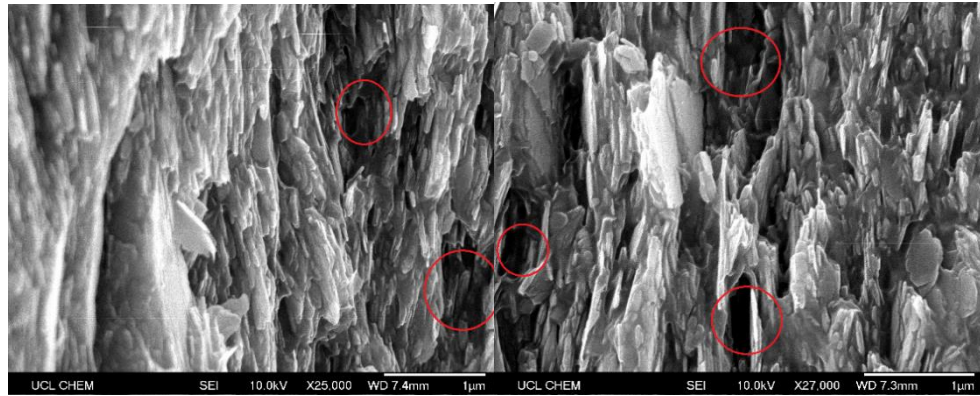


Figure 6-8. SEM of kaolinite plates by resin vacuum impregnation.

These larger pores could be caused by irregular stacking of plates during kaolinite filter cake formation. The purpose of using resin as an adhesive is to fill up the space between plates. If this fails, there is concerned about the stress concentration introduced by these defects when loaded. Therefore, absence of resin may degrade the mechanical properties.

6.1.7 Mechanical testing of kaolinite/resin composite.

After vacuum infiltration, the preformed kaolinite sheets were used to make kaolinite/resin composites by vacuum infiltration. These samples were tested in three point loading. The graph indicating three point flexural loading test was shown in Figure 6-9.

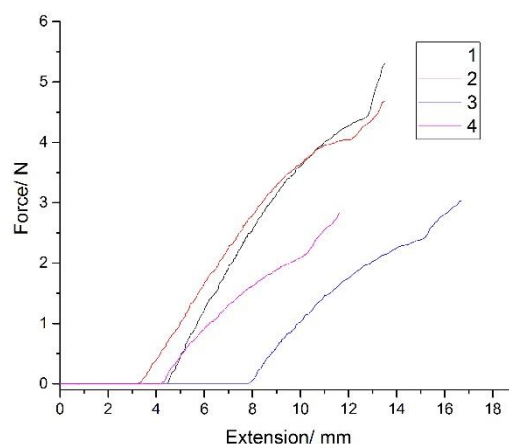


Figure 6-9. Graph of three point loading test.

Samples for three point bending test were prepared as rectangular bars, the flexural strength is defined as:

$$\sigma_f = \frac{3FL}{2bd^2} \quad (6-8)$$

where F is the applied force, L is the span of two supporting pins, b is the width of the sample and d is the thickness.

The flexural modulus E_f was calculated by:

$$E_f = \frac{L^3 m}{4bd^3} \quad (6-9)$$

where m is the gradient of the linear section of the load deflection curve.

The span of two supporting pins was kept at 45 ± 0.5 mm. The measured and calculated data were shown in Table 6-2.

Table 6-2. Measured and calculated data for three point loading test.

Sample	width of the sample/ mm	thickness of the sample/ mm	Force/ N	M*/ N mm ⁻¹	σ_f / MPa	E_f / GPa
1*	25.0 ± 0.5	0.550 ± 0.030	5.30	0.59 ± 0.01	47.3 ± 5.3	3.23 ± 0.55
2	24.0 ± 0.5	0.520 ± 0.020	4.68	0.46 ± 0.01	48.7 ± 3.9	3.11 ± 0.38
3	24.5 ± 0.5	0.500 ± 0.030	3.04	0.34 ± 0.01	33.5 ± 4.1	2.53 ± 0.52
4	25.0 ± 0.5	0.580 ± 0.030	2.83	0.38 ± 0.01	22.7 ± 2.4	1.77 ± 0.29

*Example of calculation was given in Appendix 4.

*M referred to the equation 6-9

The flexural strength of Hxtal NYL-1 epoxy resin is around 69.6 MPa (10100 Psi) and the flexural modulus is 2.52 GPa (365000 Psi) given by the supplier. It can be concluded the flexural strength of the composite was lower than the epoxy resin

from Table 6-2. However, compared with the flexural strength of pure kaolinite which was reported as 20.93 MPa by Mustafa [5], the composites showed an increase.

As indicated in Section 6.1.6, there are large pores in kaolinite filter cake which is the possible reason for the low flexural strength of the composite. During the vacuum impregnation, the resin failed to fill the pores in kaolinite as shown in the SEM images. According to Wright and Evans [6], the driving force for the organic flow to fill the pores is the different capillary pressure. The pressure difference was given as,

$$P = P_{non-wetting} - P_{wetting} = 2\gamma\left(\frac{\cos \theta_1}{r_1} - \frac{\cos \theta_2}{r_2}\right) \quad (6-10)$$

where γ is the surface tension, r is the effective pore radius, θ is the wetting angle. In this kaolinite/resin system, the pores were treated as non-wetting phase and the resin penetrated kaolinite regarded as the wetting phase. The contact angle was commonly low of organic resin on kaolinite, so the equation can be written as,

$$P \approx 2\gamma\left(\frac{1}{r_1} - \frac{1}{r_2}\right) \quad (6-11)$$

Since r_1 is the pore size of kaolinite, a larger pore means a lower capillary pressure which could make it harder for resin penetration resulting in filling of smaller pores which have preference for penetration but non-filling of larger pores. After resin has penetrated into the smaller pores, it was easy to form impermeable layers which make further penetration less possible, leaving the resin-empty large pores to degrade the mechanical properties. Considering the high viscosity of resin, a low viscous polymer should be used to make polymer/kaolinite composite. Therefore, MMA was chosen to prepare the composite by infiltration and in-situ polymerisation.

6.2 Kaolinite/PMMA polymer composites by thermal polymerisation

An initial experiment was carried out to analyse the optimum conditions for MMA polymerisation. In order to refine the method for MMA polymerisation, two initiator

(BPO and AIBN) were used for polymerisation and the time was recorded. The results are given in Table 6-3.

All samples undergo an increase in viscosity during polymerisation. Before the solid phase polymer appeared, the viscosity of the sample gradually increased. At the point when the viscous sample turned to a syrup-like gel, the polymer formed rapidly afterwards. This phenomenon is known as auto-acceleration, which is often occurs in radical chain polymerisation [7]. The polymer formed quickly in AIBN initiated samples during auto-acceleration while this was not observed in BPO initiated samples. It could be the contribution of the nitrogen by-product of the decomposition of AIBN. Rapid forming of polymer may cause defects in the polymer structure or even break the structure of clay after infiltration into clay's plates. Taking this into consideration, AIBN was subsequently eliminated from the thermal polymerisation of MMA. As indicated in Table 6-3, a higher concentration resulted in a faster rate of polymerisation for both initiators. A fairly short time was needed for MMA polymerisation. Thus, the best conditions selected for MMA polymerisation were: 1 wt. % BPO in stabilised MMA at 80°C for at least 70 min under N₂ in the aluminium polymerisation reactor. MMA buffer should be added in to prevent the evaporation of MMA.

Table 6-3. Results from experiments into optimisation of conditions for the thermal polymerisation of PMMA. [8]

Initiator concentration in MMA / wt. %	Polymerisation time / min			
	AIBN		BPO	
	Stabilised MMA	Unstabilised MMA	Stabilised MMA	Unstabilised MMA
70°C				
0.5	45	55	120	90
1	40	2400	110	75
80°C				
0.5	35	25	75	60
1	20	15	70	60

6.2.1 Redox polymerisation of MMA

From previous study of MMT/MMA, it was known that MMT can inhibit polymerisation of MMA due to the Fe ions or aluminium at the edge of the silicates. Kaolinite was tried again to see whether it is possible to polymerise MMA in the presence of it because there is no Fe in the kaolinite structure. The result confirmed the inhibition of polymerisation of MMA by kaolinite. It is thought that the aluminium at the edge of the silicates was the reason for inhibition since aluminium atoms can act as an electron acceptor to degrade the free radical polymerisation by termination or by direct electron transfer.

Therefore, an alternative path for thermal initiation, a redox system was developed. The system combined two parts, a powder part mixed with BPO and PMMA beads and a liquid part which consisted of pre-polymer suspension (PMMA in MMA) with an activator component [9,10]. The activator acts as a reducing agent. In general, it is an aromatic tertiary amine, such as N,N-dimethyl-p-toluidine (DMPT) or N,N-diethanol-p-toluidine (DEPT) [11]. The ratio for the mixture was 2:1 [12,13] of solid to liquid. After adding activator into the system, the viscosity increased quickly even under room temperature conditions. The mechanism for DMPT activation is shown in Figure 6-10.

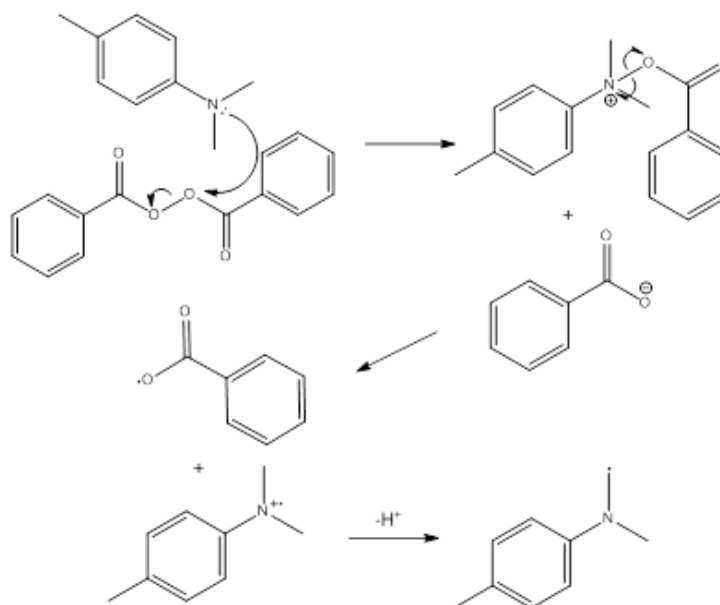


Figure 6-10. Mechanism of the redox reaction between DMPT and BPO. [14]

In order to make kaolinite/PMMA composites, a redox method could be used to provide a pathway for radical polymerisation without heating. However, due to the high viscosity of liquid phase of redox system, it is impossible for suspension to penetrate into a preformed kaolinite plates. A redox system of BPO and DMPT with liquid MMA alone was therefore developed to polymerise under ambient conditions.

A variation of the redox system used MMA containing BPO at 1, 1.5, 2 and 4 wt. %. A 1:1 molar ratio of DMPT: BPO was mixed to accelerate polymerisation. Concentrations above 4 wt. % BPO were not used even if they could increase the rate of polymerisation, because it can reduce the molecular weight of polymer which could affect the properties of PMMA and hence of the composite.

To reduce the time of polymerisation, samples were prepared with unstable MMA (MEHQ removed MMA) with a 4 wt. % concentration of BPO combined with a 1:1 molar ratio of DMPT in MMA. The FTIR peaks at 1635 cm^{-1} corresponded to C=C in MMA disappeared after redox polymerisation, showing the MMA fully polymerised and no C=C left in resultant. FTIR of MMA and PMMA by redox polymerisation and PMMA/kaolinite by redox polymerisation were given in Appendix 5.

6.2.2 Mechanical testing of samples prepared by redox polymerisation in the presence of kaolinite

The 5 h filtration kaolinite sheet was cut by a scalpel into rectangular shape for the redox polymerisation. Oxygen in ambient air could inhibit the polymerisation, so redox polymerisation was carried out under N_2 atmosphere.

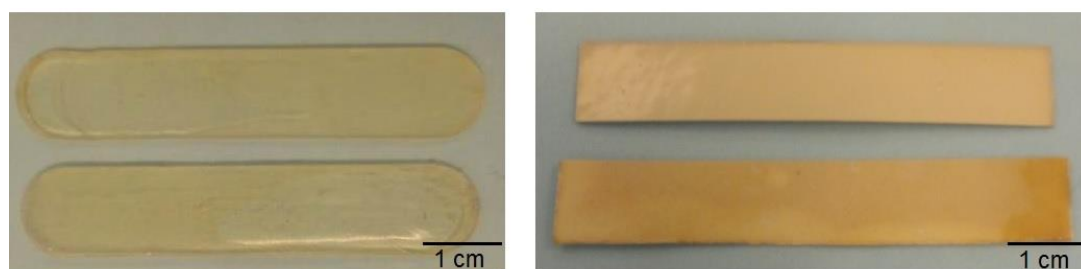


Figure 6-11. PMMA (left); PMMA/kaolinite composites (right) showing top (above) and bottom (below) side of kaolinite filter cake.

PMMA samples were prepared by the same redox polymerisation to compare the mechanical performance of the PMMA-kaolinite composite. Since the kaolinite sheets are fragile, they are not taken into account as the comparison experiment. Figure 6-11 shows the mechanical testing samples.

6.2.3 Mechanical testing of kaolinite/PMMA composite

The three point loading test was carried out to analyse the mechanical properties of both PMMA from redox polymerisation and kaolinite/PMMA composite. The results are given in Table 6-4.

Table 6-4. Results of three point loading of redox polymerised PMMA and PMMA/Kaolinite composite.

	Redox polymerised PMMA		PMMA-Kaolinite composite	
	σ_f / MPa	E_f / GPa	σ_f / MPa	E_f / GPa
Mean*	40	2.5	40	30
Standard deviation	± 30	± 0.9	± 30	± 30
Standard Error of the Mean	± 10	± 0.3	± 10	± 10

*Figures and results were given in Appendix 6

As reported [15] the flexural strength of PMMA was 64.2 MPa and the flexural modulus of it is 2.5 GPa. The flexural strength of redox polymerisation PMMA samples is 40 MPa showing a lower value compared with reported data while the flexural modulus shows not much difference.

In terms of composite, even though there is not much difference in the flexural strength between PMMA and composite, the flexural modulus shows a significant increase from 2.5 GPa to 30 GPa. This indicated that redox polymerisation was successful in using MMA only in presence of kaolinite. Since the pre-polymer has a comparatively high viscosity, the redox polymerisation is not the desirable pathway to make MMT/PMMA nanocomposites at the nanoscale.

References

- [1] Zeta-Meter, Inc. 2015. Zeta Potential: A Complete Course in 5 Minutes. Publications of Zeta-Meter, pp. 1-8.
- [2] Walley P, Zhang Y, Evans JR. Self-assembly of montmorillonite platelets during drying. *Bioinspiration & Biomimetics*. 2012; 7(4):046004.
- [3] Hughes, I. & Hase, T. P. A. 2010. Measurements and their uncertainties: a practical guide to modern error analysis. Oxford: Oxford University Press.
- [4] Imerys Performance & Filtration Minerals. 2012. Barrisurf™ - New Concept for Barrier Coatings. Technical information: Plastics, pp. 1-2.
- [5] Al Bakri AM, Liyana J, Faheem M, Tahir M, Kamarudin H, Razak AR, Yahya Z, Alida A. Effect on strength and hardness of clay ceramic substrate after treatment using kaolin based geopolymer glaze. In *Key Engineering Materials 2014* (Vol. 594, pp. 575-580). Trans Tech Publications.
- [6] Wright JK, Evans JR. Removal of organic vehicle from moulded ceramic bodies by capillary action. *Ceramics International*. 1991 Jan 1;17(2):79-87.
- [7] Odian, G. Principles of Polymerisation, 4th edn.; John Wiley & Sons: New Jersey, pp 198-286
- [8] Sanders, K. Composites that mimic the microstructure of nacre. UCL. 2016
- [9] Tham, W. L.; Chow, W. S.; Mohd Ishak, Z. A., The effect of 3-(trimethoxysilyl) propyl methacrylate on the mechanical, thermal, and morphological properties of poly(methyl methacrylate)/hydroxyapatite composites, *J. Appl. Polym. Sci.*, 2010, 118, 218-228.
- [10] Peng, S.; Zhang, J., *Engineering Geology for Underground Rocks*; Springer-Verlag: Berlin, 2007; pp 3.
- [11] Kwon, T.; Bagheri, R.; Kim, Y. K.; Kim, K.; Burrow, M., Cure mechanisms in materials for use in esthetic dentistry, *J. Investig. Clin. Dent.*, 2011, 3, 3-16.
- [12] Leonard, A.; Sender, C.; Lavergne, C.; Benoit, D., Two-component system for bone cement. U.S. Patent 20110237705 A1, Sep 29, 2011.
- [13] Vasquez, B.; Deb, S.; Bonfield, W., Optimization of benzoyl peroxide concentration in an experimental bone cement based on poly(methyl methacrylate), *J. Mater. Sci. Mater. Med.*, **1997**, 8, 455-460.
- [14] Schulz, M.; Shanov, V.; Yin, Z., *Nanotube Superfiber Materials: Changing Engineering Design*; Elsevier: Oxford, 2014; pp 632-533.

[15] Lee AJ, Ling RS, Vangala SS. The mechanical properties of bone cements.
Journal of Medical Engineering & Technology. 1977 Jan 1;1(3):137-40.

Chapter 7

Conclusions and Future work

7.1 Conclusions

As reported in Chapter 4, a drying process was used to fabricate a montmorillonite clay and PVA self-assembled structure. Experiments carried out using XRD analysis confirmed that the intercalation of PVA was thermodynamically feasible, since there was an enlargement in the basal spacing of the MMT. SEM figures give a strong support that evaporation-induced self-assembly is a feasible method to mimic nacre-like nanocomposite using MMT/PVA. It indicates that the ordered structure is not disrupted when dispersed clay particles are self-assembled by drying from a water-based polymer solution with polyvinyl alcohol even though the adsorbed polymer layer is expected to change the surface interactions. The mechanical test shows that the 50 vol. % MMT/PVA obtained the best mechanical properties among different volume fractions but the strength was still quite low, only 40.5 MPa. After trying new clay (BH natural) and a higher M_w PVA, the tensile strength showed no significant change indicating that the grades of the constituents were not responsible for the low strength. After introducing a centrifugation process and a modified cutting method, the tensile strength of the composite can be reached to 98 MPa and the highest value comes from 50 vol. % MMT/PVA composite. It then can be concluded that the low mechanical properties caused by the unexfoliated clay fraction and the impurities present in the original clay.

A structural polymer, epoxy resin, was then introduced to preformed MMT film made by the self-drying process in an attempt to fabricate a nacre-like composite using vacuum impregnation. An ion-exchanged MMT (PPD-MMT) was also tried to achieve the nacre-like structure. Even though the ordered structure was confirmed by XRD and SEM, the tensile strength of MMT/resin was 28.9 MPa and PPD-MMT/resin was 22.6 MPa, respectively. These low mechanical properties were contributed to by the high viscosity of resin which prevented it gaining access to the ordered structure.

In the next step, a low viscosity monomer MMA was used to prepare the nacre-like structure by infiltration and in-situ polymerisation. The XRD traces indicated that MMA can indeed intercalate into MMT galleries. However, the MMT clay acted as

an inhibitor in the free radical polymerisation of MMA. This could be caused by the Fe ions or by the aluminium located the edge of the silicate layers.

Laponite based composites were studied in Chapter 5 and it can be concluded that the ordered structure was obtained by the evaporation-induced assembly process. This is supported by XRD and SEM. It is worth noting that laponite/PVA composite has optical properties which give at least 80 % transparency in the range of visible light. Since then, a photo polymerisation idea came out based on the high transparent properties of laponite. The results shows that the PPGDMA and TEGDMA polymerised when it was in contacted with the surface of the laponite layer and formed an impenetrable layer, which prevented subsequent the monomer from entering into the preformed laponite and the intercalating into the interlayer of clay. Even though the laponite did not inhibit the polymerisation of acrylic groups like MMT did, it also failed to allow penetration of the monomer into the interlayer of clays in another way, accelerating the polymerisation of PPGDMA and TEGDMA.

A plate-like kaolinite was obtained, which has larger particle size than MMT or laponite and it was used to make composites at the micro-level instead of the nanoscale. A low viscosity resin used for commercial applications that demand a very long curing time was then introduced to preformed kaolinite filter cake by vacuum impregnation. The highest flexural strength of the composites was then 48.7 MPa, which was lower than the pure epoxy resin, but showed a slight increase compared with pure kaolinite. The flexural modulus was roughly the same as resin. The SEM images pointed out there were large unfilled pores among the kaolinite particles. It could be the main reason for the low mechanical properties of kaolinite. However, the pores may be filled by a low viscosity flow of polymer. Taking this into consideration, a redox polymerisation method was developed for making the kaolinite composite. After three point loading test, the flexural modulus shows a significant increase from 2.5 GPa (PMMA) to 30 GPa (composite). This indicated that redox polymerisation was successful in using MMA only in presence of kaolinite to make a traditional composite but with ordered planar random arrangement of particles.

A short chapter Appendix 1 indicated that GO/PVA nacre-like nanocomposites could be successfully synthesised by a solution-casting process. After ultrasonication, the GO layers were separated into small tactoids changing from 19-20 stacks to 2-3 stacks. As with the MMT/PVA nanocomposites described above, the microstructure was established and the polymer was put in place but a water-soluble polymer is not the ideal choice for the matrix.

This project demonstrates that the microstructure required for nacre-like composites can be made by self-assembly during drying and by filtration methods. It also demonstrates that various structural polymers can intercalate into some of the smectic clays used. However, the very serious problem that it highlights is that when attempts are made to infiltrate a non-water soluble polymer such as an epoxy resin into the preformed structure, infiltration is either obstructed at the surface or large internal pores remain unfilled. The strategy for materials manufacture that has become commonplace for glass and carbon fibre composites, namely to assemble the reinforcing phase into the geometry that is predicted to give high mechanical strength and then to infiltrate the resins does not work so effectively at the fine scale of reinforcement and pore size required for clay mineral reinforcement.

7.2 Future work

Although the nacre-like composites were successfully fabricated, there are still some issues that need to be developed in this field for the future. The composites fall behind in unification with the natural nacre: the inorganic ratio of the artificial nacre is much less than that of natural nacre. The accurate control of the thickness of the layered structure is still a major challenge. Rapid self-assembly needs to be investigated by both physical and chemical methods. The process is still under study in an attempt to mimic the nacre-like structure more accurately and on a larger scale.

In Chapter 4, the reported mechanical properties of the composites could be further improved. As reported [1, 2] from other groups, the PVA can be crosslinked by GA or boric acid. After cross-linking, the mechanical properties of composites should be increased due to the formation of the acetal bonding after GA crosslinking. A series of different molar ratios of PVA to crosslinking agent should be undertaken.

Chitosan and gelatine could be also investigated by the self-drying process since both of them are water-soluble polymers. Another possible way to improve the mechanical properties of composites could be chemical grafting the surface of clay by functional groups like -OH or -NH₂, which could be easier to interact with the function groups in polymer.

The laponite accelerated the polymerisation of acrylic groups as indicated in Chapter 5, the mechanism was not clear and needs to be further researched. Other groups [3, 4] reported that clay has fire retardant properties as well as barrier properties. It could be a promising way to produce the laponite composites as the shell of solar cells due to its high optical transparency. In this case, the laponite composites allow the light pass and keep the oxygen outside to protect the sensitive solar cell from oxidation.

The problem with the kaolinite/resin system was lack of complete pore filling. It should be infiltrated by a reactive dilute organic agent used to reduce the resin viscosity. If the resin can be penetrated into spaces of kaolinite at a low viscosity, the mechanical properties should be further promoted, after fully filling the pores in kaolinite sheets.

Furthermore, the bio-degradable plastic could be a burgeoning field to be investigated with clay-polymer composites. The polymer could be from biomass like cellulose, fibronectin and collagen. Upon disposal to landfill, the clay would return to the ground as the polymer degrades to products that can be processed in the biosphere.

Regardless of the present cost of preparation of GO, it could become a very important material in the future. As it has functional groups in its structure, GO can react with various polymers. It can crosslink with dopamine alone [5] or combined with polyurethane [6] to form a strong composite.

Biom mineralization would be another attempt to mimic the natural composite. The hierarchical structure of ivory can be fabricated by this process. The calcium

carbonate could be combined with silk fibroin microsphere to form an ivory-like material.

Clay-polymer hydrogels could be another potential direction. Polyacrylamide or poly(N-isopropylacrylamide) could be combined with clay to generate the hydrogel. The hydrogel usually shows an extremely large elastic deformation. Unlike the brittle material, the hydrogel displays regenerative properties.

Besides use in structural composites, the clay minerals can be also used in bio-applications, such as cell adhesion and proliferation, as well as drug and gene delivery because of clay nanoparticles can be interacted with biomolecules, polymer as well as cells. MMT can be used for protection of naked DNA from degradation within the acidic environment of the stomach. With laponite, it can be found that when added to a hydrogel film, the clay provided a specific site for the cell and polymer attachment.

References

- [1] Podsiadlo P, Kaushik AK, Arruda EM, Waas AM, Shim BS, Xu J, Nandivada H, Pumpilin BG, Lahann J, Ramamoorthy A, Kotov NA. Ultrastrong and stiff layered polymer nanocomposites. *Science*. 2007 Oct 5;318(5847):80-3.
- [2] Walther A, Bjurhager I, Malho JM, Pere J, Ruokolainen J, Berglund LA, Ikkala O. Large-area, lightweight and thick biomimetic composites with superior material properties via fast, economic, and green pathways. *Nano Letters*. 2010 Mar 10;10(8):2742-8.
- [3] Shikinaka K, Aizawa K, Osada Y, Shigehara K. Fire-shielding properties of flexible, transparent laponite-PEG hybrid film. *Chemistry Letters*. 2011;40(12):1389-91.
- [4] Gaume J, Taviot-Gueho C, Cros S, Rivaton A, Therias S, Gardette JL. Optimization of PVA clay nanocomposite for ultra-barrier multilayer encapsulation of organic solar cells. *Solar energy materials and solar cells*. 2012 Apr 30;99:240-9.
- [5] Cui W, Li M, Liu J, Wang B, Zhang C, Jiang L, Cheng Q. A strong integrated strength and toughness artificial nacre based on dopamine cross-linked graphene oxide. *ACS nano*. 2014 Aug 12;8(9):9511-7.
- [6] Wan S, Li Y, Peng J, Hu H, Cheng Q, Jiang L. Synergistic Toughening of Graphene Oxide–Molybdenum Disulfide–Thermoplastic Polyurethane Ternary Artificial Nacre. *ACS nano*. 2015 Jan 7;9(1):708-14.

Appendix

Appendix 1. Graphene oxide and PVA composites

A1.1 Characterisation of GO

Figure A1-1 shows the X-ray diffraction traces for the graphene oxide. The peak at $2\theta=10.84^\circ$ is the GO peak showing a $d_{(002)}$ spacing about 8.15 \AA which was similar to that as reported 8.3 \AA [1] and 8.6 \AA [2]. The author suggested that the distance (8.3 \AA) was contributed to by a one-molecule thick layer of water bonded between the graphene oxide sheets [1]. Due to the freeze-drying process, the water in prepared GO was removed, thus it gave a lower value 8.15 \AA compared with the former.

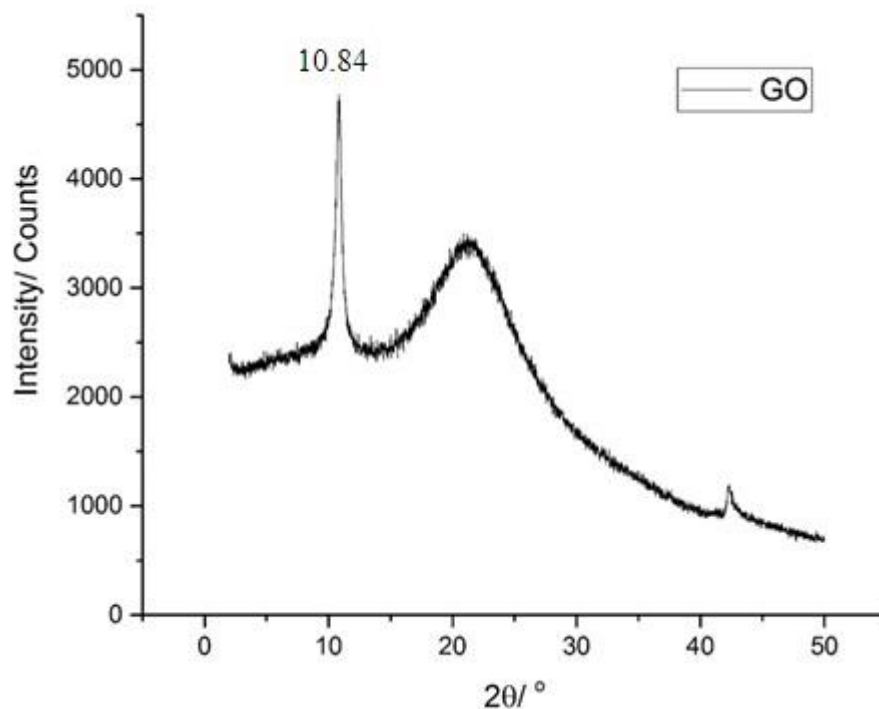


Figure A1-1. X-ray diffraction of prepared GO.

According to the Scherrer equation, which was defined as,

$$\tau = \frac{K\lambda}{\beta \cos \theta} \quad (\text{A1-1})$$

where τ is the dimension of ordered layers, K is the dimensionless shape factor, λ is the wavelength of X-ray, β is the full width of at half of maximum (FWHM), in

radians, θ is the angle read from the peak. The K is roughly 0.9 and λ is 1.54056 Å, β is $0.51 \times 22/180/7$. θ is 5.42 °.

Then the calculated $\tau=156.4$ Å from Figure A1-1. This value represents 19 to 20 stacks of graphene oxide sheets.

A1.2 Characterisation of GO/PVA nanocomposite.

Figure A1-2 shows that XRD traces for GO/PVA composites after the self-assembly process at ambient conditions. All of the samples peaks showed a shift to a lower angle due to increases of spacing between GO interlayers. The results were given in Table A1-1.

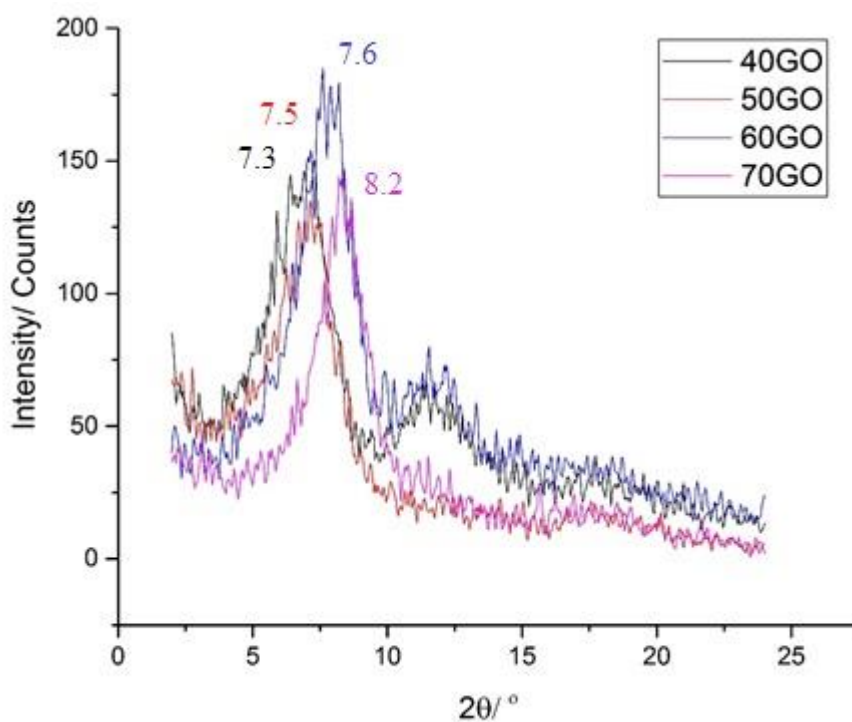


Figure A1-2. XRD traces for GO/PVA composites after self-assembly process at ambient temperature. The samples are identified by wt. % of GO.

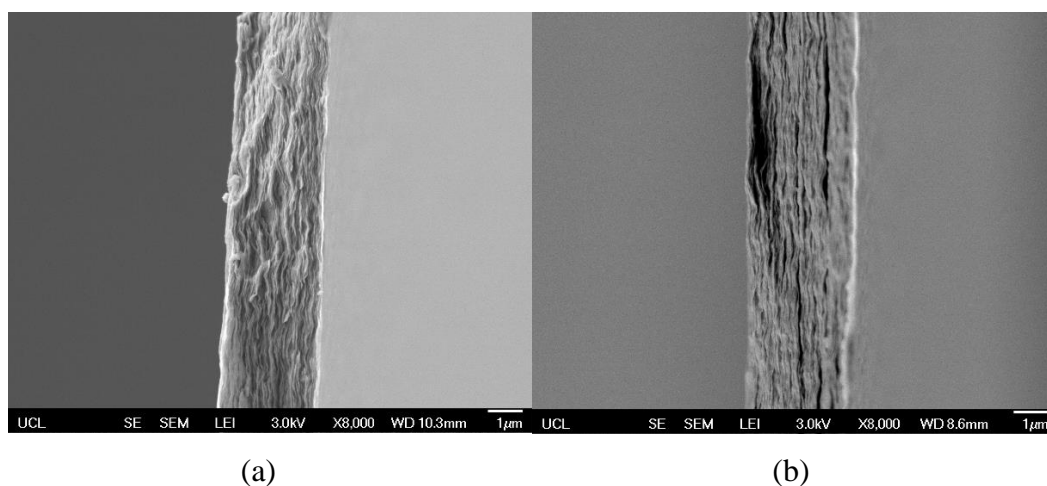
Table A1-1. Results from XRD traces of GO/PVA composites.

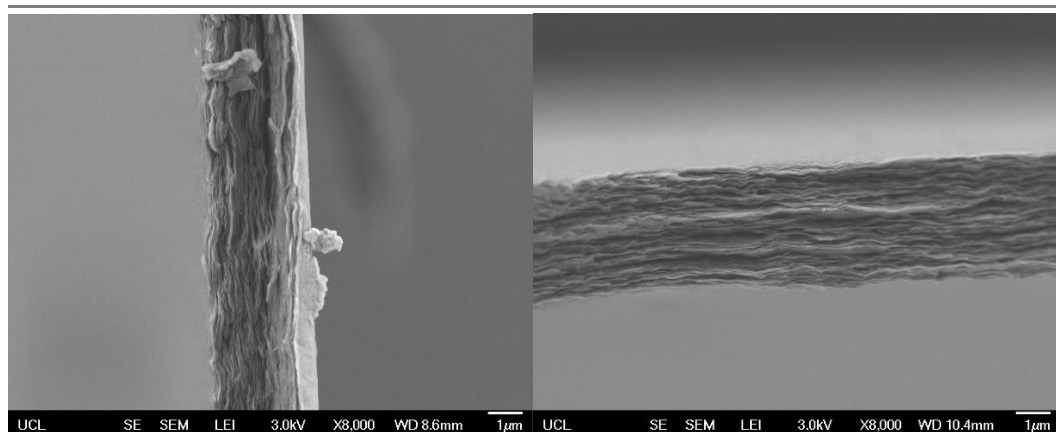
GO samples wt. %	$2\theta/^\circ$	Basal spacing/ \AA	change of $d_{002}/\text{\AA}$
40	7.3	12.10 ± 0.01	+ 3.95
50	7.5	11.78 ± 0.01	+ 3.63
60	7.6	11.62 ± 0.01	+ 3.47
70	8.2	10.77 ± 0.01	+ 2.62

According to equation A1-1, the dimension of ordered layers can be calculated. Take 40 wt. % GO/PVA composite as an example. The K was about 0.9 and λ is 1.54056 \AA , β is $3.50 \times 22/180/7$. θ is 3.65 $^\circ$. Then τ was 22.73 \AA , it gave a brief idea that after introducing to ultrasonic treatment for 72 hr, the GO was broken into small parts of layers and only 2-3 stacked GO sheets with bonded PVA in interlayers.

A1.3 SEM figures of GO and PVA composites made by self-drying process

As it indicated in Figure A1-3, all of the composites made by self-drying process showed a layered structure in high levels of orientation. The concentration of graphene oxide dispersion is only 0.2 wt. %. With such a low concentration, the composite film made by GO with PVA is quite thin (less than 15 μm).





(c)

(d)

Figure A1-3. Scanning electron micrographs of fracture surface of (a) 40 wt. % GO/PVA composites (b) 50 wt. % GO/PVA composites (c) 60 wt. % GO/PVA composites (d) 70 wt. % GO/PVA composites.

One of the aims of this project is to fabricate a relatively low cost structural material. In this case, GO cannot be prepared in high quantities in the laboratory and has a relatively high cost. Thus, it could be a good choice of future work on high-performance composites.

Appendix 2. The absorbance to thickness of MMT/PVA composite

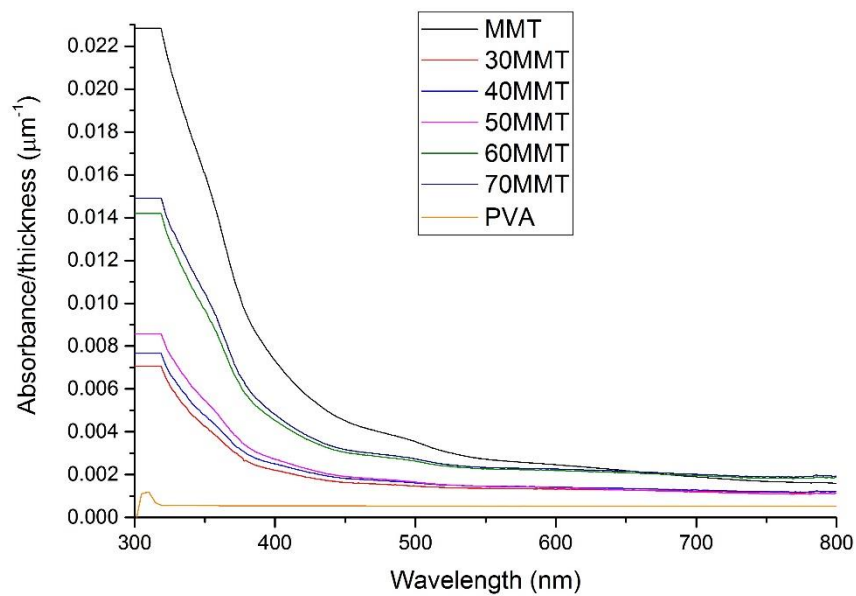


Figure A2-1. The absorbance to thickness of MMT/PVA composite. The sample was defined in volume percentage of MMT.

Appendix 3. Orientation function of kaolinite

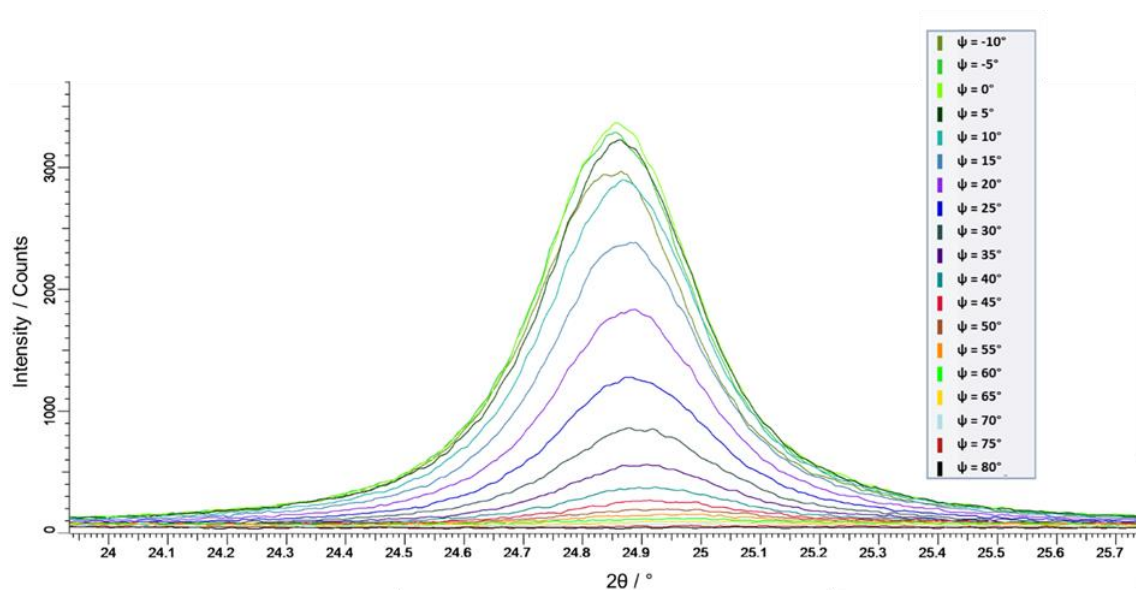


Figure A3-1. X-ray diffraction of the variation of the intensity of the kaolinite (002) peak reflection by changes in the tilt angle, ψ .

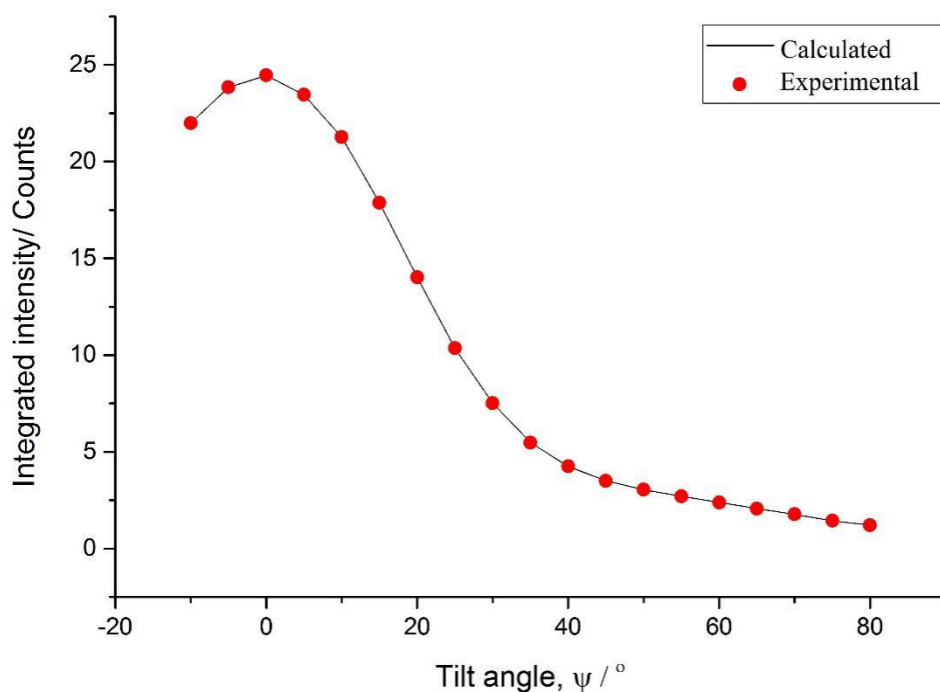


Figure A3-2. Graph showing experimental kaolinite orientation distribution function.

Appendix 4. Flexural strength and modulus of kaolinite/resin composite

Flexural strength calculation for kaolinite/resin sample 1:

$F = 5.3 \text{ N}$, $l = (45.00 \pm 0.5) \text{ mm}$ and $b = (25.0 \pm 0.5) \text{ mm}$

$d = (0.55 \pm 0.03) \text{ mm}$, so $d^2 = 0.55^2 = 0.3025 \text{ mm}^2$

Absolute error in $d^2 = 2 \times 0.55 \times 0.03 = \pm 0.033 \text{ mm}^2$

So $d^2 = (0.3025 \pm 0.033) \text{ mm}^2$

Therefore $\sigma_f = (3 \times 5.3 \times 45.00) / (2 \times 25 \times 0.3025) \text{ MPa} = 47.3 \text{ MPa}$

And relative error in $\sigma_f = \sqrt{((0.5/45)^2 + (0.5/25)^2 + (0.033/0.3025)^2)} = 0.11$

So absolute error in $\sigma_f = 0.11 \times 47.3 \text{ MPa} = \pm 5.27 \text{ MPa}$

Overall, $\sigma_f = (47.3 \pm 5.3) \text{ MPa}$

Flexural modulus calculation for kaolinite/resin sample 1:

The gradient, m , for the linear portion of the stress-strain graphs of samples was calculated, along with an estimate of its uncertainty.

$m = (0.59 \pm 0.01) \text{ N mm}^{-1}$, $d = (0.55 \pm 0.03) \text{ mm}$,

$l = (45.00 \pm 0.5) \text{ mm}$, so $l^3 = 45^3 = 91125 \text{ mm}^3$

Absolute error in $l^3 = 3 \times 45^2 \times 0.5 = 3037.5 \text{ mm}^3$

$d^3 = 0.55^3 = 0.166375 \text{ mm}^3$

Absolute error in $d^3 = 3 \times 0.55^2 \times 0.03 = \pm 0.027225 \text{ mm}^3$

Therefore $E_f = (91125 \times 0.59) / (4 \times 25 \times 0.166375) = 3231 \text{ MPa} = 3.23 \text{ GPa}$

And relative error in

$E_f = \sqrt{((3037.5/91125)^2 + (0.01/0.59)^2 + (0.5/25)^2 + (0.027225/0.166375)^2)} = 0.169$

So absolute error in $E_f = 0.169 \times 3.23 \text{ GPa} = \pm 0.55 \text{ GPa}$

Overall, $E_f = (3.23 \pm 0.55) \text{ GPa}$

Appendix 5. FTIR Spectra

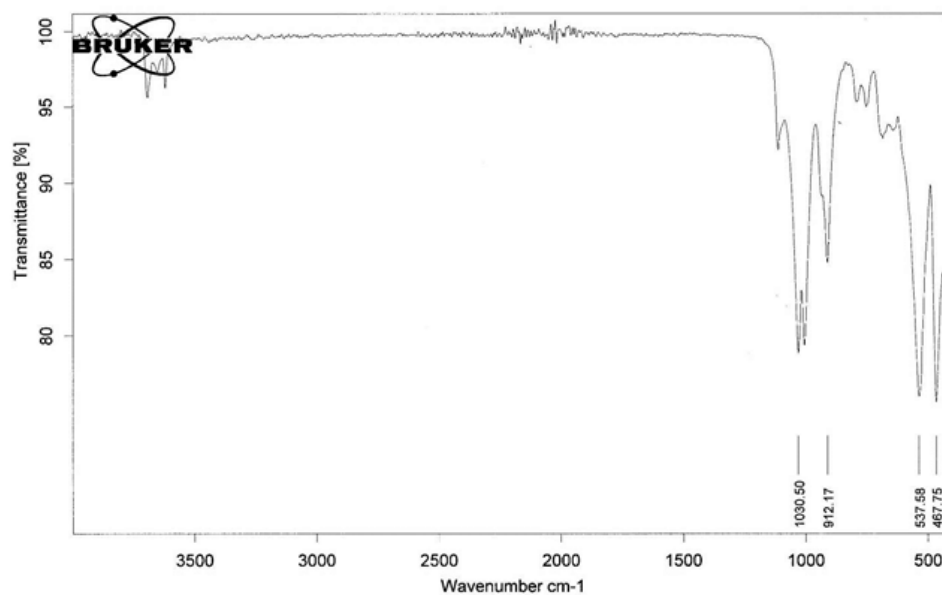


Figure A5-1. FTIR spectrum of Barrisurf LX kaolinite.

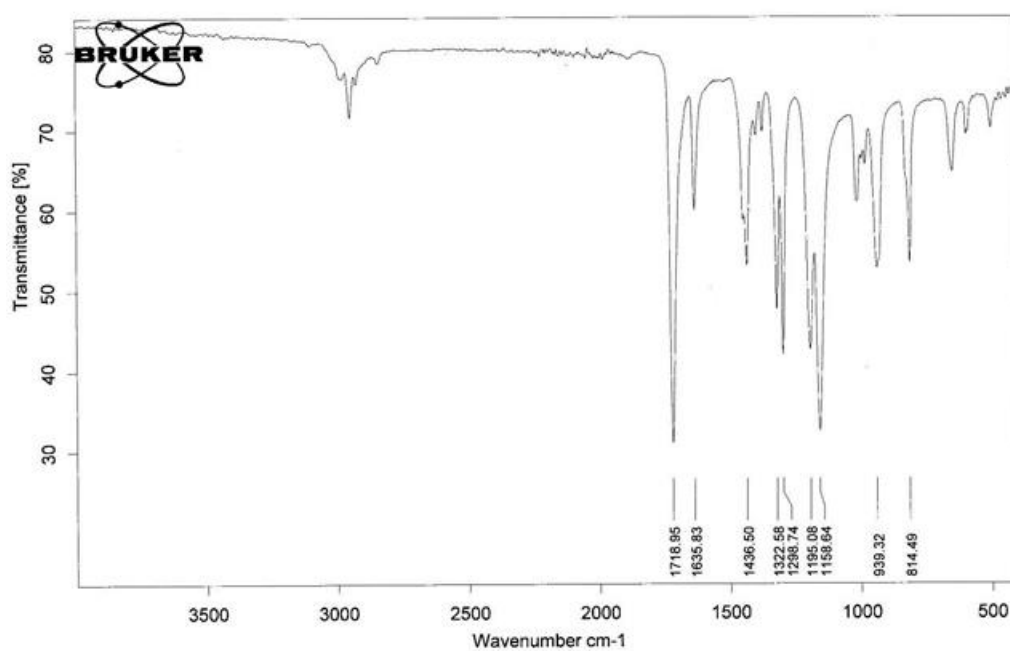


Figure A5-2. FTIR spectrum of methyl methacrylate.

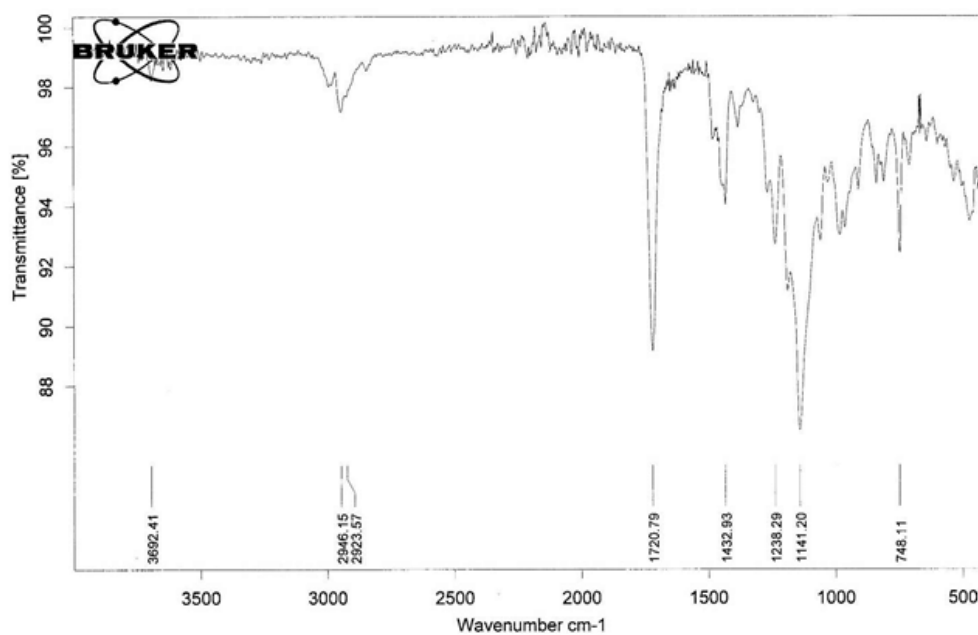


Figure A5-3. FTIR spectrum of poly (methyl methacrylate) by redox polymerisation.

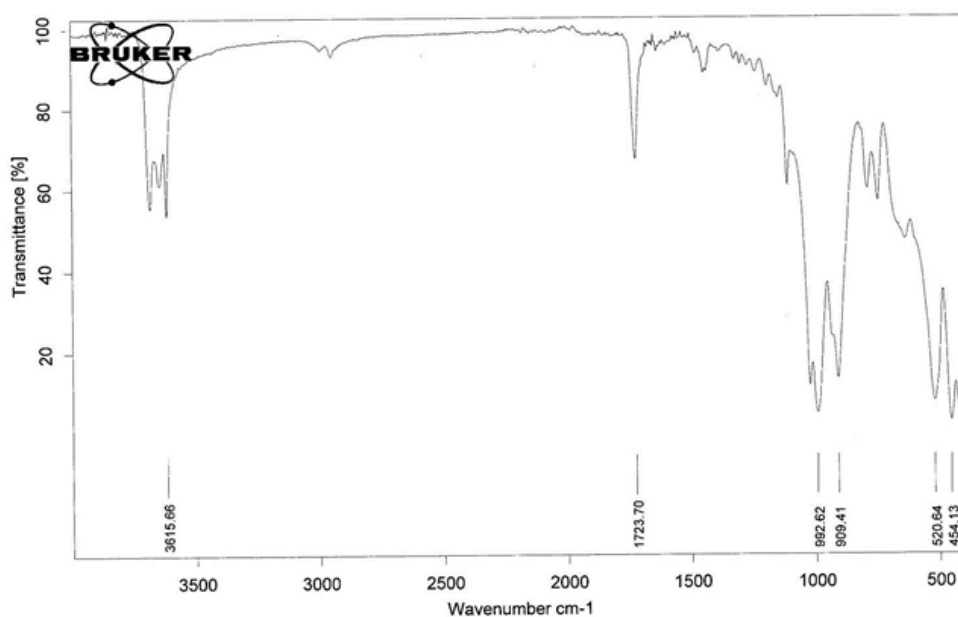


Figure A5-4. FTIR spectrum of a PMMA/kaolinite composite sample polymerised under N₂.

Appendix 6. Figures and results of three point loading test of PMMA and PMMA/kaolinite composite by redox polymerisation

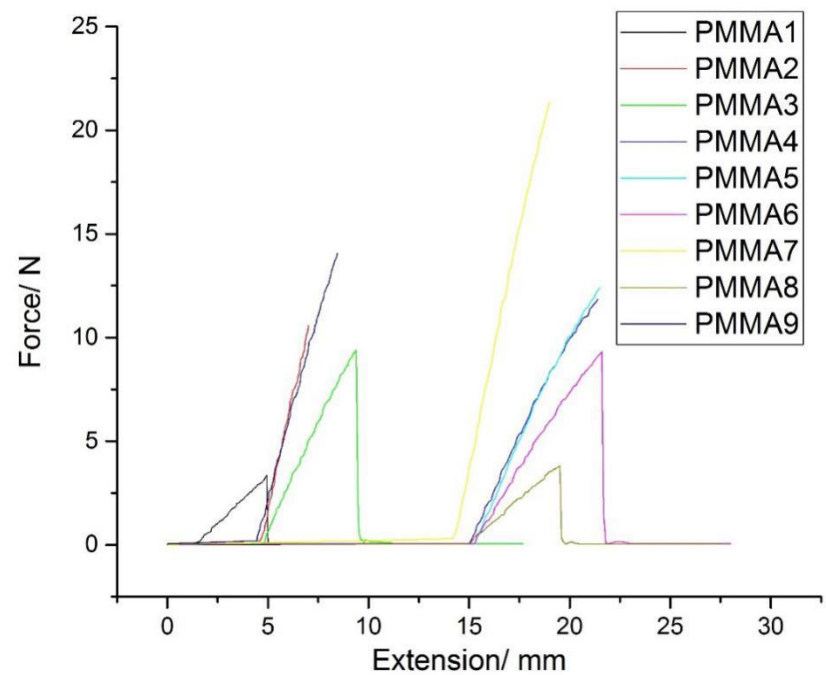


Figure A6-1. Three points loading test of PMMA by redox polymerisation.

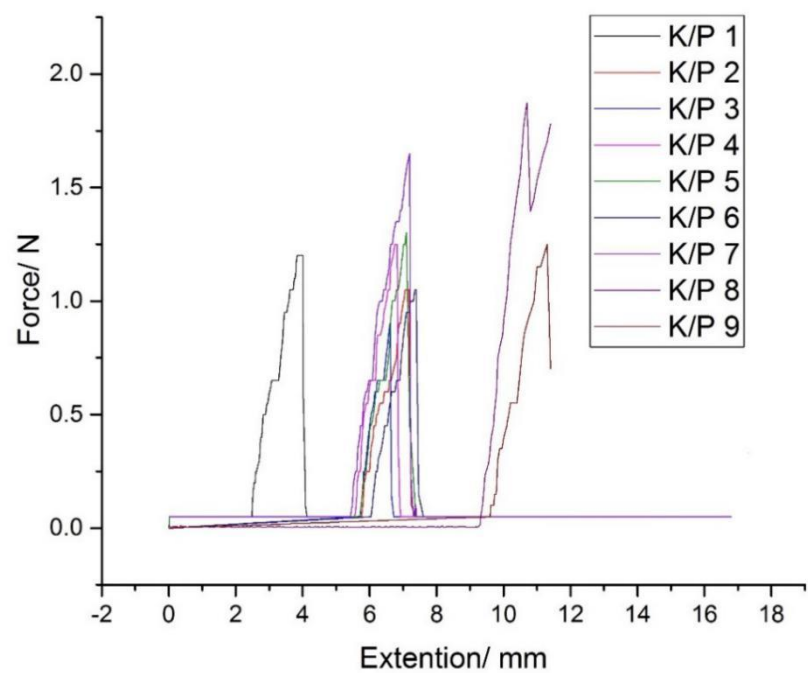


Figure A6-2. Three points loading test of kaolinite/PMMA composite.

Table A6-1. Flexural strength and modulus of PMMA.

PMMA Sample	σ_f / MPa	E_f / GPa
1	18 ± 2	1.9 ± 0.3
2	18 ± 3	1.5 ± 0.4
3	34 ± 5	2.2 ± 0.5
4	39 ± 6	1.8 ± 0.4
5	60 ± 10	3.1 ± 0.9
6	46 ± 7	2.6 ± 0.6
7	70 ± 30	4.4 ± 2.5
8	22 ± 2	1.9 ± 0.3
9	47 ± 8	3.4 ± 0.8
Mean	40	2.5
Standard Deviation	± 20	± 0.9
Standard Error of the Mean	± 10	± 0.3

Table A6-2. Flexural strength and modulus of kaolinite/PMMA composite.

PMMA-kaolinite Sample	σ_f / MPa	E_f / GPa
1	100 ± 40	80 ± 50
2	41 ± 4	24 ± 4
3	23 ± 2	17 ± 3
4	29 ± 5	16 ± 4
5	34 ± 3	17 ± 3
6	34 ± 3	19 ± 3
7	49 ± 7	16 ± 4
8	60 ± 10	30 ± 10
9	40 ± 5	20 ± 4
Mean	40	30
Standard Deviation	± 20	± 20
Standard Error of the Mean	± 7	± 7

References

- [1] Dikin DA, Stankovich S, Zimney EJ, Piner RD, Dommett GH, Evmenenko G, Nguyen ST, Ruoff RS. Preparation and characterization of graphene oxide paper. *Nature*. 2007 Jul 26;448(7152):457-60.
- [2] Moon IK, Lee J, Ruoff RS, Lee H. Reduced graphene oxide by chemical graphitization. *Nature communications*. 2010 Sep 21;1:73.